

ENDMEMBER AND PROPORTION ESTIMATION USING PHYSICS-BASED
MACROSCOPIC AND MICROSCOPIC MIXTURE MODELS

By

RYAN CLOSE

A DISSERTATION PRESENTED TO THE GRADUATE SCHOOL
OF THE UNIVERSITY OF FLORIDA IN PARTIAL FULFILLMENT
OF THE REQUIREMENTS FOR THE DEGREE OF
DOCTOR OF PHILOSOPHY

UNIVERSITY OF FLORIDA

2011

© 2011 Ryan Close

ACKNOWLEDGMENTS

I would like to thank my family, friends, and mentors for providing encouragement and support throughout my academic career. Specifically, I want to thank my parents, Don and Marian Close, my sister, Katherine Close, and my grandparents, Hal and Ann Ingman and Don and Peggy Close. A special thanks to my grandfathers, whose influence first led me to engineering and science.

I would like to thank my advisors, Dr. Paul Gader and Dr. Joe Wilson, for all of their guidance and support. I would also like to thank my committee members, Dr. Daniel Lee, Dr. Douglas Dankel, and Dr. Arunava Banerjee, for all of their help and valuable suggestions. Additionally, I would like to thank all of my current and former labmates for the many times in which they have assisted in my research and served as a sounding board for ideas.

Above all, I thank God, for providing me the opportunity to pursue this research and granting me the capability to proceed successfully.

TABLE OF CONTENTS

	<u>page</u>
ACKNOWLEDGMENTS	3
LIST OF TABLES	6
LIST OF FIGURES	7
LIST OF ABBREVIATIONS	11
ABSTRACT	13
CHAPTER	
1 INTRODUCTION	15
Hyperspectral Data	15
Mixture Based Models	17
Problem Statement	18
2 LITERATURE REVIEW	19
Macroscopic Mixtures	20
Introduction to Macroscopic Mixtures	20
Statistical Approaches to the LMM Inversion Problem	22
Iterated constrained endmembers algorithm	22
Sparsity promoting iterated constrained endmember	24
Geometric Approaches to the LMM Inversion Problem	24
Pixel purity index	25
N-FINDR	26
Vertex component analysis	26
Microscopic Mixtures	27
Introduction to Microscopic Mixing	27
Reflectance functions	28
Single-scattering albedo	31
Existing Endmember and Proportion Estimation Methods	32
Endmember estimation	32
Proportion estimation	33
Hyperspectral Nonlinear Mixture Models	39
Virtual Endmembers	39
Kernel Methods for Endmember and Proportion Estimation	40
Neural Network Based Proportion Estimation	41
Manifold Learning in Hyperspectral Data	42
ISOMAP	44
Sub-manifolds	44
Manifold-based endmember estimation	45

3	TECHNICAL APPROACH	48
	Review of Macroscopic and Microscopic Mixtures.....	48
	Macroscopic Mixtures.....	49
	Microscopic Mixtures.....	49
	Discrete Mixture Estimation	53
	Proportion Estimation	54
	Endmember Estimation	56
	Multi-Mixture Pixel Estimation.....	58
	Multi-Mixture Pixel Model	58
	Proportion Estimation	59
	Endmember Estimation	61
4	EXPERIMENTAL RESULTS.....	67
	Synthetic Data sets.....	68
	Description of Data sets	68
	Endmember Estimation	69
	Initialization and parameter robustness	71
	Microscopic mixture effects.....	73
	Endmember estimation accuracy.....	78
	Proportion Estimation	79
	Microscopic mixture effects.....	81
	Estimating microscopic mixture concentration	81
	Proportion estimation accuracy.....	83
	RELAB Data sets.....	84
	Description of Data Sets.....	84
	Endmember Estimation	85
	Proportion Estimation	85
	Aerial Hyperspectral Data Sets.....	87
	Baseball Diamond Scene	88
	Beach Scene	89
5	CONCLUSION.....	124
	LIST OF REFERENCES	128
	BIOGRAPHICAL SKETCH.....	140

LIST OF TABLES

<u>Table</u>		<u>page</u>
4-1	Algorithm μ parameter settings.....	91
4-2	RELAB data set true proportions.....	91
4-3	Comparison of proportion estimates of RELAB mixtures using mass fraction and F-parameter values. A) Olivine & Enstatite mixture. B) Olivine & Magnetite mixture.....	92

LIST OF FIGURES

<u>Figure</u>	<u>page</u>
2-1 Two linear simplexes formed from macroscopic mixtures of five endmembers with uniform proportions	47
2-2 Two nonlinear simplexes formed from microscopic mixtures of five endmembers with uniform proportions	47
3-1 Derivative of reflectance function over range of albedo values	63
3-2 Macroscopic mixture points formed from uniform proportions of two endmembers.....	63
3-3 Reflectance curve with microscopic mixture points formed from uniform proportions of two endmembers	64
3-4 Three dimensional plot of microscopic mixture of two endmembers	64
3-5 Diagram of multi-mixture pixel	65
3-6 Diagram of multi-mixture pixel	65
3-7 Diagram of multi-mixture pixel	66
4-1 Synthetic endmember reflectance spectra	93
4-2 1 st and 2 nd principal components of synthetic CMM data set.....	93
4-3 1 st and 3 rd principal components of synthetic CMM data set	94
4-4 1 st and 2 nd principal component of synthetic MMP data set.....	94
4-5 1 st and 3 rd principal component of synthetic MMP data set	95
4-6 Mean MABE over range of annealing rates.....	95
4-7 Mean MABE of synthetic CMM data sets over range of μ settings	96
4-8 Histogram of ICE MABE using random starting points	96
4-9 Histogram of RLMM-GD MABE using random starts.....	97
4-10 Histogram of AD-RLMM-GD MABE using random starts	97
4-11 Histogram of DME MABE using random starts.....	98
4-12 Histogram of MPE MABE using random starts	98

4-13	RLMM-GD estimated endmembers for CMM data set (1 st and 2 nd principal components).....	99
4-14	RLMM-GD estimated endmembers for CMM data set (1 st and 3 rd principal components).....	99
4-15	RLMM-GD estimated endmembers for CMM data set (spectra).....	100
4-16	RLMM-GD estimated endmembers for CMM data set.....	100
4-17	RLMM-GD estimated endmembers for CMM data set.....	101
4-18	RLMM-GD estimated endmembers for CMM data set.....	101
4-19	RLMM-GD estimated endmember spectra with multiple μ parameters	102
4-20	Mean MABE of VCA, DME, and MPE	102
4-21	Mean MABE of ICE, RLMM-GD, DME, and MPE.....	103
4-22	Mean MABE of AD-RLMM-GD, DME, and MPE.....	103
4-23	Histogram of VCA MABE values for CMM data set	104
4-24	Histogram of ICE MABE values for CMM data set	104
4-25	Histogram of RLMM-GD MABE values for CMM data set	105
4-26	Histogram of AD-RLMM-GD MABE values for CMM data set	105
4-27	Histogram of DME MABE values for CMM data set	106
4-28	Histogram of MPE MABE values for CMM data set.....	106
4-29	Mean MABE difference between VCA and DME and MPE	107
4-30	Mean MABE difference between ICE and DME and MPE.....	107
4-31	Mean MABE difference between RLMM-GD and DME and MPE.....	108
4-32	Mean MABE difference between AD-RLMM-GD and DME and MPE	108
4-33	Histogram of MABE difference between VCA and DME and MPE for CMM data set.....	109
4-34	Histogram of MABE difference between ICE and DME and MPE for CMM data set.....	109

4-35	Histogram of MABE difference between RLMM-GD and DME and MPE for CMM data set	110
4-36	Histogram of MABE difference between AD-RLMM-GD and DME and MPE for CMM data set.....	110
4-37	Histogram of MABE difference between VCA, ICE, RLMM-GD, AD-RLMM-GD, and DME and MPE for MMP-HMP data set	111
4-38	Comparison of nonlinearity in albedo-domain and reflectance-domain mixtures	111
4-39	Microscopic proportions resulting from LMM, AD-LMM, DME, and MPE over all synthetic data sets	112
4-40	Proportion RMSE resulting from LMM, AD-LMM, DME, and MPE over all synthetic data sets.....	112
4-41	Spectra of Enstatite and Olivine mixture.....	113
4-42	Spectra of Magnetite and Olivine mixture	113
4-43	Wavelength scatter plot of Magnetite and Olivine mixture	114
4-44	Endmember estimation of RELAB Magnetite and Olivine mixture.....	114
4-45	Endmember estimation of RELAB Enstatite and Olivine mixture.....	115
4-46	RELAB data sets endmember estimation error chart	115
4-47	Baseball diamond scene	116
4-48	Endmembers estimated from baseball diamond scene.....	116
4-49	Points labeled by DME as microscopically mixed.....	117
4-50	MPE microscopic mixture proportions	117
4-51	MPE grass macroscopic proportions	118
4-52	MPE grass microscopic proportions	118
4-53	MPE dirt macroscopic proportions.....	119
4-54	MPE dirt microscopic proportions	119
4-55	MPE clay macroscopic proportions	120
4-56	MPE clay microscopic proportions.....	120

4-57	Beach scene.....	121
4-58	Microscopic proportions estimated using MPE	121
4-59	Macroscopic proportion map for sand endmember	122
4-60	Microscopic proportion map for sand endmember.....	122
4-61	Macroscopic proportion map for sediment endmember.....	123
4-62	Microscopic proportion map for sediment endmember	123

LIST OF ABBREVIATIONS

AD-LMM	Albedo-domain linear mixture model
AD-MMM	Albedo-domain microscopic mixture model
AD-RLMM-GD	Albedo-domain regularized linear mixture model gradient descent
BRDF	Bidirectional reflectance distribution function
CMM	Combined macroscopic and microscopic
DME	Discrete mixture estimation
HNN	Hopfield neural network
HNN/MLP	Hopfield neural network / multi-layer perceptron
HSI	Hyperspectral image
ICE	Iterated constrained endmembers
IR	Infrared
KFCLS	Kernel fully-constrained least squares
LIDAR	Light detection and ranging
LMM	Linear mixture model
LSE	Least squared error
MABE	Mean absolute band error
MLP	Multi-layer perceptron
MMP	Multi-mixture pixel
MMP-HMP	Multi-mixture pixel with high microscopic proportion
MNF	Minimum noise fraction
MPE	Multi-mixture pixel estimation
MSE	Mean squared error
PCA	Principal component analysis
PPI	Pixel purity index

SPICE	Sparsity promoting iterated constrained endmembers
SPT	Sparsity-promoting term
SSA	Single-scattering albedos
SSD	Sum of squared distances
SVDD	Support vector data description
RBF	Radial basis function
RBF-L	Radial basis function linear
RBF-NL	Radial basis function nonlinear
RBFNN	Radial basis function neural network
RD-MMM	Reflectance-domain microscopic mixture model
RELAB	Reflectance experiment laboratory
RLMM-GD	Regularized linear mixture model gradient descent
RMSE	Root mean square error
RSS	Residual sum of squares
VCA	Vertex component analysis

Abstract of Dissertation Presented to the Graduate School
of the University of Florida in Partial Fulfillment of the
Requirements for the Degree of Doctor of Philosophy

ENDMEMBER AND PROPORTION ESTIMATION USING PHYSICS-BASED
MACROSCOPIC AND MICROSCOPIC MIXTURE MODELS

By

Ryan Close

December 2011

Chair: Paul Gader
Cochair: Joseph Wilson
Major: Computer Engineering

Methods of incorporating macroscopic and microscopic mixture models into hyperspectral image (HSI) endmember and proportion estimation is presented and discussed. These methods utilize the linear mixture model (LMM) and the bidirectional reflectance distribution function to model macroscopic and microscopic mixtures, respectively. This allows for estimation of endmembers and their proportions from HSIs composed of both macroscopic and microscopic mixtures.

A vast majority of HSI endmember and proportion estimation methods rely on the LMM to describe pixel spectra resulting from mixtures of endmembers. However, nonlinear mixtures have been shown to exist in HSIs. Specifically, the microscopic mixture is known to cause nonlinear mixing relationships between endmembers. Methods using microscopic mixture models exist but rely on severely limiting assumptions or estimations of the nonlinearity present in microscopic mixtures. The methods presented in this research explicitly account for the nonlinearity caused by microscopic mixing. The mixtures are, therefore, estimated directly from the data

without the need for *a priori* knowledge of the mixture types. In addition, the explicit modeling of both mixture types allows for direct estimation of endmembers.

Results are presented using synthetic data sets, which consist of macroscopic and microscopic mixtures, to demonstrate the increased accuracy in endmember and proportion estimation using these new physics-based methods over existing linear methods. In addition, results are presented using a well-known laboratory data set. Using these results and other published results from this data set, increased accuracy in proportion estimation over other microscopic mixture methods is shown. Finally, a qualitative analysis of the new methods is performed using an HSI collected from an airborne platform.

CHAPTER 1 INTRODUCTION

Hyperspectral Data

Hyperspectral image (HSI) data is characterized by a set of spatially organized pixels. [1, 2] Each pixel has an associated reflectance spectrum, estimated from radiance measurements collected by the sensor. [1] Each pixel spectrum contains 10's – 100's of contiguous wavelengths, also called bands, often with a spatial resolution of 1-30 square meters. [1, 2] Often the goal of HSI analysis is to identify the substances and their abundances from a given scene. [1] This task is complicated by the mixtures and interactions present in hyperspectral data. This fact necessitates the ill-posed inversion problem of estimating substance spectra and abundances of each substance present in a scene. [1]

Hyperspectral sensors are commonly used from air and space borne platforms. [1, 2] This causes limited spatial and spectral resolutions. As a result it is not possible to fully resolve the spectral signature of every substance or compound imaged by the sensor. [1] Therefore, the endmember concept is introduced. An endmember is defined (for the purposes of this research) as a substance within an HSI that can be described by a single observable spectral signature. Examples of the endmember concept would be a single substance or compound, such as clay, or a static mixture, such as a uniform mixture of sand and silt (i.e., no variations in mixture proportions between the mixed endmembers are present in the scene). The ill-posed inversion problem, illustrated in Equation 1-1, is restated as the estimation of an HSI's endmembers (E) and their proportions (p_i) present in each pixel (x_i) subject to a set of

underlying functions ($func$). [1] This problem is often known as endmember extraction and pixel unmixing.

$$\mathbf{x}_i = func(E, \mathbf{p}_i) + \epsilon_i \quad (1-1)$$

A vast majority of research to date has attempted to solve this inversion problem by modeling the function as a linear mixture of endmembers (\mathbf{e}_k), shown in Equation 1-2 and Equation 1-3. [1, 3-6] This type of mixture is known as a macroscopic mixture. [7] While the linear approach is amenable to mathematical analysis, it has been repeatedly shown that nonlinear mixing is prevalent in hyperspectral data. [1, 8-22] Specifically, multi-scattering between endmember particles, or microscopic mixing, is known to be pervasive in many scenes and to form nonlinear mixtures. [1, 7, 20-34]

$$\mathbf{x}_i = \sum_{k=1}^M \mathbf{e}_k p_{ik} + \epsilon_i \quad (1-2)$$

$$\forall_{ik} p_{ik} \geq 0 \quad \forall_i \sum_{k=1}^M p_{ik} = 1 \quad (1-3)$$

Attempts to incorporate the nonlinearity of microscopic mixing into the unmixing problem have largely been black-box approaches. Traditional methods of reproducing an unknown nonlinear function such as neural networks [35-38] and kernel methods [23-25, 28, 39-41] have been used to learn the function in Equation 1-1. Recent research has introduced manifolds to model the nonlinearity in hyperspectral data. Typically used in hyperspectral classification applications, endmember and proportion estimation has also been pursued with manifold based models. [42-44] These methods all attempt to account for the nonlinearity with a generic machine learning model to

approximate the mixture, however they do not explicitly model the underlying physics of the mixture.

Mixture Based Models

Often, many plausible endmembers and proportions exist that can explain the data. [3, 4] This is a common problem when addressing ill-posed inversion problems. This fact necessitates the inclusion of constraints into the unmixing problem to ensure a physically realizable and probable solution. Basing the unmixing model on physics-based models derived from the theories of reflectance spectroscopy achieve this goal. [1, 23-25, 32] Using reflectance spectroscopy to analyze an HSI is known as image spectroscopy. Algorithms based on these models constrain the inversion to be governed by the physical properties of the environment in which the data were collected, thereby finding solutions relevant to a real-world explanation of the data. [1]

The linear mixture model (LMM) mentioned above effectively models macroscopic mixtures in hyperspectral data. [1] Macroscopic mixtures, also referred to as areal or checkerboard mixtures, are formed when the spectral signatures of two or more endmembers are measured and represented by a single pixel. [1] This causes an averaging of spectral signatures as described by the LMM. This type of mixing is caused by the coarse resolution of the sensor and is not a physical mixing of endmembers.

In contrast, microscopic mixtures, also known as intimate mixtures, do represent a physical mixing of endmember's particles. Microscopic mixtures are formed when particles of two or more endmembers are homogeneously mixed together causing multi-scattering between the particles of the endmembers. [7, 30-32] Multi-scattering between particles causes a linear mixing of the constituent endmember's single-

scattering albedos (SSA). [7, 30] The reflectance spectrum resulting from the average SSA is manifested as a nonlinear mixing of the endmembers. Utilizing various remote sensing assumptions the reflectance spectra can be estimated using Hapke's bidirectional reflectance distribution function. [7, 30, 32]

In the past two decades of HSI analysis research, the macroscopic mixture has largely been regarded as the dominant mixture present. [1-4, 45-58] This is a direct consequence of the coarse pixel resolution of commonly used hyperspectral sensors. As sensor resolution continues to improve, the macroscopic mixture is becoming less prominent and the effects of physically occurring mixtures, such as the microscopic mixture, are becoming dominant. [8-13, 15-18, 23-25, 27, 28, 42-44, 59-70] This necessitates the ability to estimate endmembers and proportions while fully accounting for the physical mixtures, specifically microscopic mixtures.

Problem Statement

Currently, models and associated algorithms for estimating endmembers in the presence of both macroscopic and microscopic mixtures do not exist. Additionally, existing methods for estimating proportions in the presence of both macroscopic and microscopic mixtures rely on approximate models that do not explicitly represent the mixtures present in hyperspectral data. Using the reflectance models describing macroscopic and microscopic mixing, this research will investigate computational models to estimate endmembers and proportions in the presence of both mixtures.

CHAPTER 2 LITERATURE REVIEW

Hyperspectral image analysis can take many forms depending on the desired application, such as anomaly and target detection[2] or monitoring variations in vegetation cover[15]. Similarly, the breadth of research in HSI analysis is extensive, including feature extraction[1], detecting the number of endmembers[71, 72], band selection[5], dimensionality analysis[73], spectral libraries for unmixing[74], anomaly and target detection[2], etc. However, a common goal of HSI applications is to characterize some aspect of a scene via air or space borne collections. [1, 2, 75]

An HSI collection can be generalized into two procedures. First, a given area is scanned by the hyperspectral sensor and its radiance, or raw energy, is measured. [1] Secondly, a post-processing step is used to convert the radiance values to reflectance; this process takes into account collection specific atmospheric and illumination parameters. [1, 2] Some applications use measured radiance as an input data source, however converted reflectance data is assumed when utilizing reflectance spectroscopy models. [1]

To fully characterize an HSI, the endmembers, proportions, and mixtures present in a scene must be determined. [1] An endmember is defined, for the purposes of this research, as a substance within an HSI that can be described by a single observable spectral signature. Examples of the endmember concept are single substances or compounds, such as clay, or a static mixture, such as a uniform mixture of sand and silt (i.e., no variations in mixture proportions between the endmembers are present in the

HSI). The concepts of proportions and mixtures will be conveyed through the discussion of the mixture models.

Assuming no prior knowledge of the area scanned, this problem is an ill-posed inversion problem. [1, 3] As a result, there exist infinitely many plausible solutions to the problem. The principles and theories of reflectance spectroscopy are used to create models constrained by the laws of physics. [1, 7] These models result in physically plausible endmember, proportion, and mixture estimations. [7] This approach to analyzing HSIs can be referred to as image spectroscopy.

Macroscopic Mixtures

Introduction to Macroscopic Mixtures

A common mixture type in HSIs is the macroscopic mixture, also known as an areal or checkerboard mixture. [1] This type of mixture is caused by the presence of two or more discrete endmembers within a single pixel's instantaneous field of view. [1] In a macroscopic mixture the endmembers are not physically mixed; however, the spectral signatures of each endmember are mixed within the pixel's spectra. [1, 2] Mixing of this type is caused by the finite spatial resolution of optical detectors. Thus, a hyperspectral sensor's spatial resolution is directly related to the amount of macroscopic mixing present in an HSI. [1]

Macroscopically mixed reflectance spectra (\mathbf{r}) are modeled by a linear combination of spectra from each of the M constituent endmembers (\mathbf{r}_k), as shown in Equation 2-1. [1, 2, 7, 20, 22] The geometric cross-section (F_k) of the k^{th} endmember is the physical realization of the proportion of a mixed spectra composed of the endmember's spectra.

$$\mathbf{r} = \sum_{k=1}^M F_k \mathbf{r}_k \quad (2-1)$$

The macroscopic mixture model, known as the LMM, serves as the foundation for many approaches to HSI endmember and proportion estimation. [1, 2, 76-78] The LMM (Equation 2-2) represents the i^{th} pixel of an HSI (\mathbf{x}_i) as the linear combination of M endmembers (\mathbf{e}_k) and their respective proportions (p_{ik}) with additive zero-mean Gaussian noise (ϵ_i). [3, 4] The LMM has the constraints $\forall_{ik} p_{ik} \geq 0$ and $\forall_i \sum_{k=1}^M p_{ik} = 1$. This linear relationship makes the model amenable to mathematical analysis, which largely contributes to its popularity.

$$\mathbf{x}_i = \sum_{k=1}^M p_{ik} \mathbf{e}_k + \epsilon_i \quad (2-2)$$

The formulation of the LMM (Equation 2-2), with its associated constraints, depicts an HSI pixel as a convex combination of its endmembers. The LMM, therefore, implies a convex hull assumption over the set of pixels composing an HSI. [1, 2, 76-78] Consequentially, the LMM forms an $M-1$ linear simplex within a D -dimensional space, where D is the number of wavelengths (or bands) measured by the hyperspectral sensor. [52] The HSI endmembers are the vertices of this simplex. An example of two such simplexes, created by the LMM, can be seen Figure 2-1.

Numerous HSI endmember and proportion estimation algorithms, based on the LMM, have been published. [1-4, 6, 45-47, 49-58, 76-82] This includes recent algorithms that incorporate spatial information into the LMM. [82-91] The algorithms formed from the LMM can be generalized into two categories of autonomous approaches: statistical and geometric. [55, 77, 78]

Statistical Approaches to the LMM Inversion Problem

Statistical based approaches minimize or maximize a given objective function. [3, 4, 45-47, 49, 50] The objective function to minimize is often the squared error between the spectral signature of each pixel in the HSI and the reconstructed spectra. [3] The reconstructed spectra are formed from the mixture of the estimated endmembers and their respective proportions. The statistical methods often incorporate simultaneous estimation of endmembers and proportions. A popular method using this approach is the Iterated Constrained Endmembers (ICE) algorithm. [3] The ICE algorithm has also spawned many variants that address shortfalls in the model. For example, the Sparsity Promoting Iterated Constrained Endmember (SPICE) algorithm, uses a Bayesian approach to automatically determine the number of endmembers while simultaneously estimating the endmembers and proportions. [4] Both the ICE and SPICE algorithms are described in the following sections.

Iterated constrained endmembers algorithm

The ICE algorithm minimizes a residual sum of squares (RSS) term, shown in Equation 2-3. This is accomplished by estimating a set of endmembers (\mathbf{e}_k) and the proportions (p_{ik}) that best explain the spectral data for each pixel. [3]

$$RSS = \sum_{i=1}^N \left(\mathbf{x}_i - \sum_{k=1}^M p_{ik} \mathbf{e}_k \right)^T \left(\mathbf{x}_i - \sum_{k=1}^M p_{ik} \mathbf{e}_k \right) \quad (2-3)$$

The model, in an attempt to minimize the RSS, can theoretically create an infinitely large convex hull that completely contains the given data points. While these endmembers create a zero error solution, they are not unique and have no guarantee of being probable or even plausible. The model therefore requires additional

considerations in the objective to constrain the set of possible solutions. The sum of squared distances (SSD) term is used for this constraint, shown in Equation 2-4.

$$SSD = \sum_{k=1}^{M-1} \sum_{l=k+1}^M (\mathbf{e}_k - \mathbf{e}_l)^T (\mathbf{e}_k - \mathbf{e}_l) \quad (2-4)$$

The SSD term is proportional to the volume of the area bounded by the endmembers and thus, when minimized, provides endmembers that are tightly fitted around the data. It can be shown that the SSD formulation (Equation 2-4) is equivalent to the formulation shown in Equation 2-5, where V is the sum of variances.

$$SSD = M(M - 1)V \quad (2-5)$$

Using this new formulation for SSD (ignoring the $M(M - 1)$ constant) and the RSS, a new objective function is formed. This new objective is referred to as the regularized RSS and is shown in Equation 2-6, with μ being a regularization parameter.

$$RSS_{reg} = (1 - \mu) \frac{RSS}{N} + \mu V \quad (2-6)$$

Using this new regularized formulation, ICE estimates endmembers by minimizing the RSS_{reg} objective function, with respect to the \mathbf{e}_k 's, while holding the proportions fixed. Minimization of this objective function is accomplished using a closed form solution. Next, the proportion values are estimated with quadratic programming, while holding the endmembers fixed. This alternating optimization algorithm is continued until a convergence criterion is met.

Given a set of data points, this model may estimate a singular set of endmembers that represents a plausible, and even probable, explanation of the data. However, no guarantee exists that these are actual endmembers. This model also suffers from the

assumption that only linear relationships are present in the given HSI data, i.e., only macroscopic mixtures exist.

Sparsity promoting iterated constrained endmember

The SPICE algorithm is a popular variant of the ICE approach to HSI endmember and proportion estimation. [4] SPICE uses a Bayesian approach to autonomously determine the number of endmembers. In contrast, other techniques require the number of endmembers as input parameters to the algorithm. This capability is introduced through the sparsity-promoting term (SPT) shown in Equation 2-7 and Equation 2-8. The Γ parameter is an input associated with the degree to which the proportions are driven to zero.

$$SPT = \sum_{k=1}^M \gamma_k \sum_{i=1}^N |p_{ik}| = \sum_{k=1}^M \gamma_k \sum_{i=1}^N p_{ik} \quad (2-7)$$

$$\gamma_k = \frac{\Gamma}{\sum_{i=1}^N p_{ik}} \quad (2-8)$$

The SPICE objective function, given by Equation 2-9, is updated in a manner similar to the ICE algorithm. As with ICE, the SPICE algorithm will output the endmembers and proportions estimated from the HSI data.

$$RSS_{reg}^{SPICE} = (1 - \mu) \frac{RSS}{N} + \mu V + SPT \quad (2-9)$$

Geometric Approaches to the LMM Inversion Problem

Geometric approaches exploit the convex hull geometry formed by the endmembers and their linear mixtures. [51-58] The endmembers, which appear as vertices, form the linear simplex described by this geometry. This simplex reveals an implicit assumption of the geometric algorithms, the pure-pixel assumption. The pure-pixel assumption requires that a given HSI have at least one pure pixel of each

endmember present in the scene (i.e., $\forall_k \exists! p_{ik} = 1$). This fact illustrates the prominent disadvantage of the geometric algorithms over the statistical approaches.

A notable advantage of a geometric approach is an increased robustness to small data sets. Unlike statistical methods, geometric approaches do not require the optimization of an objective function through learning spectra and proportions. The geometric category of algorithms exploits the intrinsic geometry created by the LMM, or similar properties of the simplex, to find endmember spectra existing in the given data. Once the pure-pixel assumption is satisfied, geometric approaches are able to find endmembers within a smaller data set than would be required by a statistical approach. Using these endmembers the proportions can then be estimated.

As with the statistically based models, many variations appear in literature. Three popular algorithms are described: the pixel purity index (PPI)[53], N-FINDR[57], and vertex component analysis (VCA)[54].

Pixel purity index

The PPI algorithm attempts to find the pixels in a hyperspectral scene that have the purest representation of an endmember. [53] The algorithm first uses minimum noise fraction (MNF) to reduce the dimensionality of the data and perform noise whitening. Next, the data is projected onto numerous randomly created vectors. With every vector the pixels creating extremal values are recorded. After this process has run a predetermined number of times the results are analyzed. The pixels shown to have had frequent extremal values are determined to represent the purest pixels. This extremity-score is related to the pixel's purity through convex geometry analysis. [52] The PPI algorithm was originally designed for target detection, however the PPI has

been used, often with the addition of other algorithms or manual input, to extract endmembers and model the background subspace of hyperspectral scenes.

N-FINDR

The N-FINDR algorithm is based on the assumption that the largest volume simplex, in the spectral feature-space, is formed by the endmembers of the scene. [57] The algorithm starts by initially selecting a group of pixels from the HSI, these are the initial endmembers. The volume of the simplex defined by the pixel's spectra is calculated. A new pixel is then selected to replace one of the current endmembers. The volume of the simplex created with the replaced endmember is calculated. If the new volume is larger than the previous volume the replacement stays, otherwise the previous endmember set is restored. This process is repeated for all of pixels in the scene. The set of endmembers (pixels) remaining at the end of the algorithm creates a simplex enclosing the largest possible volume. Thus they are the endmembers for the given HSI scene.

Vertex component analysis

As with PPI and N-FINDR, VCA exploits the simplex geometry of a hyperspectral mixture and attempts to find the vertices of the simplex. Thus again requiring the pure-pixel assumption. [54] After initialization, the VCA algorithm projects data onto a direction orthogonal to the simplex spanned by the existing set of endmembers. The pixels corresponding to the extremal values in the projections are labeled endmembers. This process continues until a predetermined number of endmembers in the scene is found.

Microscopic Mixtures

Resulting from the prevalence of macroscopic mixing in hyperspectral scenes and the mathematical amenability of the LMM, a majority of endmember and proportion estimation research has been focused on macroscopic mixtures. [1] However, research has shown that nonlinear mixtures are present in hyperspectral scenes and have a substantial effect on measured spectral reflectance signatures over a given scene. [1, 16, 17] Keshava and Mustard describe the effects of nonlinear mixing by stating[1]:

In tests of linear versus nonlinear mixing on laboratory data, the fractions calculated may be in error by as much as 30% absolute. In addition, the linear model can cause considerable ambiguity and false fractions when used on nonlinear mixtures. Absorption bands and continua in nonlinear mixtures cannot be adequately fit with a linear model.

Microscopic mixtures, also called intimate mixtures, are known to be present in many HSI scenes. [1, 7, 20-24, 30-34] Unlike the macroscopic mixture, microscopic mixtures form non-linear mixtures of endmember spectra. [7, 21, 22, 30, 31, 34] Consequently, the LMM has been shown inadequate for modeling this type of mixing in hyperspectral data. [1, 7, 20-24, 30-34] While microscopic mixing does represent physical mixtures of endmembers, it is important to note that it is not a chemical reaction (i.e., the constituent endmember substances still exist).

Introduction to Microscopic Mixing

Microscopic mixing occurs when particles of different endmembers are homogeneously distributed within a sensor's instantaneous field of view. Light incident on this mixed surface (assumed a semi-infinite medium) is scattered. The scattered radiance (power per unit area per unit solid angle of the detector) measured by a sensor (I), is the sum of the singly scattered radiance (I_S) and the multiply scatter radiance (I_M) (Equation 2-10). [7, 30] The close proximity of endmembers particles, occurring in a

microscopic mixture, causes multi-scatter between particles with different scattering properties. [1, 22] This multi-scattering between particles causes a nonlinear mixture in reflectance spectra. To accurately estimate endmembers and proportions within the context of microscopic mixture reflectance spectra, a robust model for reflectance is required. However, many types of reflectance exist.

$$I = I_S + I_M \quad (2-10)$$

Reflectance functions

The type of reflectance is characterized by the collimation of the light source and the detector (or sensor). The naming convention used to distinguish the various reflectance types, is by preceding two adjectives. These adjectives (listed in decreasing order of collimation) are typically: directional, conical, or hemispherical. The first adjective describes the degree of culmination of the source, and the second the detector. If both adjectives are the same a bi- is used in place of the first adjective. Because perfect collimation and perfect diffuseness do not exist, in reality all reflectances are biconical. [7, 30] However, on a clear, sunny day, the sun can be reasonably approximated as a collimated source (i.e., directional) and on an overcast day the light scattered by the clouds can be viewed as a diffuse source (i.e., hemispherical). [7] The human eye looking at the ground can be perceived as a directional detector; likewise an air or space borne sensor looking at the ground approximates a directional detector. [7] Therefore, under these basic remote sensing assumptions (including assuming minimal cloud cover), the bidirectional reflectance distribution function (BRDF) is the appropriate model for HSI applications.

Hapke's BRDF has been validated through experimentation and is widely accepted as an accurate model. [7, 20-35, 37] Hapke's BRDF is given by Equation

2-11, where μ_0 and μ are the cosine of the angles of incidence and emergence, respectively, g is the phase angle, $P(g)$ is the phase function for particles, $B(g)$ is the backscatter function given by Equation 2-12, $H(\mu)$ is Hapke's approximation to Chandrasekhar's function for isotropic multi-scattering given by Equation 2-13, and w is the average SSA given by Equation 2-14 with P_S and P_A being the power of the incident irradiance scattered and absorbed by the particle, respectively. [7, 30, 31] The phase angle and the angles of incidence and emergence describe the geometries of the light source and detector. Scattering properties of the surface are described by the $P(g)$ function. The backscatter function $B(g)$ models the opposition effect, as given by Equation 2-12 where B_0 describes the magnitude of the opposition effect and h depends on the interparticle spacing.

$$R(\mu_0, \mu, g) = \frac{w\mu_0}{4\pi(\mu_0 + \mu)} \{ [1 + B(g)]P(g) + H(\mu_0)H(\mu) - 1 \} \quad (2-11)$$

$$B(g) = \frac{B_0}{1 + \left(\frac{1}{h}\right)\tan(g/2)} \quad (2-12)$$

$$H(\mu) = \frac{1 + 2\mu}{\left(1 + 2\mu(1 - w_\lambda)^{1/2}\right)} \quad (2-13)$$

$$w = \frac{P_S}{P_S + P_A} \quad (2-14)$$

The BRDF shown in Equation 2-11 is given as published in Hapke's reflectance spectroscopy paper. [30] To unclutter the notation, the input parameters to the reflectance function will be dropped. Additionally, to avoid conflict with future uses of μ , c_i and c_e will be used in place of μ_0 and μ to represent the cosine of the angles of incidence and emergence. The BRDF with altered notations is shown in Equation 2-15.

$$R = \frac{wc_i}{4\pi(c_i + c_e)} \{ [1 + B(g)]P(g) + H(c_i)H(c_e) - 1 \} \quad (2-15)$$

A perfectly Lambertian surface reflects all light incident on it and appears equally bright when viewed from any given angle. [7, 30] Therefore, the BRDF of a Lambert reflectance is given by Equation 2-16. Using the BRDF (Equation 2-15) and the Lambert reflectance (Equation 2-16) the reflectance coefficient can be formulated as shown in Equation 2-17. [7, 30] The reflectance coefficient is the brightness relative to an identically illuminated Lambert surface. This normalized form of the BRDF is convenient for remote sensing applications and often used in literature for HSI analysis. [22-25, 32, 35]

$$R_L = \frac{c_i}{\pi} \quad (2-16)$$

$$R = \frac{w}{4(c_i + c_e)} \{ [1 + B(g)]P(g) + H(c_i)H(c_e) - 1 \} \quad (2-17)$$

Under remote sensing assumptions, the angle of incidence is commonly 15^0 to 40^0 and the angle of emergence 0^0 , under these conditions the phase angle is between 15^0 and 40^0 . [32] Additionally, under remote sensing assumptions, these angles are assumed constant over a given collection. Mustard and Pieters demonstrated that at phase angles greater than 15^0 the $B(g)$ was negligible. [32] Additionally, under the assumption of isotropic scattering (all light is scattered equally in all directions) the phase function is defined to be $P(g) = 1$. [7, 30] Using these remote sensing assumptions and the consequential results for $B(g)$ and $P(g)$, a simplified reflectance coefficient function can be derived as shown in Equation 2-18 where the λ subscript is used to signify the wavelength dependence of the reflectance function. Also, w_λ was added as a parameter to Chandrasekhar's function to represent the single-scattering

albedo as an input parameter to the function. As the reflectance coefficient function, under the described assumptions, is the only model for reflectance (Equation 2-18) used in this research it will simply be referred to as the reflectance function.

$$R_{\lambda} = \frac{w_{\lambda}}{4(c_i + c_e)} H(c_i, w_{\lambda}) H(c_e, w_{\lambda}) \quad (2-18)$$

Single-scattering albedo

The SSA of a particle (Equation 2-14) is defined by Hapke as[7]:

The ratio of the total amount of power scattered to the total power removed from the wave is the particle single-scattering albedo, wthe single-scattering albedo are functions of wavelength.

The reflectance of a microscopic mixture is described by the reflectance function (Equation 2-18) and the average SSA of the mixture, shown in Equation 2-19. [7, 22, 32] The average SSA is a linear combination of endmember's SSAs where Ψ_k , q_k , and d_k are the mass fraction, single particle density, and average effective particle size for a given mixture component (i.e., endmember). [7]

$$w_{\lambda} = \frac{\sum_{k=1}^M (\Psi_k / q_k d_k) w_{k\lambda}}{\sum_{k=1}^M (\Psi_k / q_k d_k)} \quad (2-19)$$

The average SSA can also be represented as a relative geometric cross-section (F_k) or endmember proportion (f_k), shown in Equation 2-20 for the k^{th} component. [7] This representation is important, because often in remote sensing the particle density and particle size of endmembers is not known. Therefore, the particle density and particle size are assumed roughly equal for all endmembers. Under this assumption, the proportion of an endmember composing a mixed pixel's spectra (i.e., the relative geometric cross-section of the pixel composed of the endmember) is equal to its mass fraction.

$$F_k = f_k = \frac{(\Psi_k/q_k d_k)}{\sum_{k=1}^M (\Psi_k/q_k d_k)} \quad (2-20)$$

Using the relative geometric cross-section representation for each endmember, the equation for the average effective SSA can be written as Equation 2-21. This formulation leads to constraints similar to those of macroscopic mixing in the reflectance domain: $f_k \geq 0$ and $\sum_{k=1}^M f_k = 1$.

$$w_\lambda = \sum_{k=1}^M f_k w_{k\lambda} \quad (2-21)$$

Existing Endmember and Proportion Estimation Methods

Until recently, microscopic mixtures research was largely confined to the fields of geophysics and spectrography. The principal data source in these fields of research has been either laboratory data of known microscopic mixtures or telescopic data collected from lunar surfaces known to be dominated by microscopic mixing. [20, 22, 30-32, 34] Consequently, most published works for estimating endmembers and proportions of microscopic mixtures require severely limiting assumptions. These assumptions prevent most existing methods of endmember and proportion estimation for microscopic mixtures from being feasible for real-world HSI scenes. The following sections describe the existing methods for endmember and proportion estimation of microscopic mixtures.

Endmember estimation

A large majority of endmember and proportion estimation methods rely on the endmembers being provided *a priori*. [23-25, 32, 35, 37] Only two published methods were found to estimate endmembers from microscopic mixtures. [26, 27, 29] Both

methods however, assume that all pixels are formed from one mixture type (macroscopic or microscopic) and require the pure-pixel assumption.

Each of these methods is a two-step process. First, the given hyperspectral data is converted into SSA using a reflectance function appropriate for the given data. [26, 27, 29] In most applications the BRDF is used for this conversion, however Smith, Johnson, and Adams used data collected from a hemispherical detector and therefore used a directional-hemispherical model of reflectance. In either case, the given reflectance data was converted to average SSA.

Secondly, both methods use a common LMM endmember estimation technique on the converted SSA data. Smith, Johnson, and Adams use principal component analysis (PCA) to find the endmembers, assuming a pure-pixel exists. [26, 29] Using an eigenvalue approach on the converted SSA data and the original reflectance data, the algorithm determines if the entire data set is best modeled using SSA or reflectance. Thus, the algorithm determines the endmembers and the mixture type of the data set as a whole. Jose, et al. use the simplex identification via split augmented Lagrangian (SISAL) algorithm to estimate endmembers in the converted SSA data. [27] As with the PCA method, the SISAL algorithm requires a pure-pixel assumption.

These algorithms represent a first attempt to estimate endmembers from microscopically mixed data. However, they both require that the data contains only macroscopic or microscopic mixtures. This assumption makes these methods invalid for data sets collected over a scene of more than one mixture type.

Proportion estimation

In 2010 Broadwater and Banerjee introduced the first algorithm capable of unmixing hyperspectral data composed of macroscopic and microscopic mixtures. [24,

25] Until then all methods of microscopic mixture proportion estimation required the same assumption as the microscopic mixture endmember estimation methods; all data sets must contain only macroscopically mixed data or microscopically mixed data. [22, 26, 27, 29, 32, 33, 35] Of these approaches, two are commonly referenced for comparison with new techniques of unmixing, Mustard and Pieters's least squared error (LSE) unmixing of SSA data[32] and Guilfoyle, et al. use of a radial basis function neural network (RBFNN)[35]. In the following sections these two approaches will be discussed. Next, the Hopfield neural network/ multi-layer perceptron (HNN/MLP) nonlinear mixture model of Plaza, et al.[37] will be introduced and discussed; the results of this paper are also used for comparison with new microscopic unmixing algorithms. Finally, the physics-based kernel approaches of Broadwater and Banerjee will be presented. [23-25]

LSE. Mustard and Pieters collected highly accurate laboratory bidirectional reflectance measurements of various crushed mineral species, known to mix microscopically. [32] Two of these binary mineral mixtures have become a de facto standard for assessing the accuracy of microscopic mixture proportion estimation. [23, 24, 32, 35, 37] To unmix these mineral mixtures, Mustard and Pieters used the BRDF of Equation 2-18 to convert the hyperspectral reflectance data to SSA. Once transformed to SSA a LMM is assumed with a given set of endmember spectra, likewise converted to SSA. Using this SSA data and endmembers, a LSE approach was used to solve the inversion problem for estimating proportions. [32] Mustard and Pieters noted that in a subset of mineral mixtures, a sum-to-one constraint was not needed in the

inversion, however when Magnetite was used in a mixture the sum-to-one constraint was required.

RBFNN. Guilfoyle, et al. used an RBFNN to interpolate the microscopic proportions based off a given training set. [35] The RBFNN approach takes as input the endmembers used in the given mixture. Using the approximation of Hapke's BRDF (Equation 2-18) a set of training reflectance spectra are created from the microscopic mixing of the given endmembers. The proportions used to create the training microscopic mixture data are randomly selected. The constructed microscopic mixture spectra are used as centers for the radial basis functions used in the RBFNN. The weights of the RBFNN are then updated using the known mixing proportions of the created mixture spectra. This RBFNN, constructed with microscopic mixture data, is labeled the radial basis function nonlinear (RBF-NL) network. For comparison of results, a radial basis function linear (RBF-L) network was created using the same technique as the RBF-NL network. The RBF-L was created with training data constructed using the LMM instead of the BRDF.

To estimate mixture proportions, a hyperspectral sample is taken as input to the trained RBFNNs. The RBF-NL and RBF-L each output a set of estimated proportion values for the input sample. [35] In the paper, Guilfoyle, et al. did not discuss a method to determine which RBFNN output should be used. The mean squared error (MSE) of the reflectance experiment laboratory (RELAB) data used with the RBFNNs (and the known mixture proportions) compares the networks to each other and to Mustard and Pieters LSE approach. It was concluded that on the RELAB data, the RBF-NL network outperformed the RBF-L network and the RBF-NL performed similarly to Mustard and

Pieters. [35] These results are not surprising due to the fact that they both use the same BRDF to estimate microscopic mixtures, take endmembers as input to the unmixing, and assume that a data set contains only one mixture type (macroscopic or microscopic). [32, 35]

HNN/MLP. Plaza, et al. were the first to publish an approach to proportion estimation assuming that macroscopic and microscopic mixtures could be present in a given scene, or data set. [37] This approach requires the endmembers be supplied externally to the algorithm. In the case of the RELAB data the endmembers were given as input, for HSI scenes the automated morphological endmember extraction algorithm was used to find endmembers as a preprocessing step.

Once a set of endmembers has been established, the HNN/MLP first uses a Hopfield neural network (HNN) to unmix the macroscopic proportions (referred to in the paper simply as the “linear part of the mixing problem”). [37] The HNN uses gradient-descent learning based on error minimization. [37] The HNN uses an iterative process. Once a convergence criterion is met the HNN outputs a set of estimated linear mixing proportions.

The output proportions from the HNN are used as inputs to the multi-layer perceptron (MLP). The MLP is used to refine the linearly estimated proportions of the HNN to account for the nonlinearity in the data. The MLP is constructed using the known proportions of the training data with back-propagation and an adjustable learning rate. This fact reveals a fatal flaw in this approach. Instead of using a model to estimate the proportions from a known endmember set, this approach must use actual microscopic mixture data to interpolate proportions of new mixture data. This level of

highly accurate ground truth is seldom available for large data sets or aerial HSI collections (the author is unaware of the existence of any such collection). Plaza, et al. ran experiments to determine the amount of training data required by their algorithm to successfully unmix the RELAB data. [37] Their experiments showed that to make accurate proportion estimations, three to five samples were required from the RELAB data sets; the binary mixture RELAB data sets that were used contained only five samples.

Physics-based kernels. In machine learning literature kernel techniques are often used to model nonlinear systems. [92, 93] This ability to effectively model linear and nonlinear data has made kernels popular in hyperspectral research as well. Kernels have primarily been used in HSI research for classification applications. [94] However, kernels have also been used to estimate endmembers and proportions in hyperspectral data. [23-25, 39-41] The kernels used in these approaches were typically developed in the machine learning field for use in nonlinear problems in which the underlying relationships between data points was not known. Therefore, these kernels were generic and not specifically suited to unmixing when the underlying mixture model is known.

Broadwater and Banerjee developed a physics-based kernel, shown in Equation 2-22, in which the function Φ is a mapping from reflectance to SSA based on the BRDF of Equation 2-18. [23] The physics-based kernel was compared to three common generic kernel functions: the linear kernel, the polynomial kernel, and the radial basis function (RBF). They demonstrated, using the RELAB binary mixtures, that the physics-based kernel was better suited to proportion estimation of microscopic mixtures. [23]

Additionally, they compared the proportions estimated with the physics-based kernel to those estimated using the RBFNN and the HNN/MLP. When comparing across both RELAB data sets used, the physics-based kernel was able to more accurately estimate the proportions. [23]

$$K_\gamma(\mathbf{x}, \mathbf{y}) = \Phi^T(\mathbf{x}, \gamma)\Phi(\mathbf{y}, \gamma) \quad (2-22)$$

The physics-based kernel however, has similar limitations to the previously discussed methods. Namely, the endmembers must be externally supplied and the input data is assumed to be entirely microscopically mixed. Subsequent papers, by Broadwater and Banerjee, acknowledged the need for an approach that accounted for macroscopic and microscopic mixtures within a single algorithm, which lead to the generalized kernel for areal (macroscopic) and intimate (microscopic) mixtures (areal/intimate kernel). [24, 25]

This kernel, shown in Equation 2-23, will approximate the LMM when γ is very small and the BRDF (Equation 2-18) when γ is large. [24] To estimate the proportions of hyperspectral data, kernel fully-constrained least squares (KFCLS) is used with the areal/intimate kernel, shown in Equation 2-24. The γ parameter is optimized by minimizing the objective function shown in Equation 2-25.

$$K_\gamma(\mathbf{x}, \mathbf{y}) = (1 - e^{-\gamma x})^T(1 - e^{-\gamma y}) \quad (2-23)$$

$$\hat{\mathbf{p}} = \arg \min_{\mathbf{p}} \frac{1}{2} (K(\mathbf{x}, \mathbf{x}) - 2\hat{\mathbf{p}}^T K(\mathbf{E}, \mathbf{x}) + \hat{\mathbf{p}}^T K(\mathbf{E}, \mathbf{E})\hat{\mathbf{p}}), \quad s. t. \forall_i p_i \geq 0 \quad (2-24)$$

$$\hat{\gamma} = \arg \min_{\gamma} \frac{1}{2} (K_\lambda(\mathbf{x}, \mathbf{x}) - 2\hat{\mathbf{p}}_\lambda^T K_\lambda(\mathbf{E}, \mathbf{x}) + \hat{\mathbf{p}}_\lambda^T K_\lambda(\mathbf{E}, \mathbf{E})\hat{\mathbf{p}}_\lambda) \quad (2-25)$$

Hyperspectral Nonlinear Mixture Models

In recent years, the existence of nonlinear mixtures within HSIs has become generally accepted as fact. [1, 7, 16, 22-25, 30, 32, 39, 42-44, 60, 65, 70, 95-105] Microscopic mixtures are one cause of nonlinear mixing. Therefore, the BRDF is used to model nonlinear mixtures, of this type. [1, 7, 23-25, 30, 32, 37] However, nonlinear mixtures are also caused by multiple reflections and transmissions from scattering surfaces. [14-16, 18, 19] This results in a new model for nonlinear mixtures of this type. [13, 14] Additionally, general machine learning nonlinear models have been used to account for nonlinearity present in HSIs. [23-25, 35-38, 40-44, 59-62, 65, 93-99, 102, 106-119] This section presents an overview of nonlinear models, excluding those based on the BRDF, used in hyperspectral mixture analysis.

Virtual Endmembers

Nonlinear mixtures in hyperspectral data can be caused by multiple reflections and transmissions between scattering surfaces. [8-18, 20] This nonlinear mixing in hyperspectral data is often referred to as multi-scattering, forward-scattering, or back-scattering. This form of scattering occurs when light is reflected off one surface and strikes a second and even third surface. [11, 14, 15, 18] In turn the light striking the second or third surface is reflected in such a way that it is then detected by the sensor. In this scenario the second or third surface can also be illuminated directly, by the light source, causing a normal reflection in addition to the multi-scattering reflection. [8-15, 18, 19]

This form of nonlinear mixing causes additional photon interactions on the second and third surfaces. [8-15, 18, 19] The light incident on a given area of the second surface is now greater than that of the area of surface not impacted by multi-scattering.

Secondly, the multiplicatively scattered light impacting the second surface does not have the same signature as the light being emitted over the scene. Therefore, a multiplicative filtering effect is created on the second and third surfaces. [8-15, 18, 19]

In hyperspectral literature this nonlinear mixture is addressed using a variety of techniques. [8-15, 18, 19] These methods all attempt to model single scattering components with traditional endmembers and multiple-scattering components with what has been termed a virtual endmember. [8-15, 20] Simply put, a virtual endmember is the second and third order polynomial expansion of the endmembers of a given scene. As shown by Equation 2-26, a virtual endmember attempts to model the multiple scattering components by the element-wise product of two endmembers.

$$\text{Virtual Endmember} = \mathbf{e}_1 \odot \mathbf{e}_2 \quad (2-26)$$

Through the use of the virtual endmember, this nonlinear mixing becomes linear in the proportion values assigned to the endmembers and virtual endmembers. Using this concept endmember extraction and unmixing efforts are again framed as a LMM problem. [8-15, 18, 19] The various papers that address this model use an assortment of techniques to determine which endmembers to specifically model as virtual endmembers or methods to better account for the physical basis of the model. A common technique is to relax the constraints on the proportion values to allow the model to account for the extra photon interactions. [8-15, 18, 19]

Kernel Methods for Endmember and Proportion Estimation

Kernel methods are naturally suited to solving nonlinear problems. By projecting data points into a nonlinear kernel-space, relationships in the original feature-space may become linear. [92, 93] The methods rely on an appropriate kernel function to represent the similarity or dissimilarity between data points. [120, 121] Typically the RBF is used

because of its direct utilization of squared distance between points. [23] However kernel functions have been specifically designed to model hyperspectral data, such as the angular kernel[94], or recent work by Broadwater and Banerjee in which a kernel was proposed to model intimate mixtures[23, 24]. Within hyperspectral image analysis, kernel methods are typically used for ground cover classification [102-105, 113, 122, 123], however recent attempts have been made to estimate endmembers and proportions within the kernel-space. [23-25, 39-41]

Extraction of endmembers in the kernel-space was done by using the support vector data description (SVDD) algorithm to find the data points that surround the remaining points. [39] Proportions of these candidate endmember points could be used to fully explain the data. While this approach did allow for nonlinear extraction of possible endmembers that describe the data, there is no basis in the model to determine that these points are in fact endmembers. This model fits a common theme in which the data is explained via a given model but little to no connection is made with the underlying physics that created the data.

Estimation of proportions in the kernel-space is similar to estimation in the feature-space. [40] While using kernels does allow for nonlinear relationships, these estimation methods are not founded on principles of the underlying system that created the data. As hyperspectral endmember and proportion estimation is an underdetermined inversion problem, many possible solutions can be found that fit the data. [1, 3]

Neural Network Based Proportion Estimation

As with kernel based methods, neural networks provide a technique that is capable of modeling linear and nonlinear relationships in the given data. [93] Typically, neural networks are used for ground cover classification in hyperspectral literature but

also have a known capability to learn unknown functions. [35-38, 92, 93] This takes the form of passing inputs to the function into the neural net and training it with desired outputs of the function. Once the neural network is trained, new inputs are given. The expectation is that if the neural network is properly trained, for the new inputs, then the proper function output will result (i.e., the neural network will approximate a nonlinear mixing function in hyperspectral data).

Neural network proportion estimation makes the assumption that an unknown nonlinear function (f) defines the interaction between endmembers (\mathbf{E}) and proportions (\mathbf{p}), shown in Equation 2-27. [36-38] To learn this function training data is used consisting of a set of candidate endmembers and given proportions. This technique is also used as a refinement step after a LMM endmember extraction and unmixing method is used. [37, 38]

$$\mathbf{x}_i = f(\mathbf{E}, \mathbf{p}) + \epsilon_i \quad (2-27)$$

The nonlinear function being approximated by the neural network is assumed unknown and therefore not explicitly modeled. As mentioned before, this means that this approach is not constrained by the physical theories of reflectance and therefore is not likely to accurately model this system when interpolating hyperspectral data. In addition, this technique also requires a given set of endmembers and proportions in order to train the network, either hand-chosen or output from a previously run model.

Manifold Learning in Hyperspectral Data

In recent years, manifold learning has become a popular method to deal with nonlinearities in hyperspectral data. [100, 124, 125] This is primarily due to the manifold's ability to represent an underlying lower-dimensional linear or nonlinear

structure containing the data in a higher dimensional feature space. Exploiting this intrinsic structure allows the hyperspectral data to be expressed in a lower-dimensional space while preserving the underlying structure of the data. [42-44, 95, 97-99, 101-105, 112, 113, 115-119, 122]

The manifold learning trend in hyperspectral literature began with three articles published in “Science” magazine December 2000. [100, 124, 125] These articles discussed applications of manifold learning to nonlinear dimensionality reduction of high-dimension data sets. In addition to showing the utility of these methods, the isometric feature mapping, or ISOMAP, algorithm was introduced. [125] The ISOMAP algorithm became the basis of the first generation of hyperspectral manifold based techniques. [95-98, 101, 115-119]

Similar to many of the other nonlinear approaches to modeling hyperspectral data, manifold learning is not based on a physical model of the system being sensed. This fact limits endmember extracting and unmixing abilities with models based solely upon learning the manifold structure embedding the hyperspectral data. However, the manifold’s ability to represent an underlying nonlinear structure in a high-dimensional space does make manifold learning ideal for supervised classification tasks[99, 101-105, 112, 113, 116-119, 122], semi-supervised classification[106, 126], bathymetry mapping[95, 97, 98, 115], intrinsic dimensionality determination[59, 60, 63], dimensionality reduction and feature extraction[61, 62, 66], anomaly detection[64, 65], and other hyperspectral image processing applications[67-70] .

ISOMAP

The ISOMAP algorithm has been the most prevalent method for learning a manifold in hyperspectral feature-space. [59, 60, 95-98, 101, 115-119, 125] The ISOMAP algorithm is composed of three steps[125]:

1. Construct a neighborhood graph from the given data. The graph can be a k -nearest neighbors graph (connect two data points, nodes, if one is a k -nearest neighbor) or an ϵ graph (connect all nodes within ϵ distance of each other).
2. Compute the shortest path on the graph between all points (nodes). If two nodes are connected by an edge then the path distance between them is the direct distance between the nodes. If two nodes are not directly connected then the path distance is the sum of edges composing the shortest path between the two nodes.
3. Construct the d -dimensional embedding by using multi-dimensional scaling (MDS) on the paths created in step 2.

Once the ISOMAP algorithm has been completed, the data will be represented by a lower-dimensional embedding (the intrinsic dimensionality) via preserving the geodesic distances of the data. Hyperspectral literature research involving this technique has focused on applying it to new problems[61, 68, 69], and making it more scalable to the large data set problems common in hyperspectral data analysis[59, 60, 96, 118, 119].

Sub-manifolds

As research has continued in applications of the ISOMAP algorithm and techniques to make it scalable for large data sets, it was discovered that the global manifold structure from a hyperspectral scene had natural partitions in the data. [59, 60, 96] Recent research has discovered that the global manifold has curvature in its structure; as a result of these curves the local intrinsic dimensionality of the data is

higher than that of the global manifold. Using this information the manifold can be partitioned into sub-manifolds. [59, 60, 96]

It was also discovered that these sub-manifolds had different properties and thus used a different optimal parameter for constructing the ISOMAP nearest neighbor graph. Use of different parameters for the sub-manifolds resulted in increased effectiveness of the manifold techniques. [96] Investigation was not done into what causes the curvature, or the sub-manifolds that exhibit different properties in the feature-space, but it could be hypothesized that these represent different mixtures in the hyperspectral image scene.

Manifold-based endmember estimation

In the past year research has been published in which a manifold structure was assumed for the hyperspectral data and endmember extraction was attempted on the manifold. [42-44] The nonlinear mixing was assumed to be an unknown function that warps the LMM, as shown in Equation 2-28.

$$\mathbf{x}_i = \text{func} \left(\sum_{k=1}^M p_{ik} \mathbf{e}_k \right) \quad (2-28)$$

To extract endmembers using this assumption a simplex volume maximization approach was used. In this algorithm, hyperspectral data points are randomly chosen and the volume calculated with those points as the vertices. At each iteration a new point is substituted for an existing vertex. If the new vertex creates a larger volume it is kept as a candidate endmember, otherwise the old vertex is used in the next iteration. This technique is altered to work with the manifold structure by using the geodesic distances between points instead of their feature-space distances. [43] This allows the

endmember extraction algorithm to model nonlinearity in the distances between data points.

This approach represents a first concept in attempting to exploit the manifold structure of the data for endmember extraction. However, it fails to model the nonlinearities in a system constrained by the mixtures creating the data, thus there is no guarantee that the inversion process will create a physically probable set of endmembers to explain the hyperspectral scene. Further, by using the simplex volume maximization method it inherently relies on the pure-pixel assumption, which can be problematic.

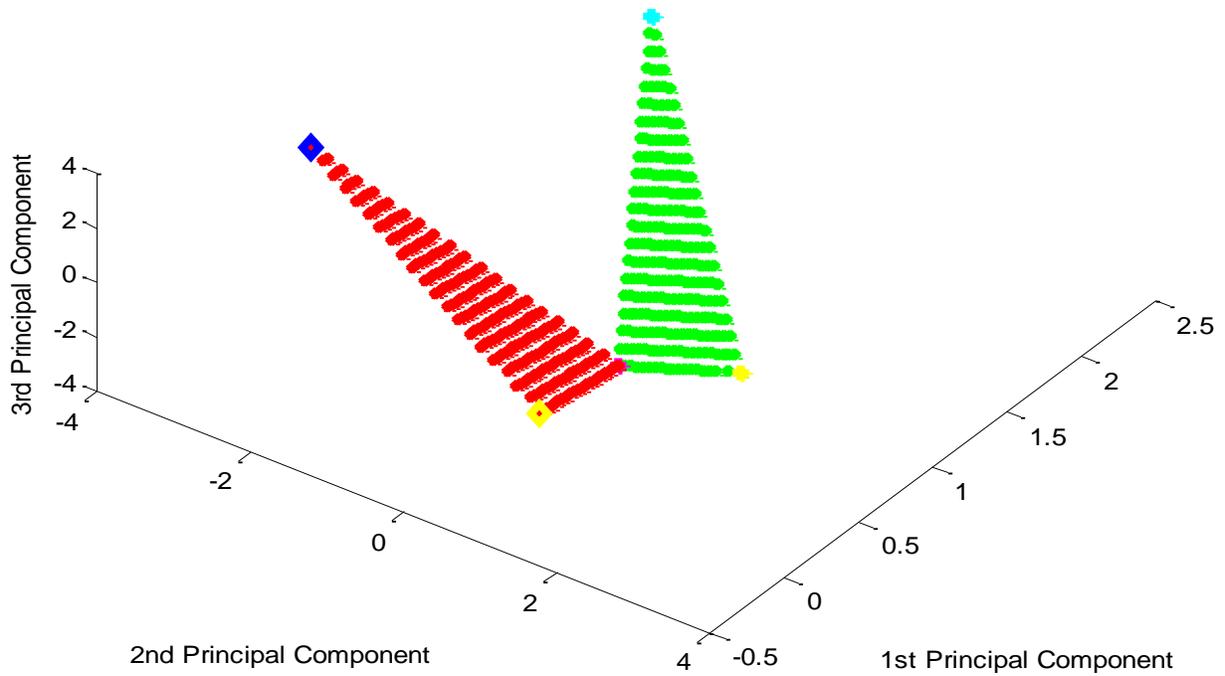


Figure 2-1. Two linear simplexes formed from macroscopic mixtures of five endmembers with uniform proportions.

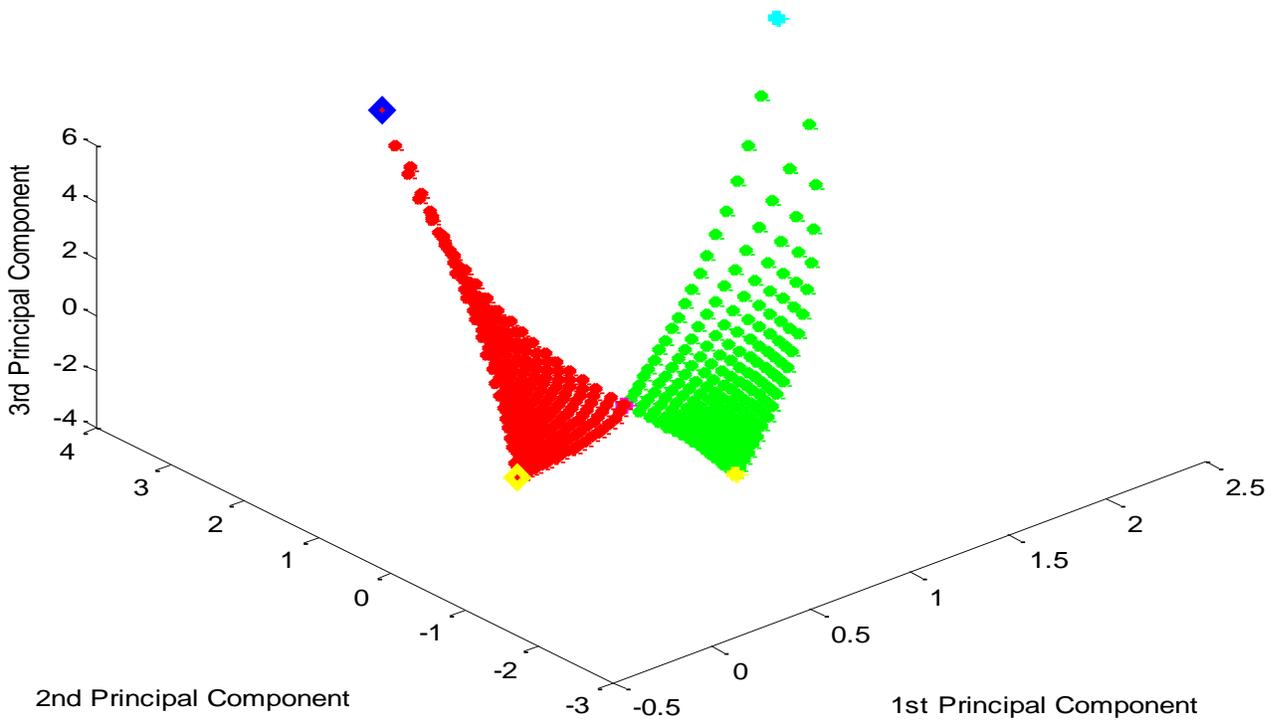


Figure 2-2. Two nonlinear simplexes formed from microscopic mixtures of five endmembers with uniform proportions.

CHAPTER 3 TECHNICAL APPROACH

New methods for hyperspectral endmember and proportion estimation are introduced in this chapter. Founded on the models derived from reflectance spectroscopy, these new algorithms incorporate nonlinear microscopic mixtures into existing linear models for macroscopic mixtures. The microscopic mixture model describes the physics of how light incident on a surface will mix between particles of different endmembers. As a result, these models represent a wider range of physical mixtures present in an HSI. Experiments in Chapter 4 demonstrate that these new algorithms allow for increased accuracy in estimating endmembers and proportions.

The first algorithm introduced is the discrete mixture estimation (DME) method. The DME labels a pixel as being best described by either a macroscopic or microscopic mixture. Using this label, the endmembers and their respective proportions are estimated with the appropriate mixture model.

Next a new HSI pixel model is introduced, the multi-mixture pixel (MMP). The MMP model represents each of the spectra in HSI pixels as being produced by a mixture of mixtures. Thus, a pixel is composed of a macroscopic mixture of endmembers and a microscopic mixture. The MMP is discussed within the contexts of its associated algorithm, the multi-mixture pixel estimation (MPE) method.

Review of Macroscopic and Microscopic Mixtures

A brief review of macroscopic and microscopic mixtures is presented in this section. A more comprehensive description of these mixtures and their associated models is given in Chapter 2.

Macroscopic Mixtures

Macroscopic mixing occurs when two or more discrete endmembers reside within a single pixel's instantaneous field of view. This causes a linear mixing of the spectral reflectance signatures from each of the endmembers. The macroscopic mixture is generally modeled with the LMM shown in Equation 3-1, where p_{ik} is the proportion of endmember e_k for the given pixel x_i with additive zero-mean Gaussian noise ϵ_i . [1, 3] The LMM is constrained as given by Equation 3-2. This type of mixing is a result of the finite spatial resolution of the sensor and does not indicate a physical mixing or interaction between endmembers. [1]

$$x_i = \sum_{k=1}^M p_{ik} e_k + \epsilon_i \quad (3-1)$$

$$\forall_{ik} p_{ik} \geq 0 \text{ and } \forall_i \sum_{k=1}^M p_{ik} = 1 \quad (3-2)$$

Geometrically, ignoring the noise term, the LMM forms a linear simplex in the \mathcal{R}^D feature-space, where each of the D dimensions in the hyperspectral feature vector corresponds to a wavelength (or band) measured by the sensor. Two such simplexes are illustrated in Figure 2-1. Each simplex is defined by its vertices, which, in the case of HSI analysis, are the endmembers.

Microscopic Mixtures

Microscopic mixtures (or intimate mixtures) occur when the particles of two or more endmembers are homogeneously intermixed together such that particles of the component endmembers are in close proximity to each other. [1] The light incident on the mixed surface is scattered between the intermixed endmember's particles. This phenomenon, called multi-scatter, creates a nonlinear mixing in reflectance. [7]

Microscopic mixtures represent a physical mixing of endmembers within the scattering medium. [1]

Reflectance of the microscopic mixture can be modeled by the nonlinear reflectance function, shown in Equation 3-3 and Equation 3-4, where w_λ is the average single-scattering albedo (SSA or simply albedo) between endmembers, θ_i the angle of incidence, and θ_e is the angle of emergence. [7, 30] As light is multi-scattered between endmember's particles, their SSAs linearly mix as shown in Equation 3-5 and Equation 3-6, where f_k is the proportion of the k^{th} endmember. [7] In these equations the SSA is shown with a λ subscript to signify the wavelength dependent properties of SSAs. This reflectance equation was developed by Hapke and Mustard using various remote sensing assumptions that have been validated through experimentation (see Chapter 2 for details). [1, 7, 22, 30-32]

$$R(w_\lambda) = \frac{w_\lambda}{4(c_i + c_e)} H(c_i, w_\lambda) H(c_e, w_\lambda) \quad (3-3)$$

$$c_i = \cos(\theta_i); \quad c_e = \cos(\theta_e) \quad (3-4)$$

$$w_\lambda = \sum_{k=1}^M f_k w_{k\lambda} \quad (3-5)$$

$$\forall_k f_k \geq 0 \text{ and } \sum_{k=1}^M f_k = 1 \quad (3-6)$$

The reflectance function (Equation 3-3) uses an approximation to Chandrasekhar's function for isotropic multi-scattering, shown in Equation 3-7.

$$H(c_{[i,e]}, w_\lambda) = \frac{1 + 2c}{\left(1 + 2c(1 - w_\lambda)^{\frac{1}{2}}\right)} \quad (3-7)$$

The derivative of Equation 3-3, with respect to the SSA (w_λ), is shown in Equation 3-8. Inspection of Equation 3-8 leads to the conclusion that the derivative is always greater than 0, since $w_\lambda \in [0,1)$ as defined by Hapke's model and all other quantities are nonnegative. [30] Figure 3-1 demonstrates this over the range of SSA values. Thus, the reflectance function (Equation 3-3) is monotonically increasing.

$$\frac{\partial R}{\partial w_\lambda} = \frac{H(c_i, w_\lambda)H(c_e, w_\lambda)}{4(c_i + c_e)} \left(1 + \frac{w_\lambda c_i}{(1 + 2c_i(1 - w_\lambda)^{1/2})(1 - w_\lambda)^{1/2}} + \frac{w_\lambda c_e}{(1 + 2c_e(1 - w_\lambda)^{1/2})(1 - w_\lambda)^{1/2}} \right) \quad (3-8)$$

A microscopic mixture can be seen in Figure 2-2, using the same endmembers and proportions as the macroscopic mixture in Figure 2-1. Geometrically, the microscopic mixture forms a perturbed simplex (i.e., warping of the macroscopic mixture linear simplex). However, since the same endmembers are used for both mixtures, the vertices of the microscopic mixture warped simplex are the same as the macroscopic mixture linear simplex. Additionally, inspection of Figure 2-1 and Figure 2-2 reveals the non-uniform distribution of sample points, created from uniform proportions, caused by the microscopic mixture. Specifically, the sample points are densest near endmembers with low albedo. In reflectance spectroscopy, this is known as the spectral dominance of low albedo endmembers. This relationship can be seen in Figure 3-1 by observing that the slope of the derivative is always increasing and that the derivative is always less than one for any albedo below .8. The graph shown in Figure 3-1 was determined using 0° angles of incidence and emergence. Different angles of incidence and emergence, however, will decrease this spectral dominance of low albedo endmembers effect.

To further characterize the nonlinearity present in microscopic mixtures, the following example is given. Assume two synthetic endmembers of three bands each. The first bands of each endmember, and nine macroscopic mixture points created from uniform proportions, are shown in Figure 3-2. Notice that the reflectance values for each mixture point are linearly related. Figure 3-3 shows the first band of the same two endmembers microscopically mixed with the proportions used in Figure 3-2. Notice that the mixture points are uniformly spaced along the x-axis, the albedo values. These same mixture points, however, are not uniformly spaced along the y-axis, the reflectance values. The black line in this figure illustrates the reflectance curve created from the reflectance function (Equation 3-3). Notice, that for any two albedos the mixture points between them will always have increasing reflectance values, from the lowest albedo to the highest. The reflectance values for all three bands of the microscopic mixture shown in Figure 3-3 are plotted in Figure 3-4. The mixture points between the two endmembers reside on a curved line in the 3-dimensional space. The 1-dimensional line between the two endmembers is understood as representing the $M-1$ dimensional manifold between M endmembers (where M is 2 in this example). [52] The line is curved as a result of the microscopic mixing.

A reflectance-domain microscopic mixture model (RD-MMM) is shown in Equation 3-9, where R is the reflectance function given in Equation 3-3 and the constraints of Equation 3-6 hold for all x_i . The SSA of the k^{th} endmember is shown in Equation 3-10.

$$x_i = R \left(\sum_{k=1}^M f_{ik} \mathbf{w}_k \right) + \epsilon_i \quad (3-9)$$

$$\mathbf{w}_k = R^{-1}(\mathbf{e}_k) \quad (3-10)$$

An albedo-domain microscopic mixture model (AD-MMM) derived from Equation 3-9 is shown in Equation 3-11. The additive noise terms in the RD-MMM (ϵ_i) and AD-MMM (β_i) are assumed a zero-mean Gaussian. [1-3, 22-25, 32] This commonly used assumption, however, cannot be accurate. Assuming ϵ_i is a zero-mean Gaussian random variable. Because the reflectance function (Equation 3-3) describing the relationship between the reflectance-domain and albedo-domain is nonlinear and monotonically increasing, the distribution describing the β_i random variable cannot be Gaussian.

The models and associated algorithms described in this section use the zero-mean Gaussian assumption for the error in both albedo and reflectance domains. However, future research could investigate the albedo-domain error distribution and its effects on microscopic mixture model estimation algorithms. Since the reflectance function (Equation 3-3) is strictly monotonically increasing, minimizing the RSS of the RD-MMM (Equation 3-9) results in the same proportions (f_{ik}) as minimizing the RSS of the AD-MMM (Equation 3-11).

$$R^{-1}(x_i) = \sum_{k=1}^M f_{ik} \mathbf{w}_k + \beta_i \quad (3-11)$$

Discrete Mixture Estimation

The first method developed in this research is the DME algorithm. This algorithm constitutes a step forward in HSI spectroscopy methods that explicitly include macroscopic and microscopic mixtures. DME uses a pixel-level approach to label each input HSI pixel or data sample as either macroscopically or microscopically mixed. Previously published methods to include both mixture models required an image-level

estimation of mixture type, i.e., an HSI was entirely macroscopically or microscopically mixed. [26, 29, 32, 35] Recently Broadwater and Banerjee created a kernel function that allowed for a pixel-level approach to estimating mixture types. [24, 25] This physics-based kernel approach relies on an approximation of the reflectance function and externally provided endmembers. [23-25] A comprehensive survey of microscopic endmember and proportion estimation models and algorithms is presented in Chapter 2.

Using the RD-MMM constrains the endmember and proportion estimation inversion problem to a strict physics-based model. DME eliminates the assumption of a single mixture type within an HSI, without the need to approximate the reflectance function. In addition to proportion estimation, DME allows for direct estimation of endmembers in the presence of both mixture types. Use of the ICE framework allows DME to estimate endmembers without the pure-pixel assumption, as is required with existing microscopic mixture endmember estimation methods. [3, 26, 29]

Proportion Estimation

To estimate proportions using DME, a set of endmembers must be provided (later sections will describe how the endmember set is estimated using DME). Using these endmembers, the proportions of each pixel will be estimated. A pixel-level indicator variable is used to label the mixture type of each pixel. The RSS objective function used by DME is given by Equation 3-12. In this model the RSS for the macroscopic mixture (RSS_i^{MAC}), derived from the LMM, is given by Equation 3-13. The RSS for the microscopic mixture (RSS_i^{MIC}), derived from the RD-MMM, is shown in Equation 3-14. The variable ($t_{[1,2]i}$) determines the mixture type that represents the i^{th} pixel.

$$RSS = \sum_{i=1}^N \left(t_{1i}(RSS_i^{MAC}) + t_{2i}(RSS_i^{MIC}) \right) \quad (3-12)$$

$$RSS_i^{MAC} = \left(\mathbf{x}_i - \sum_{k=1}^M p_{ik} \mathbf{e}_k \right)^t \left(\mathbf{x}_i - \sum_{k=1}^M p_{ik} \mathbf{e}_k \right) \quad (3-13)$$

$$RSS_i^{MIC} = \left(\mathbf{x}_i - R \left(\sum_{k=1}^M f_{ik} \mathbf{w}_k \right) \right)^t \left(\mathbf{x}_i - R \left(\sum_{k=1}^M f_{ik} \mathbf{w}_k \right) \right) \quad (3-14)$$

DME relies on the assumption that a pixel is largely dominated by a single mixture type. In its current configuration DME labels a pixel as either a macroscopic or microscopic mixture; however it is amenable to adding new mixture terms. This allows future modifications to include additional spectral phenomena or mixtures. The indicator variables ($t_{[1,2]i}$) are determined by assigning the minimum RSS mixture term $t_{[1,2]i} = 1$ and the remaining terms 0, for all i pixels.

The macroscopic proportions (p_{ik}) are estimated using quadratic programming to minimize RSS_i^{MAC} (Equation 3-13). However, the microscopic proportions (f_{ik}) appear in the argument to the nonlinear reflectance function. Consequentially, quadratic programming cannot be used with Equation 3-14. Therefore, the microscopic proportions are estimated from the albedo-domain RSS ($RSS_i^{MIC-Albedo}$) derived from the AD-MMM (Equation 3-11). The microscopic proportions are estimated using quadratic programming to minimize Equation 3-15.

$$RSS_i^{MIC-Albedo} = \left(R^{-1}(\mathbf{x}_i) - \sum_{k=1}^M f_{ik} \mathbf{w}_k \right)^t \left(R^{-1}(\mathbf{x}_i) - \sum_{k=1}^M f_{ik} \mathbf{w}_k \right) \quad (3-15)$$

The proportion estimation piece of DME is as follows:

1. Take as input a set of pixels from an HSI scene and a set of endmembers

2. Use quadratic programming to estimate the macroscopic proportions (p_{ik} 's) by minimizing Equation 3-13
3. Use quadratic programming to estimate the microscopic proportions (f_{ik} 's) by minimizing Equation 3-15
4. Assign the indicator variables ($t_{[1,2]i}$'s) by setting the indicator variable to 1 corresponding to the minimum RSS term from Equation 3-12 and the rest 0

Endmember Estimation

DME is able to use a set of endmembers supplied externally, such as from another endmember estimation algorithm or library of spectral signatures. However, in many applications a full set of spectral signatures from a given image may not be available. Many endmember estimation algorithms also rely on the pure-pixel assumption. This assumption, however, is often not valid for all endmembers present in an HSI.

The ICE framework is used in DME to estimate the endmembers from the HSI, versus selecting pixels as endmembers. The inclusion of the RD-MMM, along with the LMM, allows DME to utilize implicit endmember information from macroscopic and microscopic mixtures. DME uses the RSS objective function (Equation 3-12) within the regularized ICE framework, discussed in Chapter 2, to estimate the endmembers as shown in Equation 3-16. [3] The SSD between the endmembers, shown in Equation 3-17, is used to regularize endmember estimation. The μ parameter controls the tradeoff between the RSS and SSD terms (Equation 3-16).

$$RSS_{reg} = (1 - \mu) \frac{RSS}{N} + \mu SSD \quad (3-16)$$

$$SSD = \sum_{j=1}^D \mathbf{e}_j^T (M \mathbf{I}_M - \mathbf{1} \mathbf{1}^T) \mathbf{e}_j \quad (3-17)$$

To estimate endmembers Newton's method is used, as shown in Equation 3-18 for the j^{th} endmember, where η is a learning-rate. [93] The derivative of RSS_{reg} with respect

to endmember \mathbf{e}_j is given by Equation 3-19 , where $E = [\mathbf{e}_1 | \dots | \mathbf{e}_M]$ and $W = [\mathbf{w}_1 | \dots | \mathbf{w}_M] = [R^{-1}(\mathbf{e}_1) | \dots | R^{-1}(\mathbf{e}_M)]$. In this equation, \mathbf{u}_i is the derivative of the reflectance function (Equation 3-8) evaluated at the albedo-domain microscopic mixture, as given by Equation 3-5, (i.e., $\mathbf{u}_i = \left[\frac{\partial R}{\partial w_{\lambda_1}}(w_{\lambda_1}) \quad \dots \quad \frac{\partial R}{\partial w_{\lambda_M}}(w_{\lambda_M}) \right]^T$) and \mathbf{v}_j is the slope of the inverse reflectance function evaluated at the j^{th} endmember. The second derivative of RSS_{reg} with respect to endmember \mathbf{e}_j is given by Equation 3-20. To estimate endmembers, assuming proportions are not known *a priori*, an alternating optimization technique is used between estimating endmembers and their proportions.

$$\mathbf{e}_j^{new} = \mathbf{e}_j^{old} - \eta \left(\frac{\frac{\partial RSS_{reg}}{\partial \mathbf{e}_j}}{\frac{\partial^2 RSS_{reg}}{\partial \mathbf{e}_j^2}} \right) \quad (3-18)$$

$$\begin{aligned} \frac{\partial RSS_{reg}}{\partial \mathbf{e}_j} = & -2 \frac{1-\mu}{N} \sum_{i=1}^N \left(t_{1i} p_{ij} (\mathbf{x}_i - E^{old} \mathbf{p}_i) + t_{2i} f_{ij} (\mathbf{u}_i \odot \mathbf{v}_j) (\mathbf{x}_i - R(W \mathbf{f}_i)) \right) \\ & + \frac{2\mu}{M(M-1)} \sum_{k=1, k \neq j}^M (\mathbf{e}_j^{old} - \mathbf{e}_k) \end{aligned} \quad (3-19)$$

$$\frac{\partial^2 RSS_{reg}}{\partial \mathbf{e}_j^2} = 2 \frac{1-\mu}{N} \sum_{i=1}^N \left(t_{1i} p_{ij}^2 + t_{2i} (f_{ij} (\mathbf{u}_i \odot \mathbf{v}_j))^2 \right) + \frac{2\mu}{M} \quad (3-20)$$

The complete DME algorithm is as follows:

1. Initialize by selecting a starting set of pixels as endmembers
2. Use the DME proportion estimation to estimate the proportions of each pixel with the current endmembers
3. Use a Newton step to update the endmembers
4. Repeat steps 1 – 3 until a stopping criteria is met

Multi-Mixture Pixel Estimation

Multi-Mixture Pixel Model

In the previous algorithm, DME, each pixel is assumed to be macroscopically or microscopically mixed. This assumption is valid for some HSIs. However, the assumption is violated in HSIs that contain overlapping heterogeneous regions of different mixture types. In these scenes a pixel may be composed of a macroscopic mixture, a microscopic mixture, or a combination of the two mixture types. A second violation to this assumption occurs when one or more endmembers of a microscopic mixture clumps together. These particles cause macroscopic mixing with the surrounding microscopic mixture. These observations led to the MMP model, shown in Equation 3-21.

This new model characterizes a pixel as a macroscopic mixture of endmembers and a microscopic mixture, i.e., a mixture of mixtures. The MMP model (Equation 3-21) has not been previously considered in HSI analysis. Endmembers and albedos have the same relationship as described previously in Equation 3-10.

$$\mathbf{x}_i = \sum_{k=1}^M p_{ik} \mathbf{e}_k + p_{iM+1} R \left(\sum_{k=1}^M f_{ik} \mathbf{w}_k \right) + \boldsymbol{\varepsilon}_i \quad (3-21)$$

The macroscopic proportions (p_{ik}) in the MMP model are dependent on the reflectance of the component microscopic mixture. Therefore, the macroscopic proportions are dependent on the microscopic proportions (f_{ik}). Estimation of the microscopic proportions is an ill-posed inversion problem. Ignoring noise, consider the following case, as illustrated in Figure 3-5. A MMP \mathbf{x} is composed of two endmembers, \mathbf{e}_1 and \mathbf{e}_2 . The MMP is constrained by the set of possible macroscopic mixtures between the endmembers, illustrated as a dashed blue line, and the set of possible

microscopic mixtures between the endmembers, illustrated as a solid red line. Recall that the MMP model treats the microscopic mixture as an endmember. Therefore, the MMP model can represent x with 0 residual error using e_1 , e_2 , and $r = R(\sum_{k=1}^M f_{ik} w_k)$ for any point r on the arc A . More precisely, $\forall r \in A \exists p_1, p_2, p_3: x = p_1 e_1 + p_2 e_2 + p_3 r$.

As a pixel's microscopic mixture proportion (p_{iM+1}) increases, the MMP mixture point moves closer to the microscopic mixture line, as shown in Figure 3-6. Therefore, the plausible proportions of the microscopic mixture become increasingly constrained and even unique in the case of a 100% microscopic mixture, i.e., the arc A of plausible points r shrinks. As an MMP mixture point's microscopic mixture proportion lessens, the MMP mixture point moves closer to the macroscopic mixture, as shown in Figure 3-7. This causes the plausible microscopic proportions to be less constrained, i.e., the arc A of plausible points r increases. However, as the microscopic mixture proportion decreases (i.e., the MMP is dominated by a macroscopic mixture) the microscopic mixture becomes less of a factor in the overall pixel's mixture proportions. Therefore, the error caused by the ill-posed inversion of estimating the microscopic proportions is a small factor in accurately estimating the mixture proportions.

Proportion Estimation

As with DME, proportion estimation with MPE requires a current set of endmembers to be provided. Estimation of proportions using MPE is composed of two steps. First, the reflectance signature of the microscopic mixture component of the MMP must be estimated. To determine this reflectance signature, the microscopic mixture proportions are estimated using the AD-MMM. Secondly, the macroscopic

proportions are estimated by minimizing the RSS objective function shown in Equation 3-22, derived from the MMP model (Equation 3-21).

$$\begin{aligned}
 \text{RSS} = \sum_{i=1}^N & \left(\left(\mathbf{x}_i - \sum_{k=1}^M p_{ik} \mathbf{e}_k - p_{iM+1} R \left(\sum_{k=1}^M f_{ik} \mathbf{w}_k \right) \right)^t \left(\mathbf{x}_i - \sum_{k=1}^M p_{ik} \mathbf{e}_k \right. \right. \\
 & \left. \left. - p_{iM+1} R \left(\sum_{k=1}^M f_{ik} \mathbf{w}_k \right) \right) \right)
 \end{aligned} \tag{3-22}$$

HSI pixels, described by the MMP model, reside within the region bounded by the macroscopic and microscopic mixtures of a given set of endmembers. This relationship is illustrated in Figure 3-5 and Figure 3-6. A unique estimation of the microscopic mixture proportions is not possible with the information contained within an HSI pixel. Therefore, it is likely that some amount of estimation error will be introduced into the microscopic proportion estimation. This is due to the ill-posed inversion.

The microscopic mixture proportions are estimated by using quadratic programming to minimize the RSS in Equation 3-15. This can be considered in Figure 3-5 and Figure 3-6, as the point residing on the microscopic mixture curve that is closest to the MMP mixture point. The macroscopic mixture proportions of the endmembers and the microscopic mixture are estimated by using quadratic programming to minimize the RSS objective in Equation 3-22. The proportions estimation component of MPE is as follows:

1. Take as input a set of pixels from an HSI and a set of endmembers
2. Use quadratic programming to estimate the microscopic mixture proportions (f_{ik} 's) by minimizing Equation 3-15

3. Use quadratic programming to estimate the macroscopic mixture proportions (p_{ik} 's) by minimizing Equation 3-22

The resulting proportions are interpreted as follows. The macroscopic proportions 1 through M ($p_{i1} \cdots p_{iM}$) represent the proportions of endmembers macroscopically mixed. The $M+1$ macroscopic proportion (p_{iM+1}) is the estimated proportion of the pixel composed of a microscopic mixture. Therefore, $p_{iM+1}f_{ik}$ is the proportion of the pixel described by a microscopic mixture of the k^{th} endmember.

Endmember Estimation

Similar to the DME, MPE can use externally provided endmembers from either a spectral library or an independent endmember estimation technique. In many situations spectral libraries are unavailable and external methods fail due to pure-pixel or linear model assumptions. MPE uses the MMP model to estimate endmembers from the macroscopic and microscopic mixture information inherently contained in an HSI pixel.

Estimation of endmembers using MPE utilizes the ICE regularized framework as shown in Equation 3-16 and Equation 3-17. [3] The endmembers are estimated using Newton's method (Equation 3-18). The derivative of RSS_{reg} for the j^{th} endmember is shown in Equation 3-23, where $E = [e_1 | \cdots | e_M]$ and $W = [w_1 | \cdots | w_M]$
 $= [R^{-1}(e_1) | \cdots | R^{-1}(e_M)]$. In this formulation u_i is the derivative of the reflectance function (Equation 3-8) at the albedo-domain microscopic mixture (i.e., $u_i = \frac{\partial R}{\partial w_\lambda}(Wf_i)$) and v_j is the slope of the inverse reflectance function of the j^{th} endmember. The second derivative of RSS_{reg} is given by Equation 3-24. To estimate endmembers, assuming proportions are not known *a priori*, an alternating optimization technique is used between estimating endmembers and their proportions.

$$\begin{aligned} \frac{\partial RSS_{reg}}{\partial \mathbf{e}_j} = & -2 \frac{1-\mu}{N} \sum_{i=1}^N \left((p_{ij} + p_{iM+1} f_{ij} \odot \mathbf{v}_j \odot \mathbf{u}_i) (\mathbf{x}_i - E^{old} \mathbf{p}_i - p_{iM+1} R(W\mathbf{f})) \right) \\ & + \frac{2\mu}{M(M-1)} \sum_{k=1; k \neq j}^M (\mathbf{e}_j^{old} - \mathbf{e}_k) \end{aligned} \quad (3-23)$$

$$\frac{\partial^2 RSS_{reg}}{\partial \mathbf{e}_j^2} = 2 \frac{1-\mu}{N} \sum_{i=1}^N (p_{ij} + p_{iM+1} f_{ij} \odot \mathbf{v}_j \odot \mathbf{u}_i)^2 + \frac{2\mu}{M} \quad (3-24)$$

The complete MPE algorithm is as follows:

1. Initialize by selecting a starting set of HSI pixels as the endmembers
2. Use the MPE proportion estimation algorithm to estimate the proportions of each pixel with the current endmembers
3. Use Newton's method to update the endmembers
4. Repeat steps 1 – 3 until a stopping criteria is met

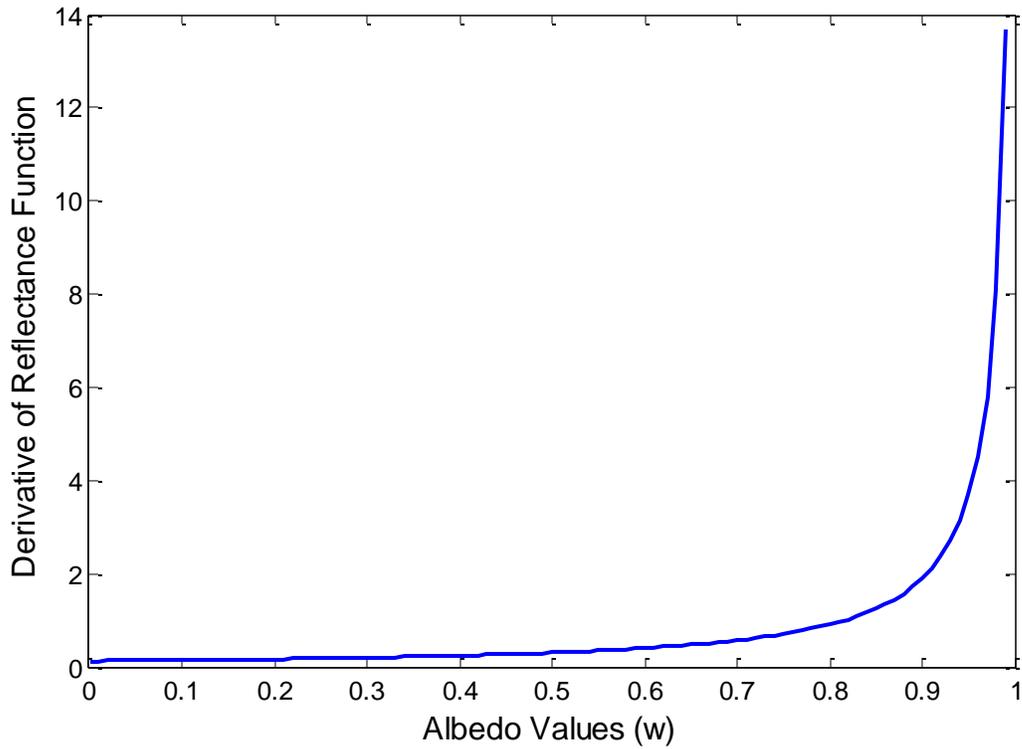


Figure 3-1. Derivative of reflectance function over range of albedo values.

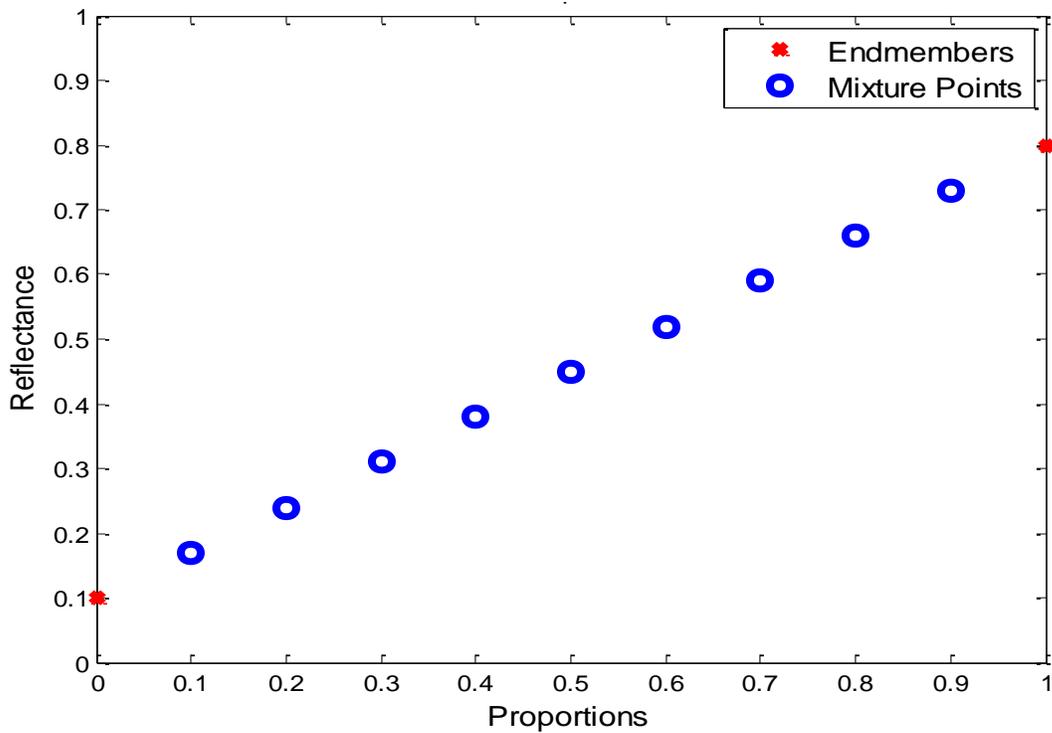


Figure 3-2. Macroscopic mixture points formed from uniform proportions of two endmembers, band one is plotted.

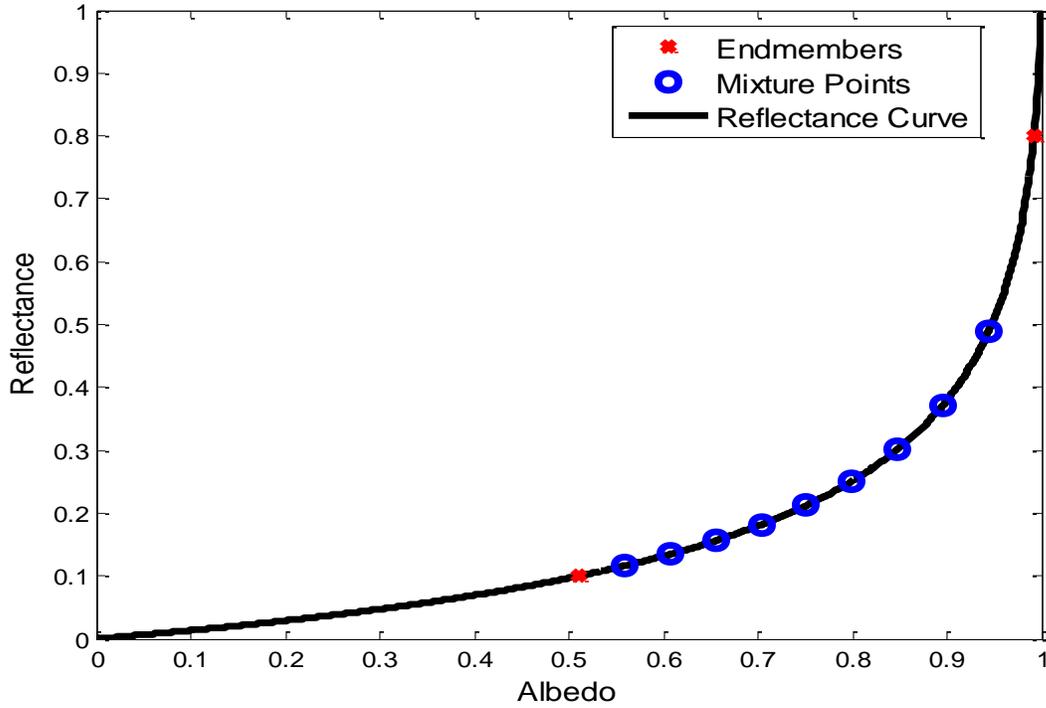


Figure 3-3. Reflectance curve with microscopic mixture points formed from uniform proportions of two endmembers, band 1 is plotted.

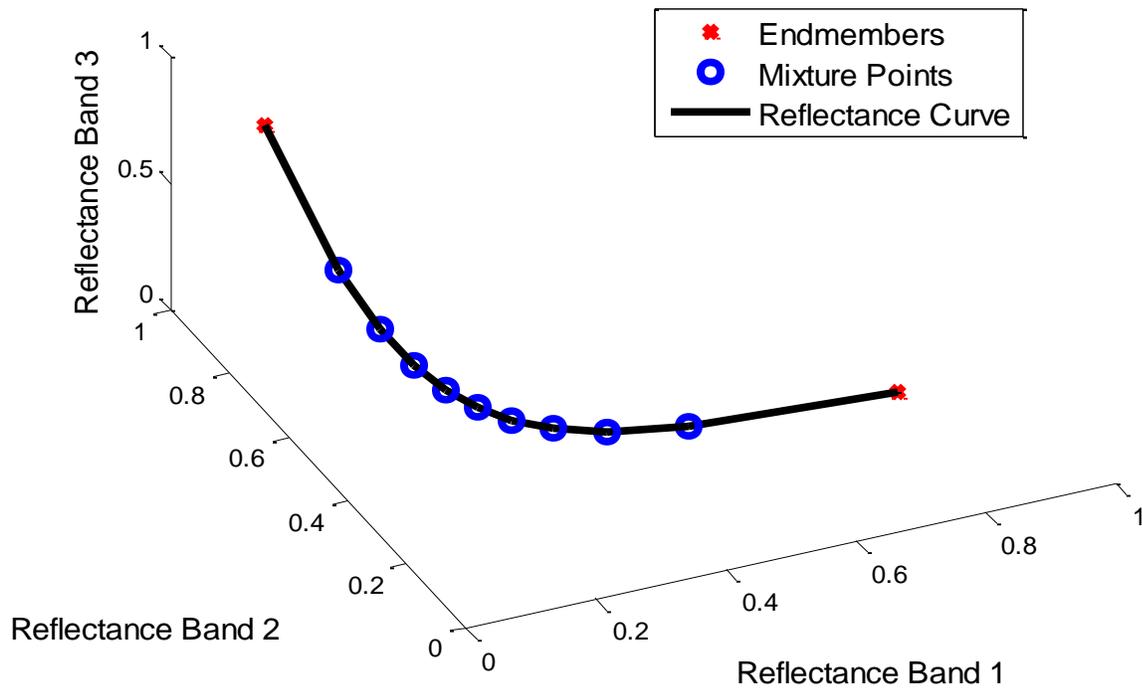


Figure 3-4. Three dimensional plot of microscopic mixture of two endmembers, all three bands are plotted.

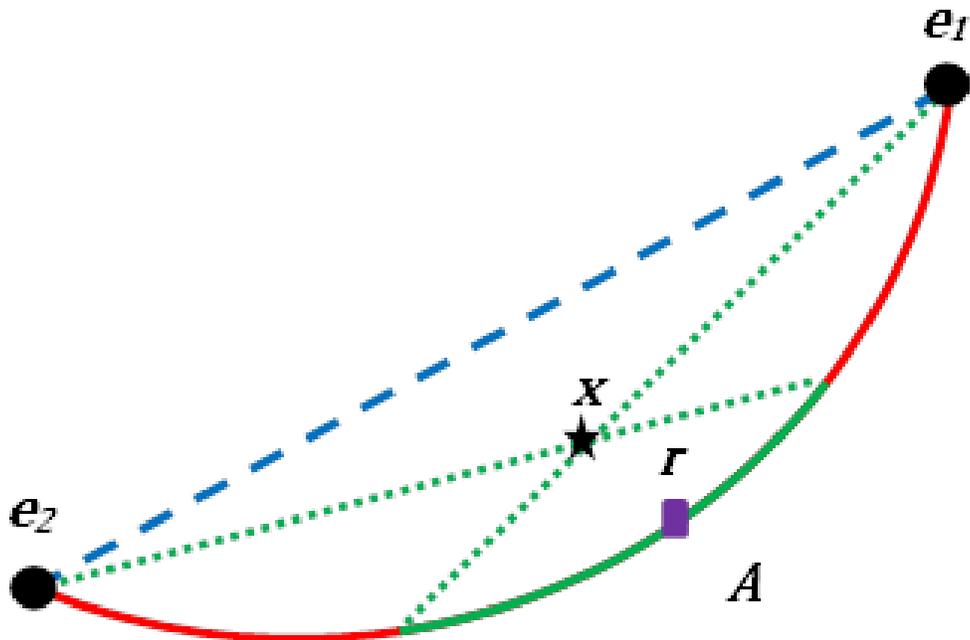


Figure 3-5. Diagram of multi-mixture pixel (black star) contained within the region bounded by the possible macroscopic mixtures (dashed blue line) and the possible microscopic mixtures (solid red line) with plausible constituent microscopic mixture (purple square).

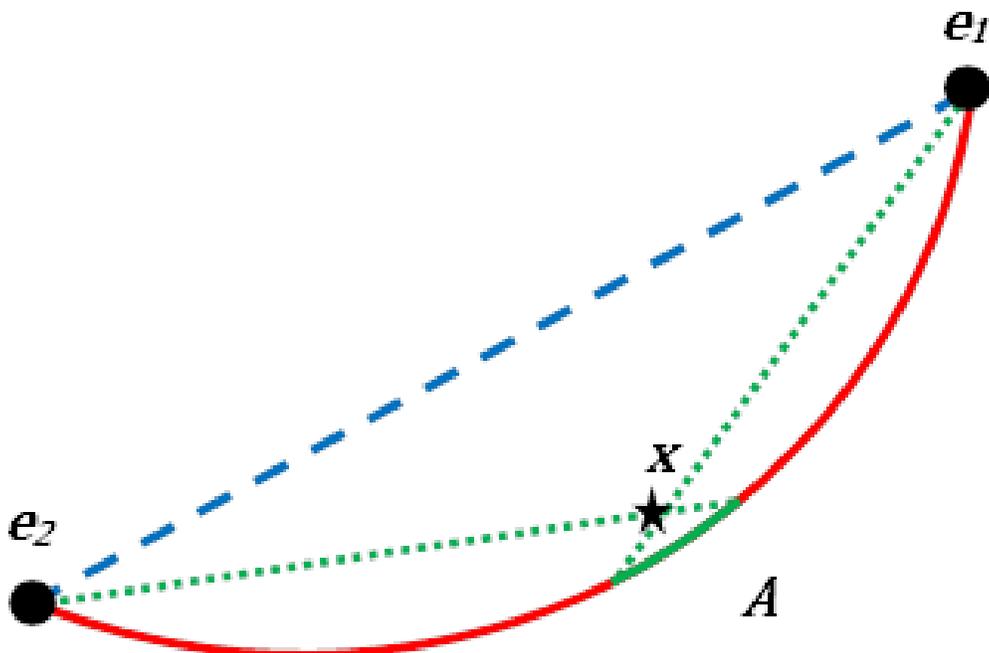


Figure 3-6. Diagram of multi-mixture pixel x contained within the region bounded by the possible macroscopic mixtures (dashed blue line) and the possible microscopic mixtures (solid red line) with plausible constituent microscopic mixtures (green arc).

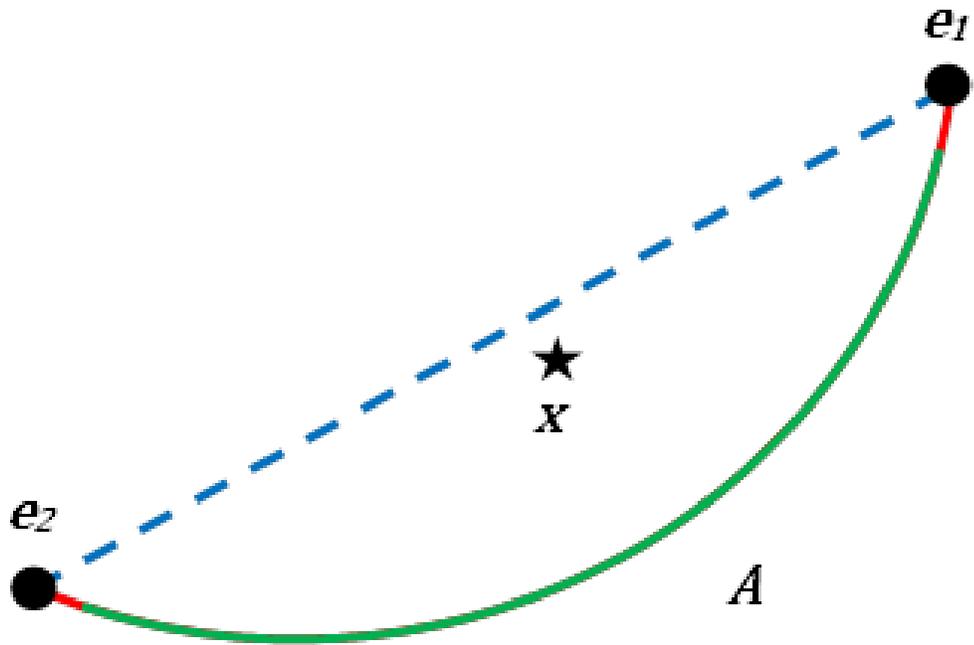


Figure 3-7. Diagram of multi-mixture pixel x contained within the region bounded by the possible macroscopic mixtures (dashed blue line) and the possible microscopic mixtures (solid red line) with plausible constituent microscopic mixtures (green arc).

CHAPTER 4

EXPERIMENTAL RESULTS

Experiments were conducted to assess the ability of the introduced algorithms to estimate proportions and endmembers in hyperspectral data. The algorithm's accuracies are functions of their underlying models and the means of estimating their parameters. Quantitative and qualitative analysis was used in evaluating the algorithms accuracy. The quantitative investigation of the proposed methods used a set of synthetically created data sets and the RELAB data of known mineral mixtures. The qualitative analysis was performed on two scenes from the MUUFL-Gulfport HSI collection.

Quantitative experiments allow for exact measurements of errors in estimating the proportions and endmembers with a given data set. These exact measurements are possible because each data set has known proportions and endmembers. Ability of the algorithms to estimate endmembers and proportions from airborne HSIs is assessed using qualitative analysis. Qualitative analysis is necessary due to the lack of exact measurements of endmembers and microscopic mixture proportions from airborne data collections.

The synthetic data sets were used to compare DME and MPE against LMM based algorithms. It was found that LMM-based algorithms caused increased error in estimating endmembers and proportions in data containing macroscopic and microscopic mixtures. DME demonstrated an ability to estimate endmembers, mixture types, and mixture proportions accurately in mixture data points dominated by discrete combinations of macroscopic and microscopic mixtures. MPE was found to have similar accuracy to DME but with improved accuracy when estimating endmembers and

proportions in multi-mixture data points. Using the RELAB data sets, DME and MPE were compared against existing models for estimating proportions in microscopically mixed data. These experiments indicate that DME and MPE both were able to estimate proportions of microscopic mixtures with more accuracy than existing algorithms.

Synthetic Data sets

The use of laboratory data sets is a very effective method for analyzing algorithms accuracies. However, due to the high cost in creating these data sets, they are composed of a small number of samples. Therefore a set of synthetic data sets was created to supplement the analysis of the laboratory experiments. The synthetic data sets allow for creation of a variety of conditions in which to test the algorithms ability to estimate proportions and endmembers.

Description of Data sets

The synthetic data sets are broken into five categories: macroscopic only, microscopic only, combined macroscopic and microscopic (CMM), multi-mixture pixel (MMP), and MMP with high microscopic proportion (MMP-HMP). Each data set contains 1,000 data points created using three 38 dimensional endmembers obtained from the ASTER spectral library, shown in Figure 4-1. [127] These endmembers represent the reflectance signatures of red smooth-faced brick, asphalt roofing shingle, and white marble; however, they are referred to in this document simply as endmember 1, 2, and 3, respectively. Because these endmembers are reflectance signatures, each band of the endmembers has a range from zero to one. The macroscopic and microscopic mixture data sets were created using the LMM of Equation 3-1 and the RD-MMM of Equation 3-9, respectively. Detailed descriptions of the LMM and the RD-MMM are given in Chapter 3. Independent zero-mean Gaussian noise, with standard

deviation of .001, was added to each mixture data point. The proportions for each model were drawn from a uniform distribution.

The CMM data set was formed from the union of 500 independently created mixture data points of each of the macroscopic and microscopic mixtures. The CMM data set can be viewed from the perspective of its first three principal components in Figure 4-2 and Figure 4-3. The blue x's in each of these figures represent the macroscopic mixture data points and therefore can also be used to illustrate the macroscopic mixture only data set. Similarly, the red o's in the figures are microscopic mixture data points and can be used to visualize the microscopic only data set.

The MMP and MMP-HMP were created using the multi-mixture pixel model of Equation 3-21. The macroscopic and microscopic mixture proportions for the MMP data set were sampled from a uniform distribution. Therefore, the MMP data set proportions between the three endmembers and the microscopic mixture are ~25%. The proportions for the MMP-HMP data set were sampled from a Dirichlet distribution in which the microscopic proportion was more likely. Therefore, the MMP-HMP data set is representative of a multi-mixture pixel in an environment dominated by microscopic mixtures, i.e., the microscopic proportion is ~92%. These two data sets will allow for analysis of the algorithms under contrasting microscopic mixing proportions of multi-mixed pixels. The MMP data set can be seen in Figure 4-4 and Figure 4-5.

Endmember Estimation

The synthetic data sets were used to assess the accuracy of DME and MPE in comparison to endmember estimation methods based on the LMM. These experiments were conducted using all five synthetic data set categories. The DME and MPE algorithms results were contrasted with the ICE and VCA algorithms. ICE and VCA

constitute representative endmember estimation methods from both the statistical and geometrical families of HSI endmember estimation methods.

Additionally, results are compared to the regularized linear mixture model gradient descent (RLMM-GD) algorithm and the albedo-domain RLMM-GD (AD-RLMM-GD) algorithm. RLMM-GD is similar to ICE with the exception that it uses a gradient descent approach to estimate endmembers within the ICE objective function. Details of the ICE algorithm can be found in Chapter 2. The AD-RLMM-GD algorithm converts all input reflectance-domain data into albedo-domain using the inverse of the reflectance function from Equation 3-3. Using the albedo-domain data, the RLMM-GD algorithm is run to estimate endmembers and proportions. Using RLMM-GD and AD-RLMM-GD allowed for comparison with LMM based algorithms that used gradient descent to estimate endmembers in both reflectance and albedo domains. Comparing DME and MPE against RLMM-GD and AD-RLMM-GD will negate any advantages that may be gained from using a gradient descent optimization.

To quantify the error between estimated and true endmembers, the mean absolute band error (MABE) is introduced. The MABE, shown in Equation 4-1, quantifies the error in each of the D dimensions between the true endmember (e_{dk}) and the estimated endmember (\hat{e}_{dk}). Similar to an L-1 norm, the MABE provides for a robust evaluation of the error over a set of M estimated endmembers.

$$MABE = \frac{1}{N \cdot D} \sum_{d=1}^D \sum_{k=1}^M |e_{dk} - \hat{e}_{dk}| \quad (4-1)$$

This section uses the synthetic data sets to investigate:

1. Initialization of parameters for DME and MPE

2. The failures, caused by microscopic mixing, of existing endmember estimation methods based on the LMM
3. The accuracy of DME and MPE in comparison to endmember estimation methods based solely on the LMM

Initialization and parameter robustness

As with many endmember estimation algorithms, ICE, RLMM-GD, AD-RLMM-GD, DME, and MPE require initialization and parameter settings. [3] Following the ICE framework, RLMM-GD, AD-RLMM-GD, DME, and MPE use an alternating optimization scheme to estimate the endmembers and proportions. [3] A convergence criterion is used in the algorithms, such that when the regularized RSS (Equation 3-16) error is reduced by less than 1×10^{-7} the algorithms terminate.

Gradient descent optimization is used to estimate the endmembers in the RLMM-GD, AD-RLMM-GD, DME, and MPE algorithms. Specifically, in these experiments, all algorithms used Newton's method in batch mode for minimizing the regularized RSS objective function. An annealing learning rate was used to control the step size. The learning rate started at 10 and was divided by two until either a step was found that reduced the objective function or the updated learning rate was less than 1×10^{-7} . If no step was made that reduced the objective function then the algorithm was terminated. Figure 4-6 shows the demonstrated robustness to the annealing rate used. The results in Figure 4-6 were obtained using five CMM data sets

Regularization parameter settings. In the ICE, RLMM-GD, AD-RLMM-GD, DME, and MPE algorithms the μ parameter acts as a regularization parameter offsetting the RSS error term and the SSD term, as shown in Equation 3-16 and repeated here in Equation 4-2 for convenience. The SSD penalizes the objective function as the distances between endmembers gets larger. This constrains the endmembers to fit

tightly around the data. The larger the μ the more the objective function minimizes the distances between endmembers versus the RSS error.

$$RSS_{reg} = (1 - \mu) \frac{RSS}{N} + \mu SSD \quad (4-2)$$

To evaluate the algorithms robustness to the μ parameter the following experiments were conducted. Each algorithm was run on five CMM synthetic data sets. Using the CMM synthetic data sets for these experiments provided a mix of macroscopic and microscopic mixture data points to optimize over. The algorithms were initialized using PPI. [53] These experiments were repeated for nine different settings of the μ parameter, the results are shown in Figure 4-7. The μ setting creating the smallest mean MABE for each algorithm was used. Based on the results of this experiment, the values given in Table 4-1 are used in all experiments presented in this document.

Initialization of starting endmembers. ICE, RLMM-GD, AD-RLMM-GD, DME, and MPE all use an alternating optimization scheme to iteratively estimate proportions and endmembers. Further, RLMM-GD, AD-RLMM-GD, DME, and MPE use a gradient descent optimization to estimate endmembers. One inherent problem with alternating optimization and gradient descent techniques is local minima. Consequently, initialization of starting endmembers has a large impact on the accuracy of the final estimated endmembers.

Choosing random input data points as starting endmembers is often the simplest solution. However, this approach, in all five algorithms, leads to large inconsistencies in estimating endmembers from a single data set, as demonstrated by Figure 4-8 – Figure 4-12. The histograms are the result of running each algorithm on a single CMM data

set 50 times. Each algorithm run used three randomly chosen data points as starting endmembers. Comparison of these histograms to the results obtained using PPI (Figure 4-7) reveals that using random data points as starting endmembers decreases the accuracy in endmember estimation for all considered algorithms.

As shown in Figure 4-7, PPI works well for initializing these algorithms even when including microscopic mixtures. PPI finds points near the vertices and returns spectra from actual data points. These spectra, when microscopically mixed, more accurately reflect the microscopic mixture created by the actual endmembers (i.e., no ambiguous errors are introduced to the spectra through trying to linearly estimate the endmembers). PPI is used to initialize all experiments presented in this document.

A common problem in endmember estimation is determining the number of endmembers in a mixture. [3, 4, 49, 71, 72] Using an incorrect number of endmembers will result in anomalous or missing endmembers from a mixture which in turn can cause incorrect proportion estimates for the estimated endmembers. In this research the correct number of endmembers will be provided as an input parameter, as has been done in other microscopic mixture research. [23, 24, 32, 35, 38] Future work, however, can use the SPICE framework to allow DME and MPE to automatically determine the number of endmembers. [4]

Microscopic mixture effects

To clarify analysis of experimental results, it is advantageous to categorize the types of effects that microscopic mixtures create. These effects are discussed with respect to the errors they cause by assuming a LMM. A macroscopic mixture of M endmembers is known to form a linear $M-1$ simplex embedded in D dimensions. [52] Assuming a three endmember mixture, the first and second principal components,

therefore, fully describe the linear simplex (ignoring noise). A microscopic mixture of the same endmembers warps the linear simplex, as discussed in Chapter 3. Using the synthetic data sets, three different effects can be observed due to this warping. These effects, and their magnitudes, are directly related to the single-scattering albedos and multi-scattering properties of the mixing endmembers, and collection parameters such as the angles of incidence and emergence.

Convex combination error. The first error will be referred to as a convex combination error (these names are not a recognized convention but used in this document for convenience). This error is defined by mixture data points that form a convex set in the linear span of the $M-1$ principal components but are not constrained to be convex combinations of the mixture endmembers. This violates the convex combination assumptions made in the LMM. [3]

The convex combination error can be observed in Figure 4-2. This figure shows the first and second principal components of a representative CMM mixture with three endmembers. The macroscopic mixture data points (blue x's) between endmembers one and three form a line of randomly distributed points resulting from the convex combination of endmembers. The microscopic mixture data points (red o's), between the same two endmembers, curve outside of the linear simplex formed by the endmembers. These mixture data points form a convex set but violate the convex combination constraints. Because this error occurs in the linear span of the $M-1$ principal components, geometrical methods will be directly impacted as well.

In these synthetic data sets, this type of error caused distortions in the estimated endmember spectra, i.e., increased or decreased reflectance in a subset of the

endmember's bands. Convex combination error is shown demonstrated on a CMM data set in Figure 4-13 and Figure 4-15. The image in Figure 4-13 shows the microscopic mixture data points curving outside of the simplex boundary between endmembers three and one. Optimization of the objective function based on the LMM caused the endmember estimates to spread out, attempting to create a linear simplex that enclosed all of the mixture data points. This error, observed in the $M-1$ principal axis of variation, causes the errors in estimated endmember spectra shown in Figure 4-15. In this example all three endmembers show a skewing of spectra in a subset of their bands.

Convex set error. The second type of error will be referred to as convex set error. This error is defined by mixture data points, created by microscopic mixing, that form a non-convex set. This violates the LMM assumption that mixture data points form a convex set. Additionally, this type of effect increases the intrinsic dimensionality of the mixture from $M-1$ dimensions to at least M dimensions.

Convex set error can be observed in the first and third principal components of the CMM data set shown in Figure 4-3. It is observed that the microscopic mixture data points form a non-convex set. Comparatively this error represented a small variation in the overall mixture. In the synthetic data sets discussed in this document, the additional principal component accounts for less than 1% of the total variance in a given data set.

Convex set error can be seen in the endmember estimation results shown in Figure 4-14. This figure shows the first and third principal components of the data, true endmembers, and estimated endmembers resulting from the same experiment shown in

Figure 4-13. The estimated endmembers minimize linear error between all mixture data points by averaging over the 3rd principal component.

Linear proportions error. The first two types of errors described perturbations, caused by microscopic mixing, of the linear simplex. The third type of error, linear proportions error, is defined as mixture data points in which the endmember proportions are not proportional to the relative distances between endmembers. In reflectance spectroscopy literature, this is termed the spectral dominance of low albedo materials in microscopic mixing. [32]

This error can be observed in Figure 4-2 and Figure 4-3 by noting that the macroscopic and microscopic proportions were drawn from the same uniform distribution. The macroscopic mixture points in the first, second, and third principal components appear uniformly distributed. However, the microscopic mixture points have the highest density near the endmember with the lowest albedo, and consequently lowest reflectance, endmember one. The microscopic mixture points are very sparse closer to endmember three, which has the highest albedo/reflectance.

Linear proportions error was characterized in these data sets by a uniform shift in the amplitude of the estimated endmember spectra. This error can be seen in the first three principal components, shown in Figure 4-16 and Figure 4-17. These figures show the results of the same experiment as shown in Figure 4-13 and Figure 4-14 except that in this experiment a μ of 1×10^{-3} was used. The images in Figure 4-16 and Figure 4-17 show that the endmember three estimation was pulled in closer to the largest density of mixture data points, when compared to Figure 4-13 and Figure 4-14. Figure 4-18

shows the effect of this error on the estimated endmember spectra. When compared to Figure 4-15, a uniform reduction in magnitude of endmember three can be observed.

The chart in Figure 4-7 shows increased MABE for the larger μ parameters, this increased error is largely caused by linear proportions error. Figure 4-19 shows the estimated endmembers from the same data set as the experiments in Figure 4-13 – Figure 4-18, using μ values 1×10^{-2} through 1×10^{-5} . These spectra demonstrate the increased error in estimation of endmember three caused by linear proportions error for larger μ values, and the contrasting increases and decreases in convex combination error.

Through an understanding of the causes of microscopic mixing, it is clear that microscopic mixtures are present in most HSIs. [1, 7, 30, 31] However, throughout published literature it is rare to find instances where these specific errors are addressed. This can be explained in some HSIs due to low proportion of microscopic mixing or small contrast between microscopically mixed endmembers. Both of these reduce the magnitude of error created by the microscopic mixture. Additionally, in many cases adequate ground-truth is not available to assess the accuracy of estimated endmembers from HSIs. However, recently the impact of nonlinear mixtures in HSIs has garnered much attention. [1, 8-19, 28, 33, 35-38, 41, 42, 44, 59, 60, 69, 95-98, 101, 104, 105, 116, 117, 119, 122] This, therefore, necessitates that these nonlinear microscopic mixing effects be used to increase endmember estimation accuracy and not simply dismissed.

Endmember estimation accuracy

In this section, results are presented to assess the accuracy of DME and MPE in estimating endmembers. For comparison, the results of DME and MPE will be contrasted to the results of VCA, ICE, RLMM-GD, and AD-RLMM-GD. To compare the algorithms, 50 synthetic data sets of each category were generated. Each of the six algorithms was run on the data sets and the resulting MABE values calculated. The algorithms were initialized using the same starting initial endmembers, determined by using PPI, and the μ parameter values given in Table 4-1. The mean MABE values for each data set are given in Figure 4-20 – Figure 4-22. For ease of readability, the results were broken into three separate charts. The first chart (Figure 4-20), illustrates the results for VCA, a representative geometric method based on the LMM. The second chart (Figure 4-21), shows the results for ICE and RLMM-GD, two representative statistical methods based on the LMM. Finally, the third chart (Figure 4-22) gives the results for AD-RLMM-GD, an albedo-domain method based on the LMM.

The error bars in each chart represent one standard deviation from the mean MABE over a given data set category. The distribution of MABE values for a given algorithm and data set, however, are not Gaussian distributions. The histograms for each algorithm run on the CMM data sets is given in Figure 4-23 – Figure 4-28. Further analysis treats the MABE values resulting from any two algorithms on the same data set as a paired test. The charts in Figure 4-29 – Figure 4-32 illustrate the difference in MABE values between the LMM based algorithms and DME and MPE.

From these results it can be observed that when macroscopic mixtures dominated the data set (i.e., macroscopic only and MMP), the reflectance-domain LMM algorithms performed similar to DME and MPE. These observations are contrasted with the poor

performance of the reflectance-domain LMM algorithms (VCA, ICE, RLLM-GD) on data sets dominated by microscopic mixtures (i.e., microscopic only and MMP-HMP).

Likewise, the albedo-domain LMM algorithm (AD-RLMM-GD) performed similar to DME and MPE on those data sets dominated by microscopic mixtures and poorly on those dominated by macroscopic mixtures. The CMM data sets combine equal numbers of macroscopic and microscopic mixture data samples, therefore, they provide a single data set to evaluate the results of these algorithms on both mixture types. The paired MABE difference histograms of the LMM algorithms and DME and MPE are given Figure 4-33 – Figure 4-36.

The charts in Figure 4-29 – Figure 4-32 also indicate that DME did not consistently perform better than the LMM algorithms on the MMP-HMP data sets. This results from the multi-mixture pixel model that formed these data sets. The histogram in Figure 4-37 illustrates the paired MABE difference between MPE and all other algorithms, including DME. These results demonstrate that MPE consistently created lower MABE than the other algorithms when estimating endmembers of a multi-mixture pixel.

Proportion Estimation

In this section the accuracy of DME and MPE in estimating endmember proportions is assessed. To compare with experiments performed in other published research, each algorithm being evaluated took as input the correct endmember spectra for each data set. [23, 24, 32, 35, 37] Each algorithm estimated proportions of the mixture data, using their respective approaches, and reported error in proportion estimation using the root mean square error (RMSE). The RMSE, shown in Equation 4-3, is commonly used to measure proportion estimation accuracy, where N is the number of data set samples, M is the number of endmembers, a_{ik} is the true proportion

of the sample, and \hat{a}_{ik} is the estimated proportion. [23, 24, 32, 35, 37] The sample proportion estimates are calculated for DME using Equation 4-4 and for MPE with Equation 4-5, where \hat{p}_{ik} and \hat{f}_{ik} are the estimated macroscopic and microscopic proportions for the models, respectively.

$$RMSE = \left(\frac{1}{N \cdot M} \sum_{i=1}^N \sum_{k=1}^M (a_{ik} - \hat{a}_{ik})^2 \right)^{\frac{1}{2}} \quad (4-3)$$

$$\hat{a}_{ik} = t_{i1}(\hat{p}_{ik}) + t_{i2}(\hat{f}_{ik}) \quad (4-4)$$

$$\hat{a}_{ik} = \hat{p}_{ik} + p_{iM+1}(\hat{f}_{ik}) \quad (4-5)$$

In these experiments 50 data sets were generated from each synthetic data set category. DME and MPE were run on all data sets and their mean RMSE of proportions estimates calculated. When using the given true endmembers the standard deviation of proportion estimates was less than .01 in all cases. Therefore, the error bars were not used in the results charts. To evaluate DME and MPE, the LMM and the albedo-domain (AD-LMM) were included for comparisons. The LMM and AD-LMM use quadratic programming to estimate the endmember proportions of the given data points. This method of linear unmixing is commonly used in published literature, including the ICE algorithm. [3] The AD-LMM, however, first converts the endmembers and mixture data points into the albedo-domain using the inverse of the reflectance function from Equation 3-3. In the following sections the effects of microscopic mixtures on proportion estimation is discussed, as well as an analysis of the accuracy of DME and MPE for estimating microscopic mixture concentrations and estimating mixture proportions.

Microscopic mixture effects

Microscopic mixtures affect linear proportion estimation in two ways. The first is caused by the previously mentioned convex combination and convex set errors. These errors were visualized in Figure 4-2 and Figure 4-3. As both figures show, microscopic mixtures create a warped simplex. When unmixing hyperspectral data, using a linear model, it is assumed (by definition of the linear model) that all data points are contained within the linear simplex described by the endmembers. [1] Therefore, when estimating the proportions of a microscopic mixture data point using a linear model, the data point is actually the projection of the microscopic mixture point onto the linear simplex. This projection does not preserve the true relationship between endmembers represented by the data point and thus error is introduced. [1]

Secondly, the previously discussed linear proportions error causes inaccuracies in estimating proportions when using a linear model. The spectral dominance of low albedo substances causes a non-uniform distribution of mixture points. [32] The linear model makes the assumption that a data point is a linear combination of its constituent endmembers, i.e., the proportions of each endmember are equivalent to the relative distance between the mixture point and the vertices of the linear simplex. As shown in Figure 4-38, a microscopic mixture of 50% of each of two endmembers in the albedo-domain (shown as the cyan dashed line) is a linear mixture. However, when converted to reflectance-domain, the signature of the mixture point (cyan dotted line) does not represent a linear 50% mixture of each endmember (red dotted line).

Estimating microscopic mixture concentration

In estimating endmember proportions of a mixed data set, some knowledge about the mixture types present in the data must be either assumed or estimated. In the case

of the LMM the mixture type is assumed to be 100% macroscopically mixed. Likewise, in the AD-LMM the mixture type is assumed to be 100% microscopically mixed.

Broadwater was the first to present an algorithm that was able to identify a mixture data point, or pixel, as macroscopically or microscopically mixed. [24, 25] In his paper, the mixture identified for each pixel was used to characterize the mixing patterns in the given HSI. This information provides a unique analysis and understanding of the HSI. These labels can also be used as a diagnostic tool to better understand the mixtures present in a mixed data point and evaluate the accuracy of the estimation algorithm.

DME presents a similar capability to Broadwater's kernel method. MPE, however, builds upon this capability by using the MMP model. MPE is able to estimate the proportion of microscopic mixing occurring in a single mixed data point. This allows new observations and analysis of the disbursement patterns of various substances throughout a scene. DME discriminates each sample as wholly macroscopically or microscopically mixed. Therefore, DME estimates microscopic mixture proportions for a given data set as the percentage of mixture data points labeled as microscopically mixed. MPE estimates samples as partially microscopically mixed; therefore the microscopic proportion estimate of a data set is the mean microscopic proportion over every sample in the data set.

The results of the mean estimated microscopic proportions are shown in Figure 4-39. LMM and AD-LMM are unable to estimate mixture types. Therefore, as indicated by the graph, produce large errors in estimating mixture types when compared to the known mixture type proportions. DME and MPE were able to accurately estimate the proportion of mixture data points representing microscopic mixtures in the macroscopic,

microscopic, and CMM data sets. DME's microscopic proportion estimation for the MMP-HMP data set, which is dominated by microscopic mixtures, is accurate. However, DME's discrete mixture assumption fails as is indicated by the large error in estimating the microscopic proportion in the MMP data sets. MPE proportion estimation shows an error of approximately 6.0% – 8.0% estimated microscopic proportion between the MMP and MMP-HMP data sets. This error is due to the ill-posed inversion problem of estimating the microscopic proportions.

Proportion estimation accuracy

Using the results of the same experiments run for the mixture type concentration, the accuracy in proportion estimation is assessed. The results of the proportion estimation experiments are shown in Figure 4-40. This chart shows the RMSE for each of the LMM, AD-LMM, DME, and MPE proportion estimation algorithms for each randomly generated data set. These results indicate large RMSE in proportion estimations for LMM and AD-LMM when the data set dominate mixture type is not in-line with the mixture type assumption made by the algorithm. Both DME and MPE demonstrate an ability to accurately estimate endmember proportions in the macroscopic, CMM, and microscopic data sets. DME and MPE indicate increased errors in estimation in the MMP and MMP-HMP data sets. The increased error in estimating proportions of these data sets is understood in DME as a failed assumption of discrete mixtures. MPE, however, indicates more accuracy in estimating proportions in the MMP and MMP-HMP data sets with some error in estimation, as previously discussed.

Based on these results, the following conclusions can be made. Microscopic mixtures can cause nonlinear effects that violate the LMM's assumptions. These

violations cause increased error in estimating endmembers and their proportions when microscopic mixing is present. DME and MPE are able to accurately estimate endmembers and their proportions when macroscopic and/or microscopic mixtures are present. Additionally, when a mixture data point is composed of a multi-mixture pixel the DME can show increased errors in estimating endmembers and proportions. However, MPE is able to estimate these endmembers and proportions with decreased error.

RELAB Data sets

Description of Data Sets

Quantitative analysis of DME and MPE was performed on mixtures of Olivine with Enstatite and Olivine with Magnetite. The mixtures were prepared and measured by Professors John Mustard and Carle Pieters of Brown University, as specified in their paper. [32] The spectra were collected with RELAB, a high-resolution bidirectional reflectance spectrometer with a specified angle of emergence of 0° and angle of incidence of 30° . [32] Each mixture data set is composed of spectra from five mixed samples (proportions of which are given in Table 4-2) and two endmembers, as shown in Figure 4-41 and Figure 4-42. The spectra have 211 dimensions with wavelengths ranging from 400 nm to 2,500 nm.

The precise measurements of the mineral mixture proportions and their spectra make these data sets ideal for analysis of hyperspectral unmixing algorithms. These mineral sets are known to mix microscopically and each sample was crushed prior to mixing, to ensure a homogenous mixture. A scatter plot of two wavelengths of the Olivine with Magnetite data set (Figure 4-43) demonstrates the nonlinearity in the mixtures. Additionally, the endmembers have a variety of absorption features (including

the contamination feature in the Olivine spectra) and both small and large contrasts between endmember albedos. Consequently these samples have become a standard data set for evaluating microscopic unmixing algorithms. [23, 24, 32, 35, 37]

Endmember Estimation

Experiments were conducted to compare endmember estimation of DME and MPE against ICE using the RELAB data. All three algorithms used the μ parameters given in Table 4-1 (as previously determined) and sample points one and five as initial endmembers. The results of the experiments on the Magnetite and Olivine data set are shown in Figure 4-44 and the Enstatite and Olivine data set in Figure 4-45. The MABE for both experiments is given in Figure 4-46. These results indicate that in both experiments DME and MPE were able to estimate the endmembers with more accuracy than ICE. In the Magnetite and Olivine experiment, DME resulted in a lower MABE. In the Enstatite and Olivine experiment, MPE resulted in a lower MABE. As will be shown in the next section, this phenomenon is mimicked in the proportion estimation experiments.

Proportion Estimation

The RELAB Enstatite with Olivine and Magnetite with Olivine binary mixtures have become the *de facto* standard of comparison between microscopic proportion estimation algorithms. [23, 24, 32, 35, 37] Experiments with these data sets allow a precise comparison between DME and MPE and other attempts to estimate proportions with microscopic mixing. In addition, results from the LMM algorithm are included for comparisons.

The proportion estimation results are shown in Table 4-3, part A shows results from the Enstatite & Olivine mixture and part B the Magnetite & Olivine mixture.

Proportion RMSE results were included from or calculated from published results using the LSE[32], kernel methods[23-25], RBFNN[35], and HNN/MLP[37] algorithms. See Chapter 2 for details on these algorithms.

In the published works using kernel methods and neural networks to unmix microscopically mixed hyperspectral data, RMSE comparisons were made using the known mass fractions of the RELAB samples. [23, 24, 35, 37] However, since these unmixing algorithms estimate microscopic mixture proportions, often referred to as F-parameters, an assumption of similar particle densities and diameters between endmembers is required (details discussed in Chapter 2). [7, 30, 32] The RELAB data sets were prepared such that particle diameters are similar but not particle densities. [32] Therefore, a more appropriate measure of accuracy in estimating RELAB proportions is to calculate RMSE between estimated proportions and published F-parameters for the data sets.

Table 4-3 lists proportion RMSEs between published LSE, RBFNN, and HNN/MLP estimated proportions and F-parameter truth for comparison with the experimentally estimated DME and MPE proportions. [32, 35, 37] However, the estimated proportions using the various kernel methods were not available and the reference papers did not describe the experiments in enough detail to allow reproduction of the experiments. [23, 24] Therefore, the proportion RMSE using mass fractions is given, as published, for the kernel and neural network approaches. [23, 24, 35, 37] Additionally, Table 4-3 lists the percentage of the data set estimated by the algorithm as a microscopic mixture.

These results indicate that in the Magnetite and Olivine experiments DME estimated the proportions with the most accuracy, followed by LSE and MPE. Further

insight into this result can be drawn from the microscopic mixture estimate for both DME and MPE. DME estimated a 100% microscopic mixture. This indicates that the algorithm would unmix the data set similarly to the LSE algorithm, which leads to the similar results between those algorithms shown in Table 4-3. The microscopic mixture for MPE is 98.3%. Based on this estimation, it can be concluded that previously discussed error in estimating microscopic mixing proportions caused increased proportion estimation error. Therefore, MPE displayed more RMSE than DME and LSE.

The results for the Enstatite and Olivine data set show a contrasting example. In these results (Table 4-3), MPE produced the lowest RMSE followed by DME. The microscopic mixture estimation results indicate that both DME and MPE estimated this data set as having a large macroscopic mixing component. This is likely due to the small contrast between mixing endmembers. The ability of DME and MPE to include macroscopic mixing in their estimations allowed for large improvements in RMSE over the LSE algorithm. Of the algorithms evaluated, DME and MPE were the only ones able to estimate the mixture proportions accurately over both data sets.

Aerial Hyperspectral Data Sets

To assess the ability of DME and MPE to operate on aerial hyperspectral data, the MUUFL-Gulfport collection was used. The MUUFL-Gulfport data was collected with a CASI hyperspectral sensor over Gulfport, MS. The data provides 72 bands ranging from 368 nm to 1,043 nm with a spatial resolution of 1 m x 1 m. Qualitative analysis of the data using DME and MPE estimated proportions and endmembers indicated a plausible explanation of the HSI.

Baseball Diamond Scene

The first scene discussed is the baseball diamond scene, shown in Figure 4-47. The pixels used in this experiment were specifically selected so that just the baseball diamond was included, i.e., the baseplate and trees were excluded. The endmembers estimated by DME, MPE, and ICE are shown in Figure 4-48. All three methods estimated endmembers similar in spectral shape, which is a consequence of a large amount of macroscopic mixing over microscopic. The spectra indicate grass, dirt, and clay endmembers. The grass endmember can be identified by the bump observed at approximately 550 nm and the increased reflectance in the near infrared (IR). The clay endmember is characterized by relatively high reflectance from approximately 550 nm through the IR. The negative values present in the spectra are a result of errors in the conversion process of estimating pixel reflectance values from measured radiances. In this data set the conversion was performed using the empirical line method for atmospheric correction. The relative smoothness of the spectra also indicates that plausible endmember spectra were extracted.

DME detected microscopic mixture pixels (shown in red) can be observed in Figure 4-49. DME was able to find a few microscopically mixed pixels but a majority of the pixels in this scene were more than 50% macroscopically mixed.

MPE's microscopic mixture mapping is shown in Figure 4-50. To further understand these results the MPE macroscopic proportions map for the grass endmember is shown in Figure 4-51 and the microscopic proportion map in Figure 4-52. These maps indicate extensive macroscopic and microscopic mixing in the outfield and infield. These results make sense, especially when considering the macroscopic and

microscopic proportions of the dirt endmember, Figure 4-53 and Figure 4-54, respectively.

The dirt endmember shows slight macroscopic and microscopic mixing across the entire scene, except for an area between bases in the middle of the base path. The dirt endmember also shows increased macroscopic mixing in the area on the outside of the base path that is darker in the color image of the scene (Figure 4-47). A most likely explanation would be that dirt from the outfield has, over time, spread into the clay base path.

The proportion maps for the clay endmember are shown in Figure 4-55 for the macroscopic proportions and Figure 4-56 for the microscopic proportions. Both proportion maps illustrate a dominance of the clay endmember in the base path, mostly observed between first, second, and third base. However, a faint base path between home plate and first and home plate and third can be observed. Also, pixels containing clay endmember proportions can be seen in the middle of the infield, the pitcher's mound.

Beach Scene

The second scene looked at in these experiments was the beach scene, shown in Figure 4-57. In this experiment only pixels covering the beach were included. To estimate the endmembers VCA was used. [54] Two endmembers were found: a sand endmember and a sediment endmember. MPE was used to unmix the pixels given the VCA estimated endmembers. The microscopic mixture proportions map is shown in Figure 4-58. From this image it can be seen that the sediment is originating from the construction area to the left of the beach. The sediment is dispersed down the beach by wind and water.

The dispersion pattern of the sediment can be observed by referencing the sand macroscopic and microscopic proportion maps, Figure 4-59 and Figure 4-60, respectively, and the sediment macroscopic and microscopic proportion maps, Figure 4-61 and Figure 4-62, respectively. It can be observed from the microscopic proportion maps of each endmember that while sand is the dominant endmember, concentrations of the sediment are found near the origin point and in concentration points along the beach. Also, the microscopic proportion maps reveal that along the waterline traces of the sediment can be seen mixing microscopically with the sand. This leads to the conclusion that the sediment bled into the water and was deposited along the waterline of the beach. Using the macroscopic proportion maps areas of sediment can be observed to be macroscopically mixing along the fence line. This result can be explained by wind that blows the sediment and sand that is then trapped by the fence. Therefore, more concentrated areas of sediment are created thus causing macroscopic mixtures.

Due to a lack of precise mixture ground truth, an exact analysis of DME and MPE on the aerial HSI data is not possible. However, a plausible explanation was presented for each scene. Further, analysis of sediment distribution made possible by estimating microscopic mixture was presented.

Table 4-1. Algorithm μ parameter settings.

Algorithm	μ
ICE	1.0E-04
RLMM-GD	1.0E-04
AD-RLMM-GD	1.0E-07
DME	1.0E-07
MPE	1.0E-09

Table 4-2. RELAB data set true proportions.

Mass Fraction		F-Parameter		Mass Fraction		F-Parameter	
Olivine	Enstatite	Olivine	Enstatite	Olivine	Magnetite	Olivine	Magnetite
90	10	0.897	0.103	95	5	0.967	0.033
75	25	0.745	0.255	90	10	0.933	0.067
50	50	0.493	0.507	75	25	0.823	0.177
25	75	0.245	0.755	50	50	0.610	0.390
10	90	0.097	0.903	25	75	0.343	0.657

Table 4-3. Comparison of proportion estimates of RELAB mixtures using mass fraction and F-parameter values. A) Olivine & Enstatite mixture. B) Olivine & Magnetite mixture. [*Results adapted from J. F. Mustard and C. M. Pieters, "Quantitative Abundance Estimates From Bidirectional Reflectance Measurements," *Journal of Geophysical Research*, vol. 92, pp. E617-E626, March 30, 1987 1987. **Results adapted from J. Broadwater and A. Banerjee, "A comparison of kernel functions for intimate mixture models," in *Hyperspectral Image and Signal Processing: Evolution in Remote Sensing*, 2009. WHISPERS '09. First Workshop on, 2009, pp. 1-4. ***Results adapted from J. Broadwater and A. Banerjee, "A generalized kernel for areal and intimate mixtures," in *Hyperspectral Image and Signal Processing: Evolution in Remote Sensing (WHISPERS)*, 2010 2nd Workshop on, 2010, pp. 1-4. **** K. J. Guilfoyle, M. L. Althouse, and I. C. Chein, "A quantitative and comparative analysis of linear and nonlinear spectral mixture models using radial basis function neural networks," *Geoscience and Remote Sensing, IEEE Transactions on*, vol. 39, pp. 2314-2318, 2001. ***** J. Plaza, P. Martinez, R. Perez, and A. Plaza, "Nonlinear Neural Network Mixture Models for Fractional Abundance Estimation in AVIRIS Hyperspectral Images," presented at the NASA Jet Propulsion Laboratory AVIRIS Airborne Earth Science Workshop, Pasadena, California, 2004.]

A			
Method	F-Parameter Proportion RMSE	Mass Fraction Proportion RMSE	Microscopic Mixture
DME	0.0136		60.0%
MPE	0.0118		54.7%
LMM	0.0389	0.0348	N/A
*LSE	0.0267		N/A
**RBF Kernel		0.0345	N/A
**Polynomial Kernel		0.0158	N/A
**Physics-based Kernel		0.0228	N/A
***Areal/Intimate Kernel		0.0197	UNK
****RBFNN	0.0306	0.0337	N/A
*****HNN/MLP	0.0171	0.0168	N/A
B			
Method	F-Parameter Proportion RMSE	Mass Fraction Proportion RMSE	Microscopic Mixture
DME	0.0135		100.0%
MPE	0.0219		98.3%
LMM	0.2790	0.2100	N/A
*LSE	0.0193		N/A
**RBF Kernel		0.2101	N/A
**Polynomial Kernel		0.1658	N/A
**Physics-based Kernel		0.0561	N/A
***Areal/Intimate Kernel		0.0589	UNK
****RBFNN	0.0318	0.0490	N/A
*****HNN/MLP	0.0802	0.0754	N/A

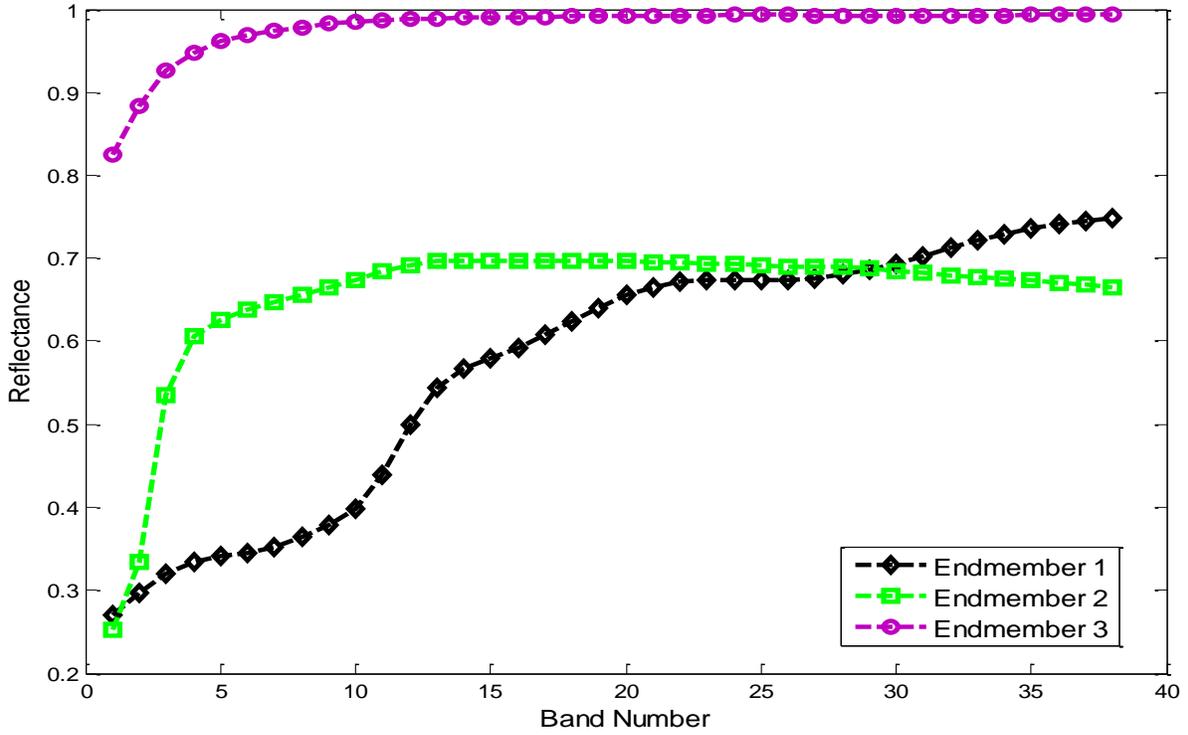


Figure 4-1. Synthetic endmember reflectance spectra.

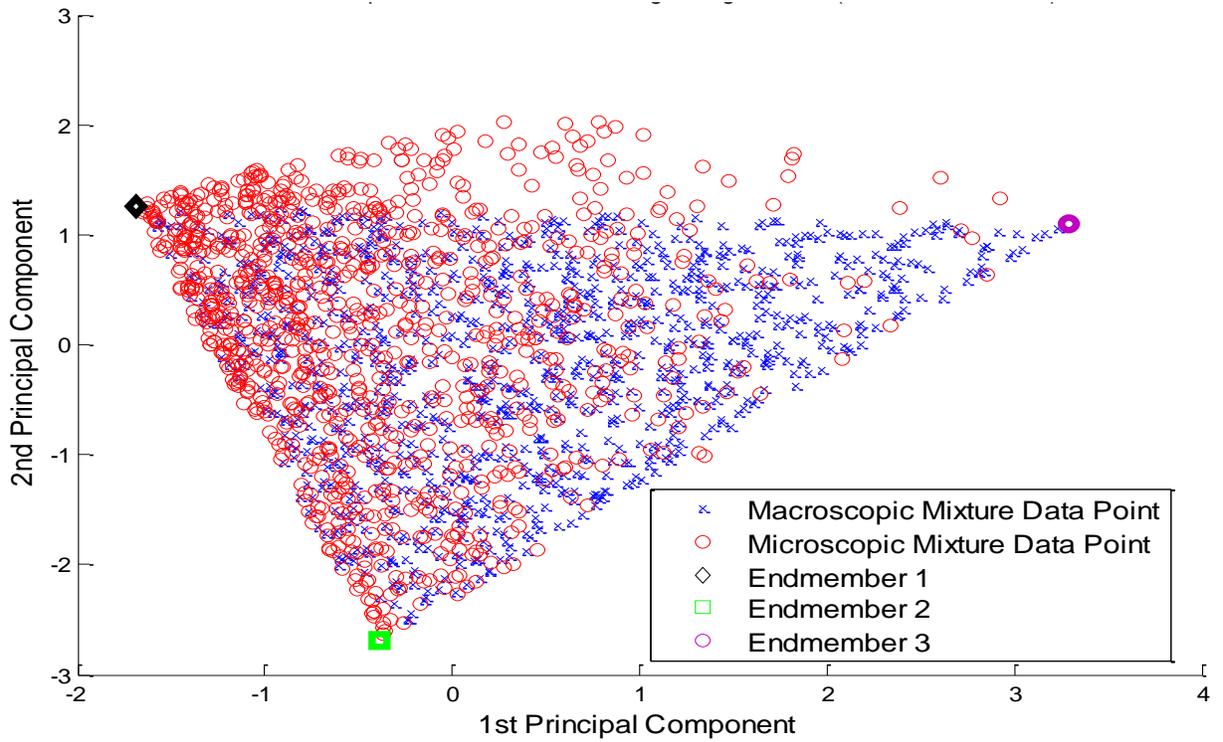


Figure 4-2. 1st and 2nd principal components of synthetic CMM data set.

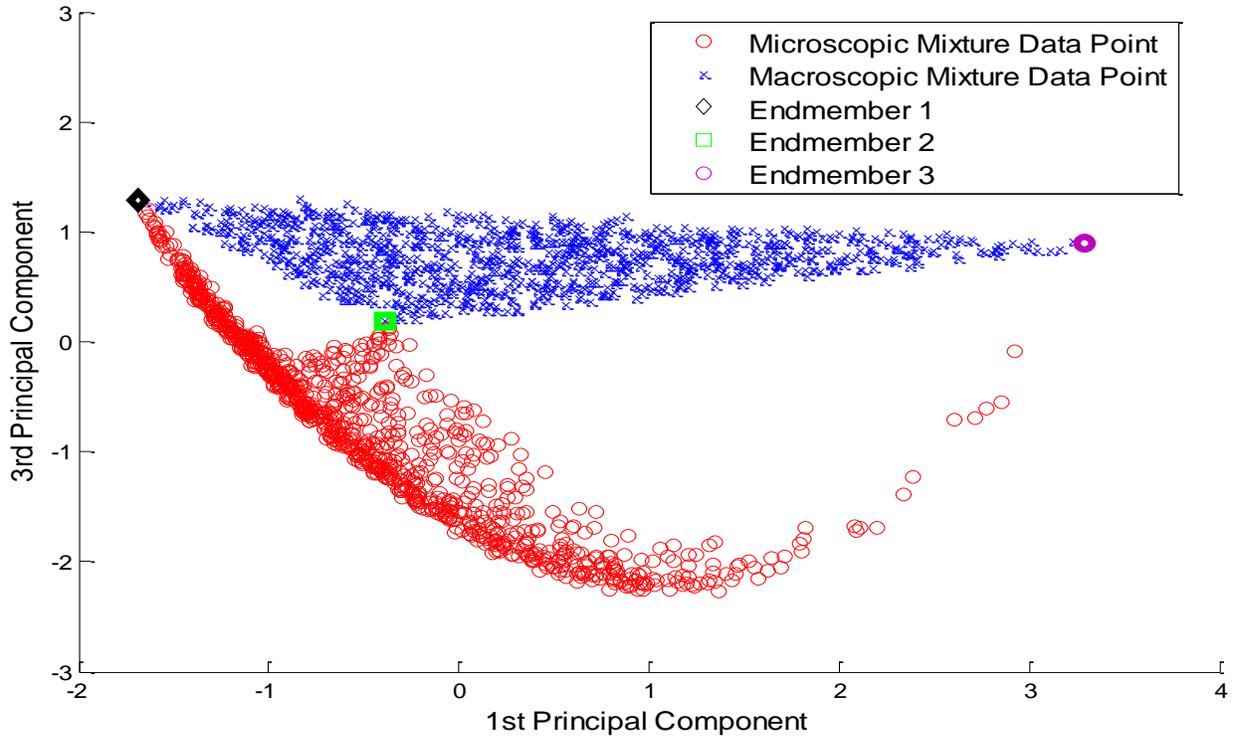


Figure 4-3. 1st and 3rd principal components of synthetic CMM data set.

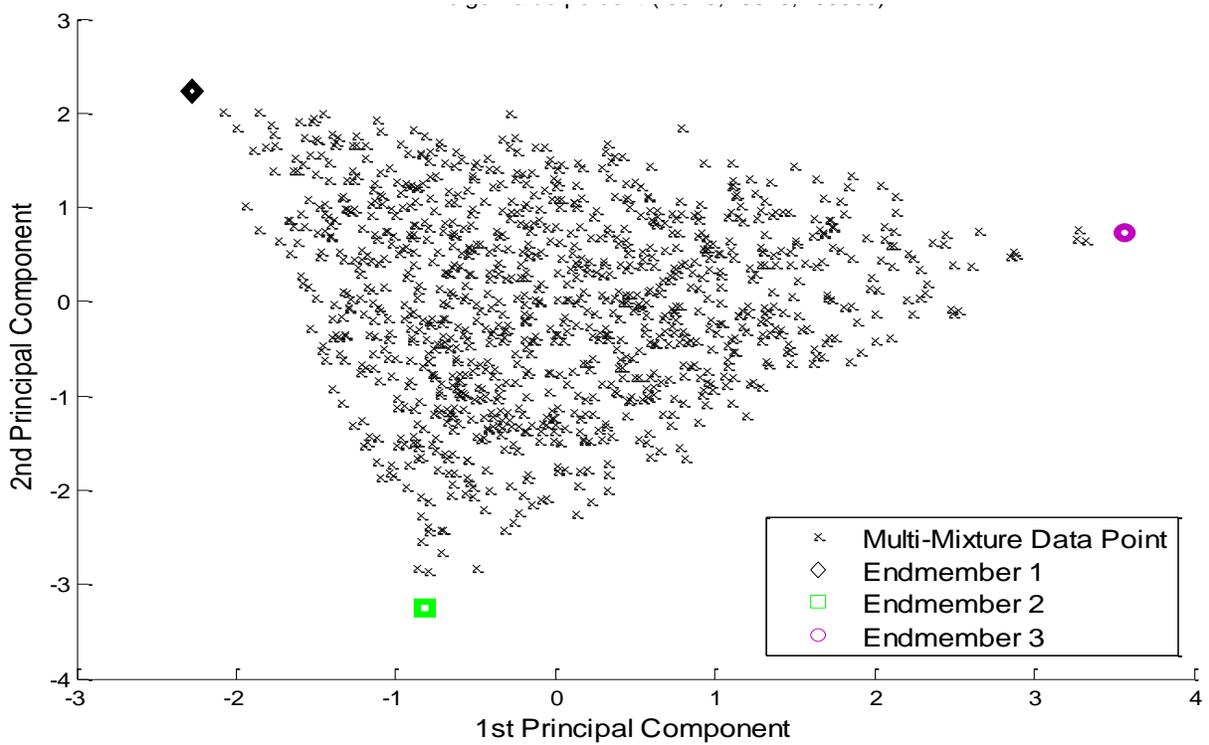


Figure 4-4. 1st and 2nd principal component of synthetic MMP data set.

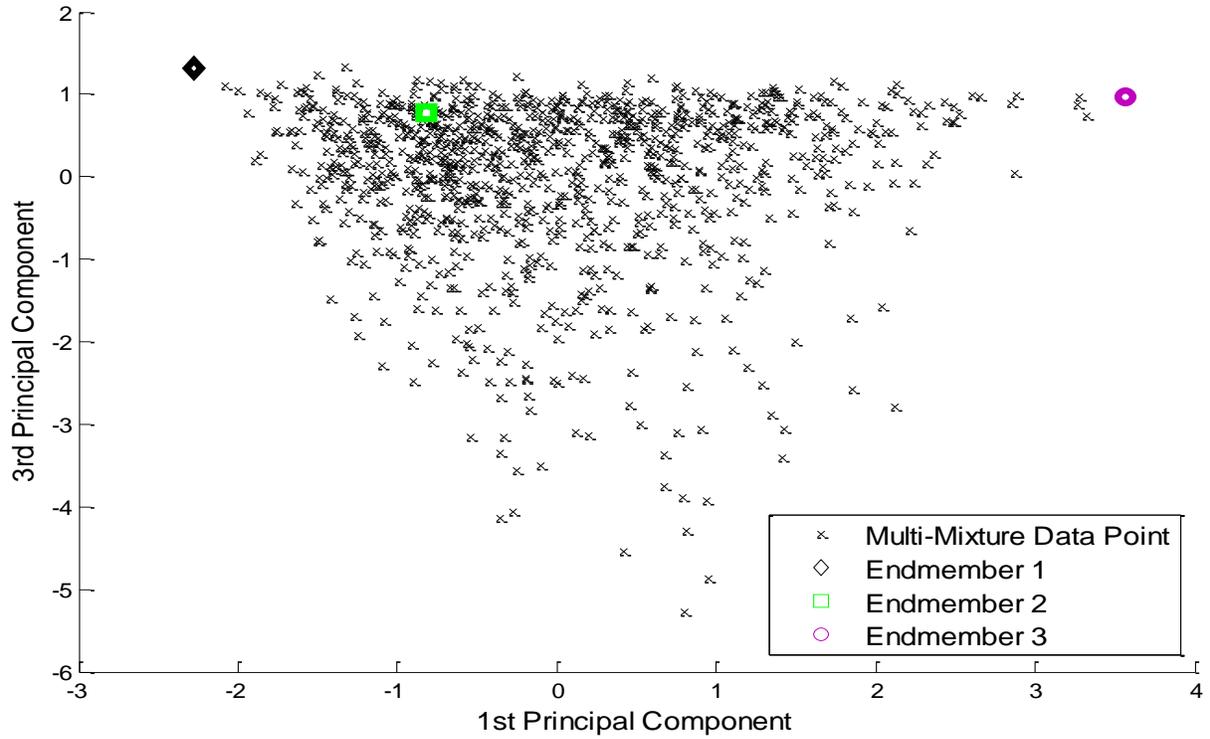


Figure 4-5. 1st and 3rd principal component of synthetic MMP data set.

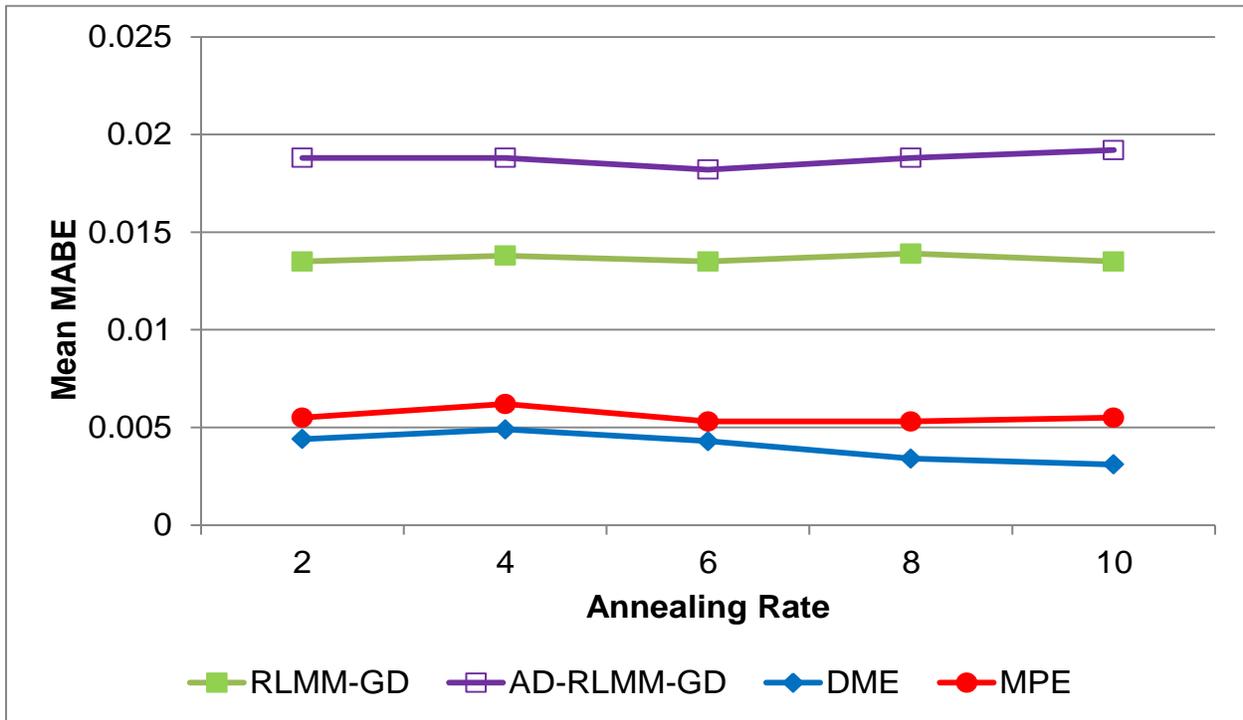


Figure 4-6. Mean MABE over range of annealing rates.

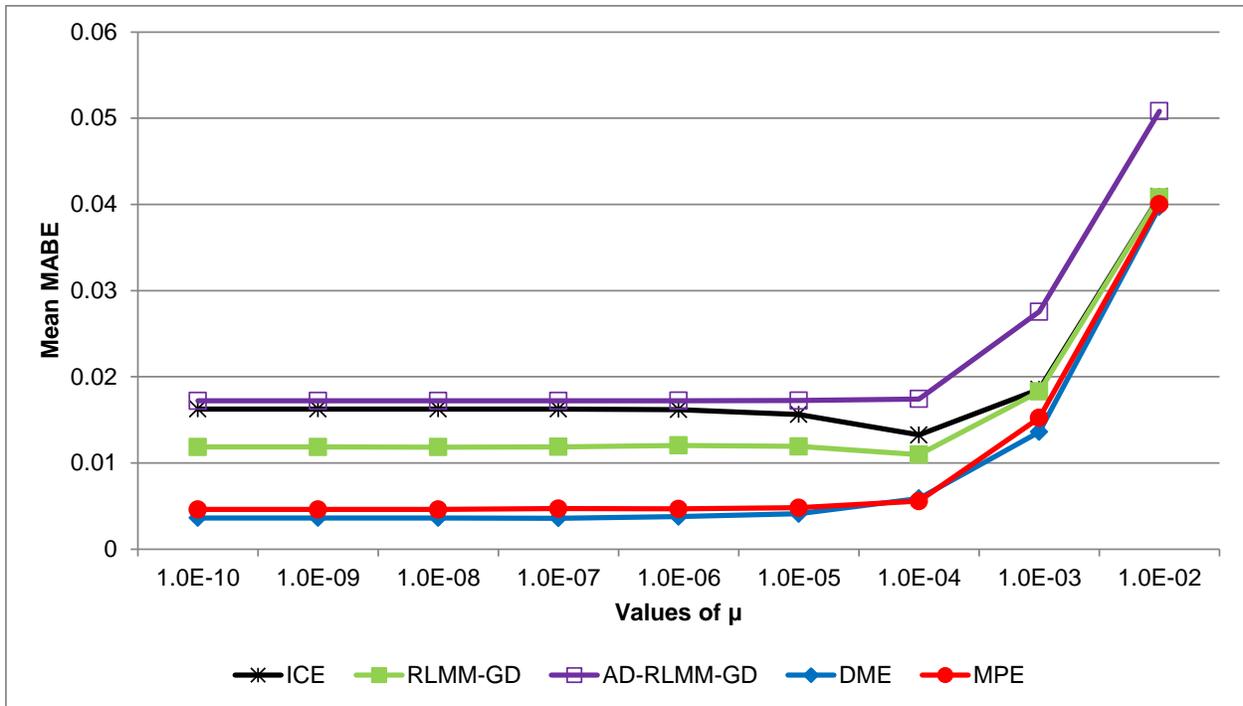


Figure 4-7. Mean MABE of synthetic CMM data sets over range of μ settings.

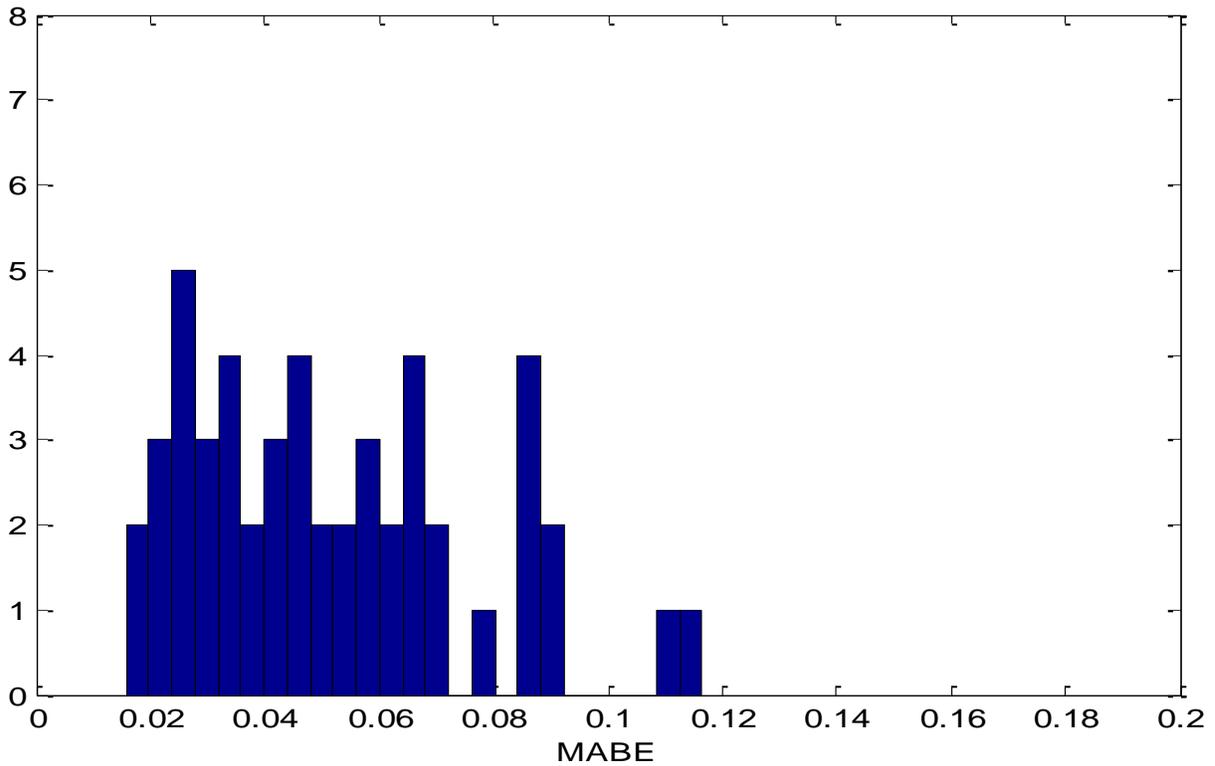


Figure 4-8. Histogram of ICE MABE using random starting points.

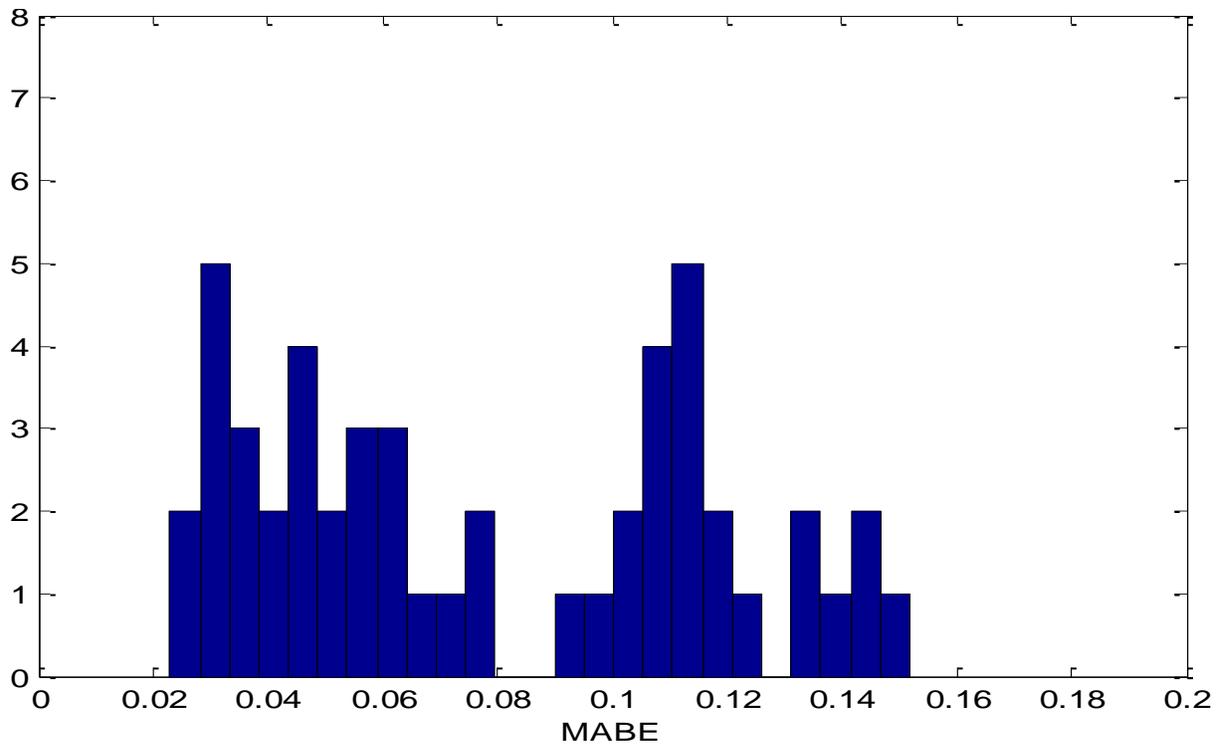


Figure 4-9. Histogram of RLMM-GD MABE using random starts.

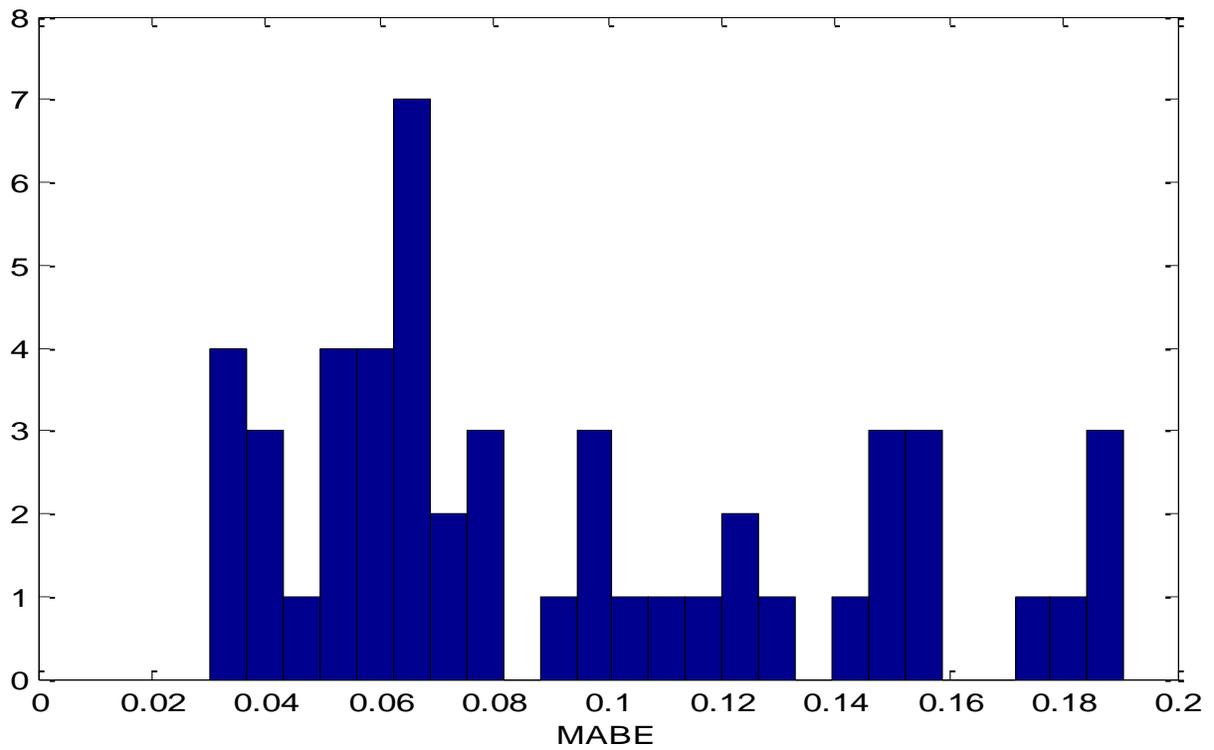


Figure 4-10. Histogram of AD-RLMM-GD MABE using random starts.

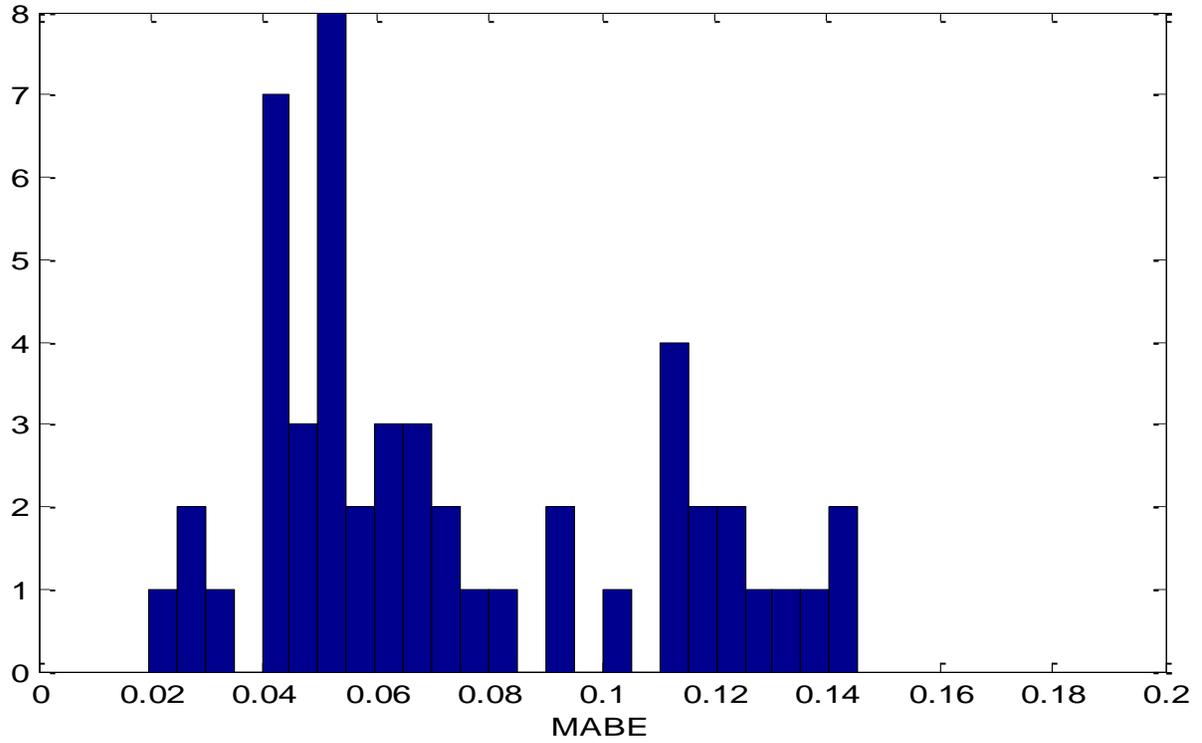


Figure 4-11. Histogram of DME MABE using random starts.

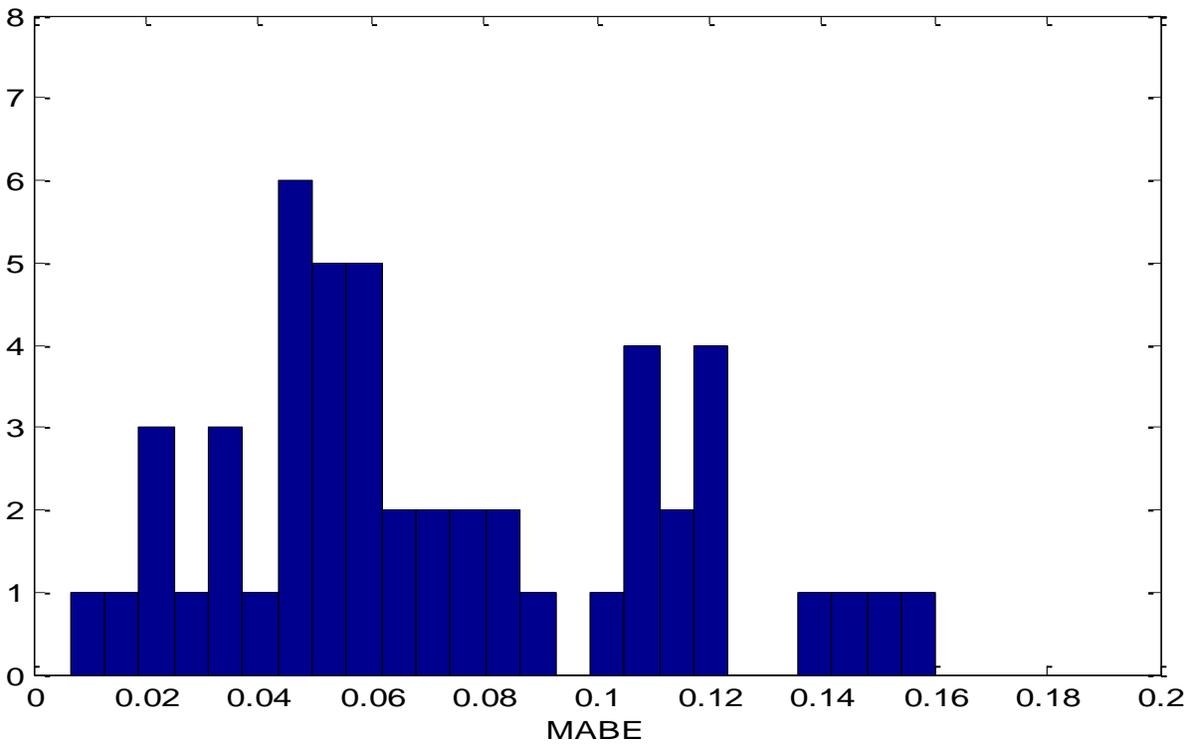


Figure 4-12. Histogram of MPE MABE using random starts.

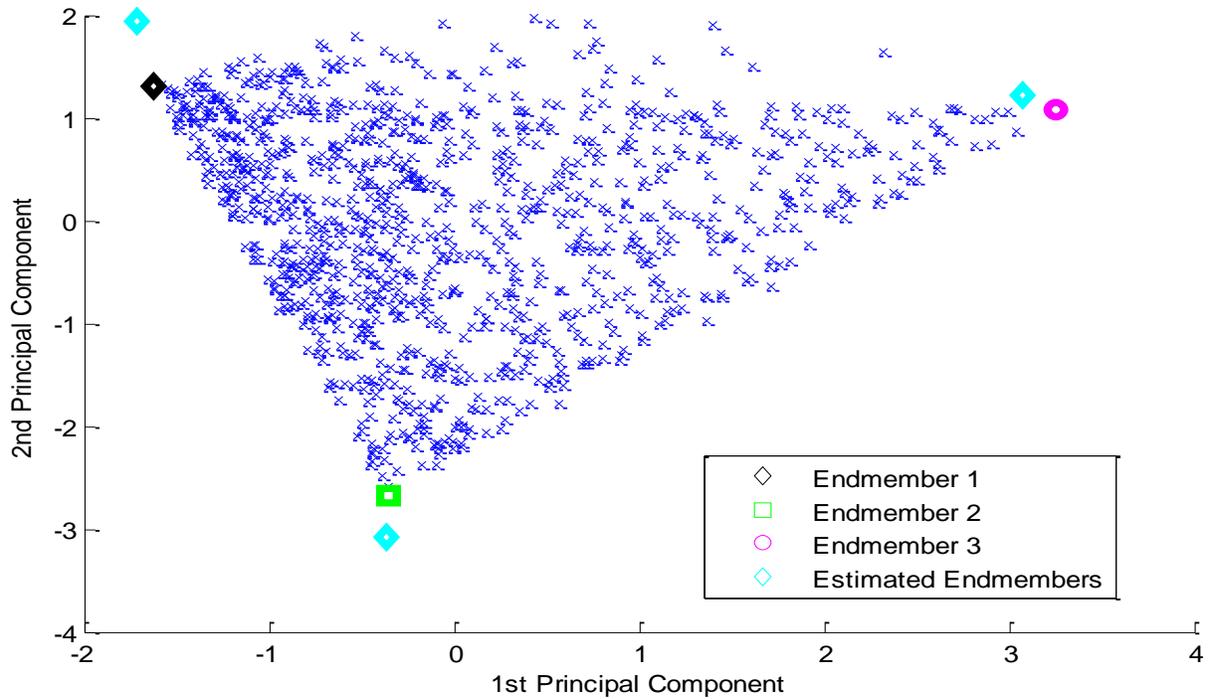


Figure 4-13. RLMM-GD estimated endmembers for CMM data set (1st and 2nd principal components).

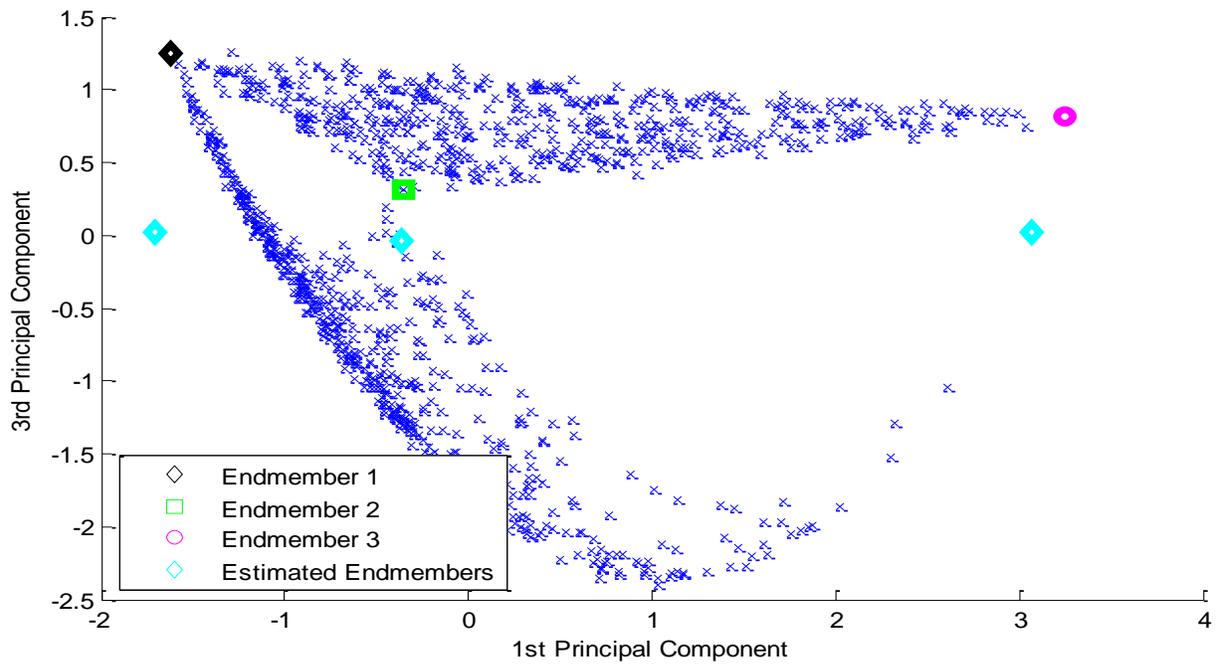


Figure 4-14. RLMM-GD estimated endmembers for CMM data set (1st and 3rd principal components).

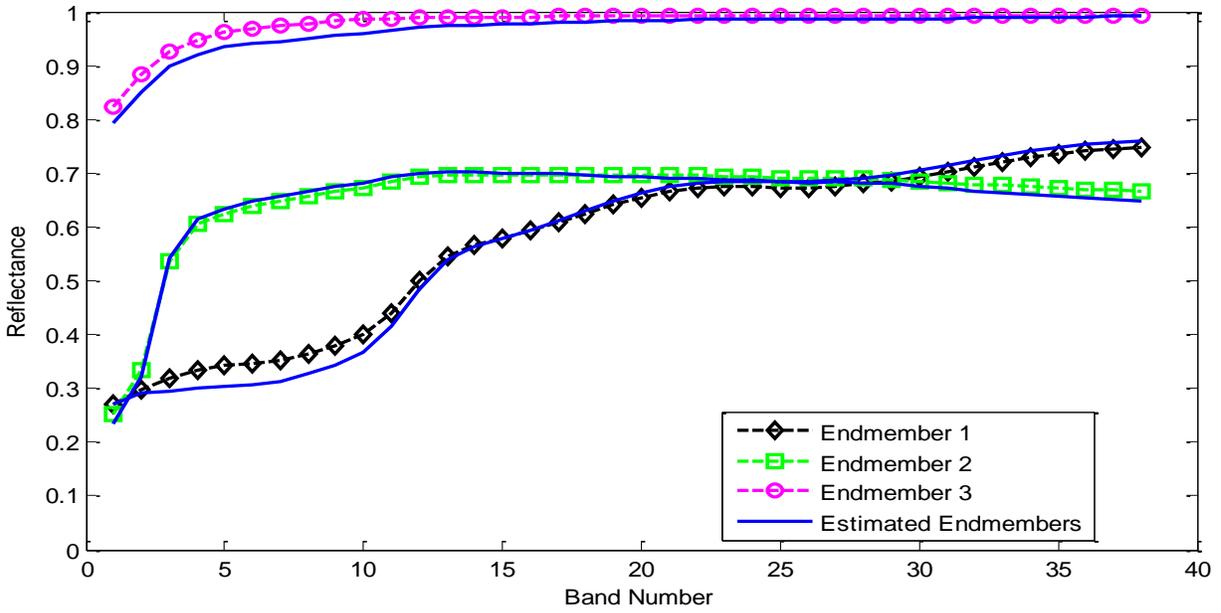


Figure 4-15. RLMM-GD estimated endmembers for CMM data set (spectra).

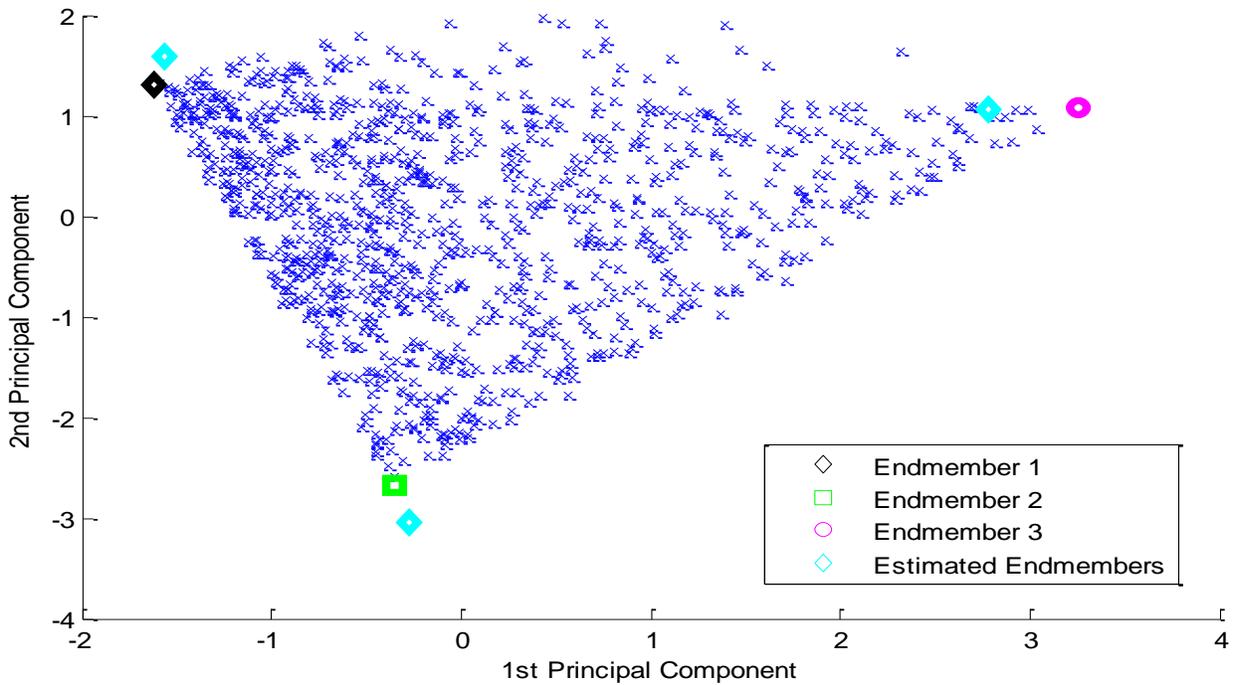


Figure 4-16. RLMM-GD estimated endmembers for CMM data set with $\mu = 1 \times 10^{-3}$ (1st and 2nd principal components).

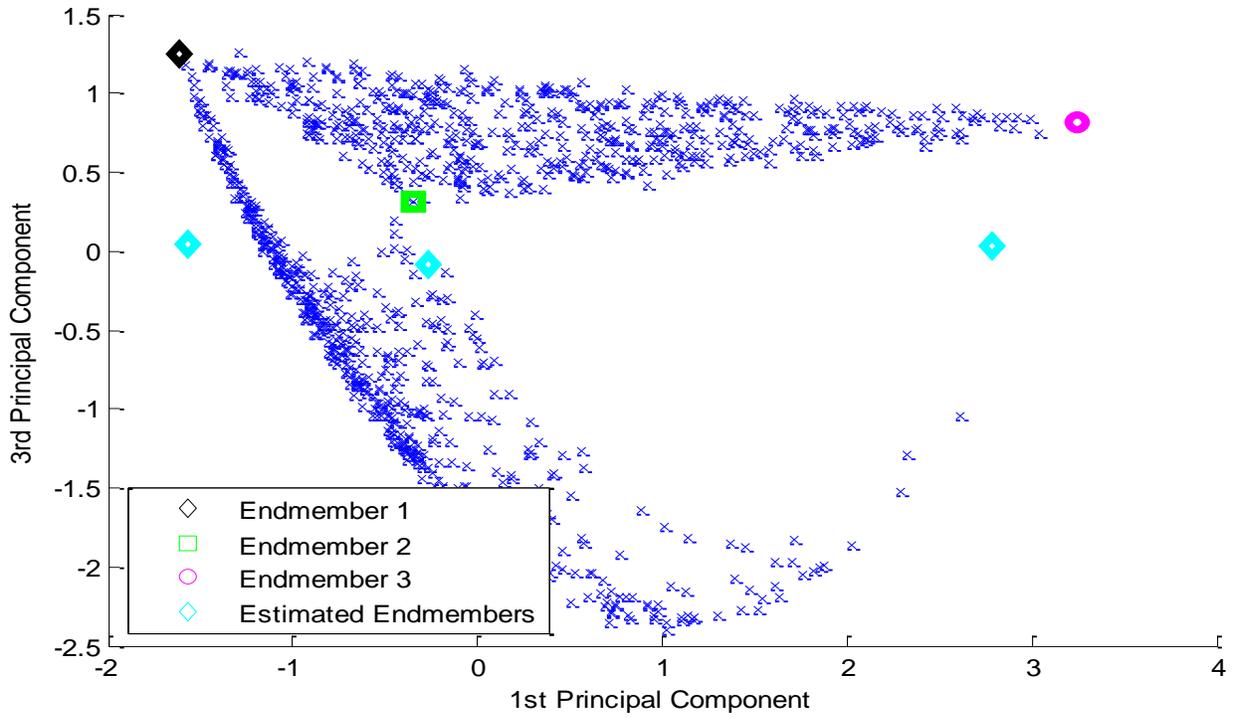


Figure 4-17. RLMM-GD estimated endmembers for CMM data set with $\mu = 1 \times 10^{-3}$ (1st and 3rd principal components).

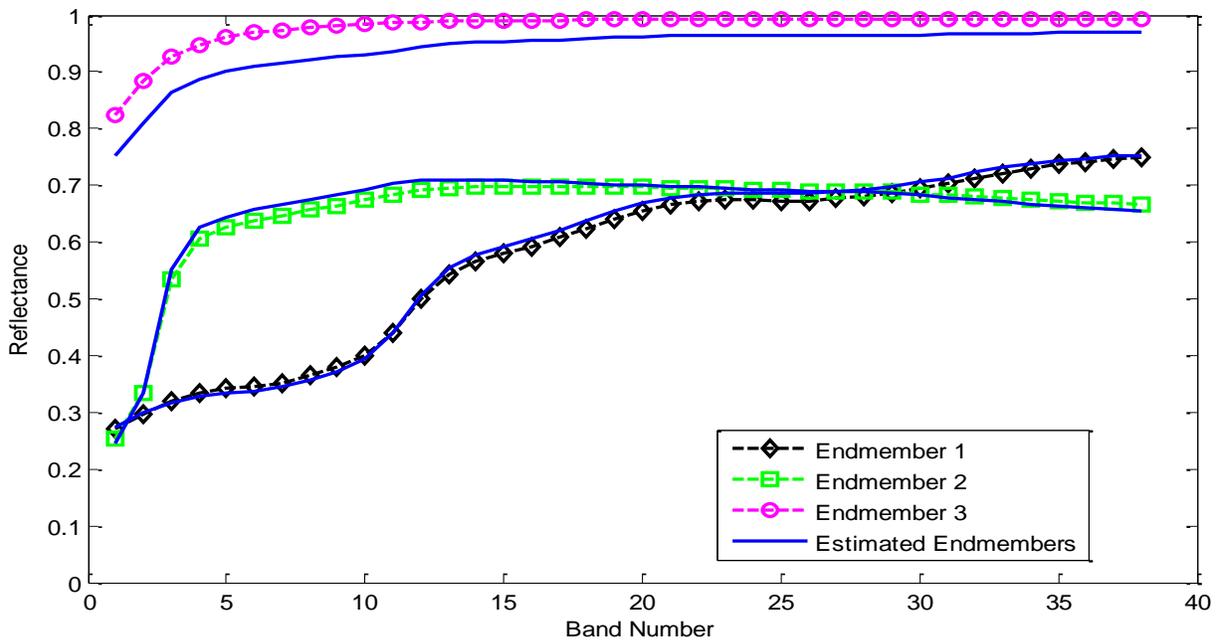


Figure 4-18. RLMM-GD estimated endmembers for CMM data set with $\mu = 1 \times 10^{-3}$ (spectra).

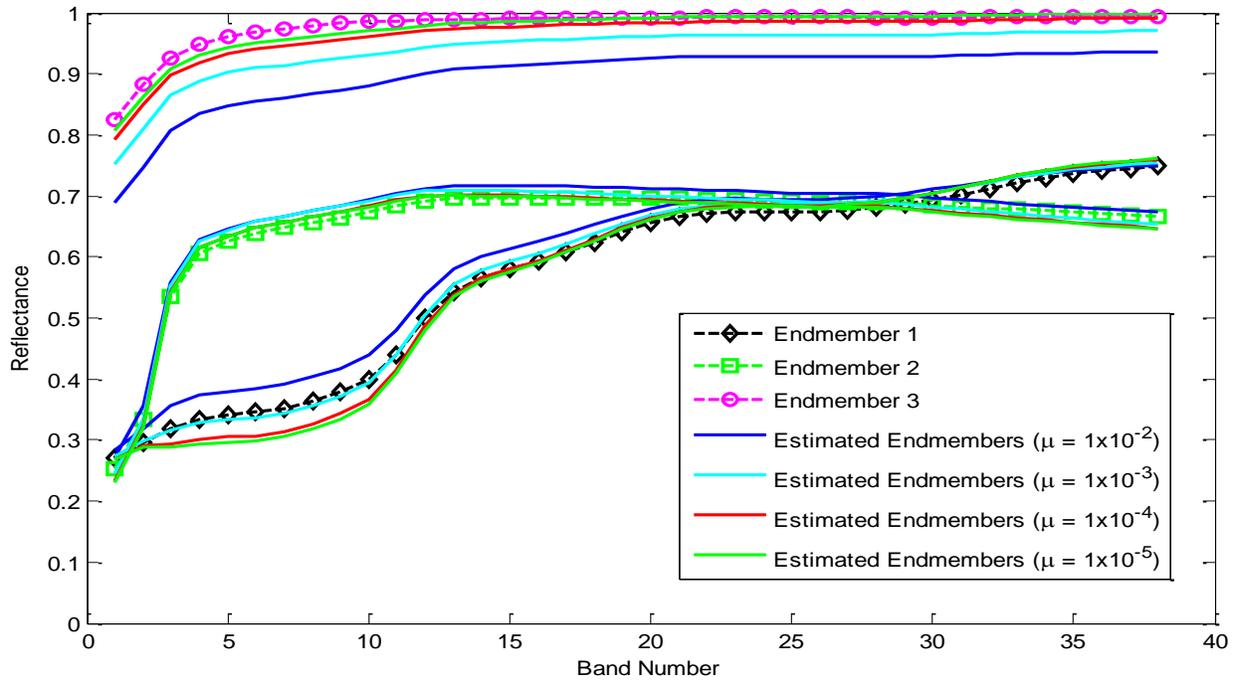


Figure 4-19. RLMM-GD estimated endmember spectra with multiple μ parameters.

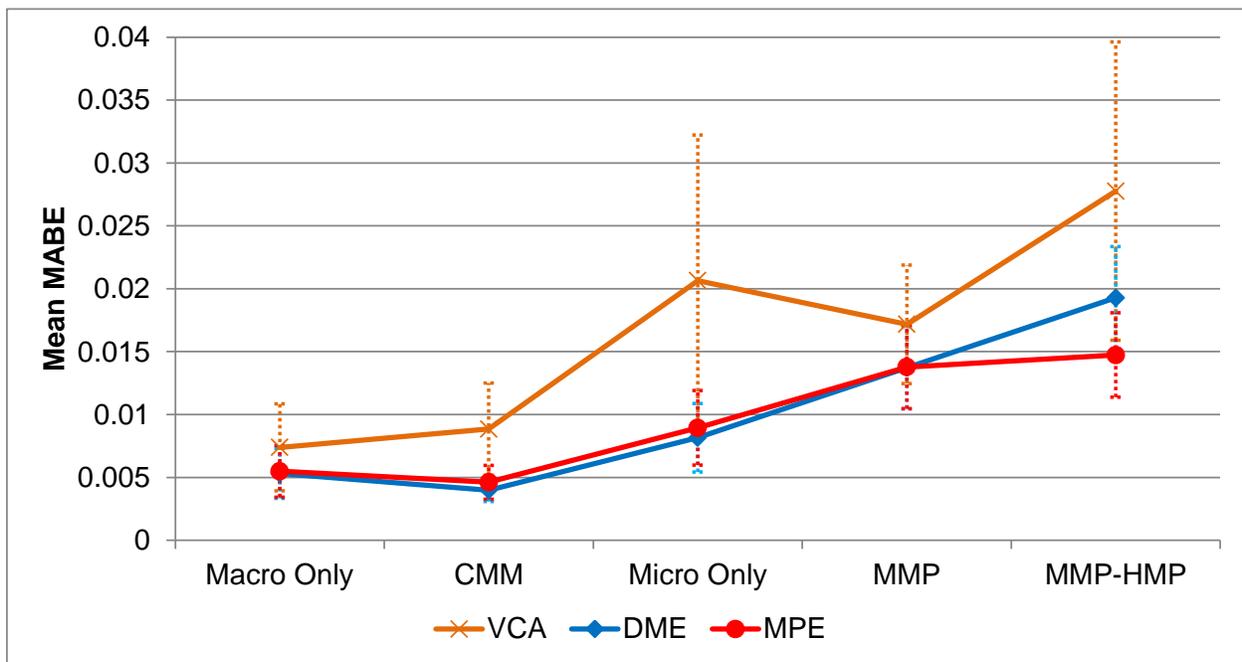


Figure 4-20. Mean MABE of VCA, DME, and MPE.

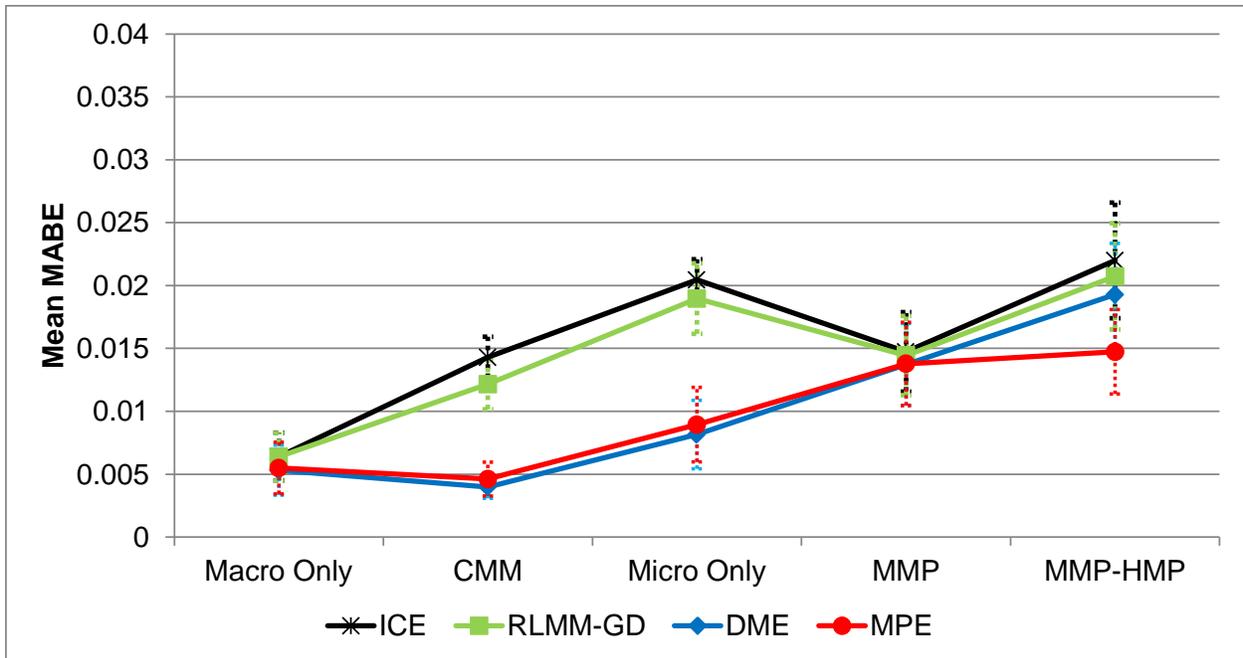


Figure 4-21. Mean MABE of ICE, RLMM-GD, DME, and MPE.

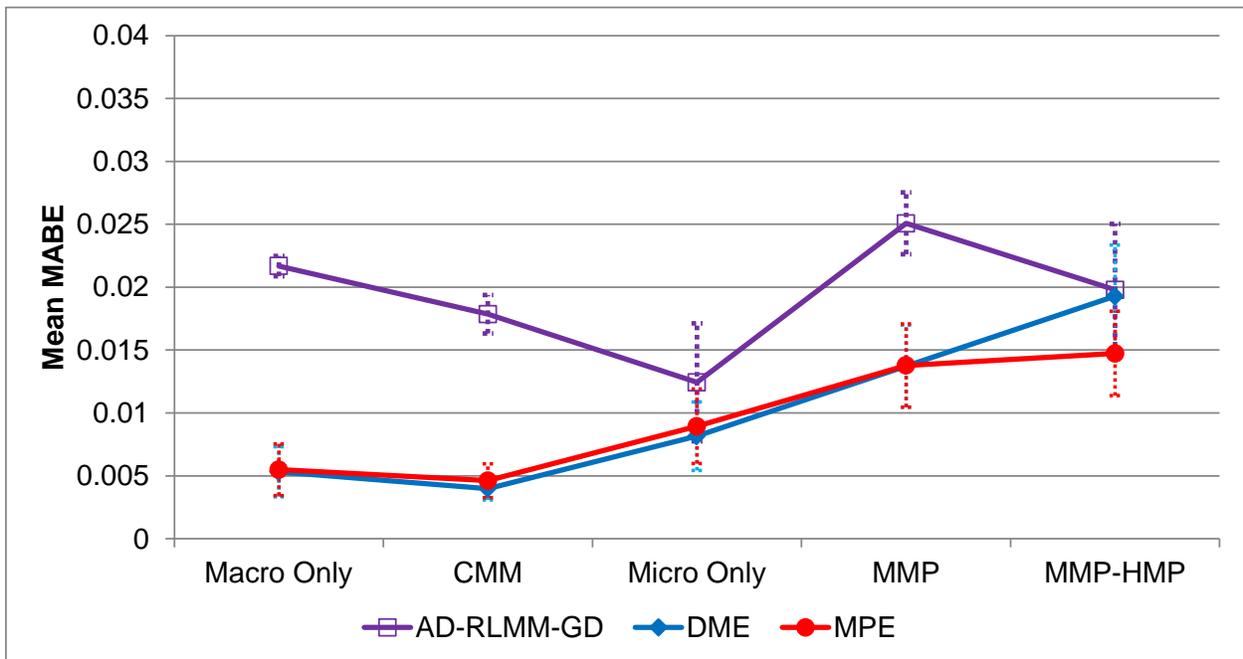


Figure 4-22. Mean MABE of AD-RLMM-GD, DME, and MPE.

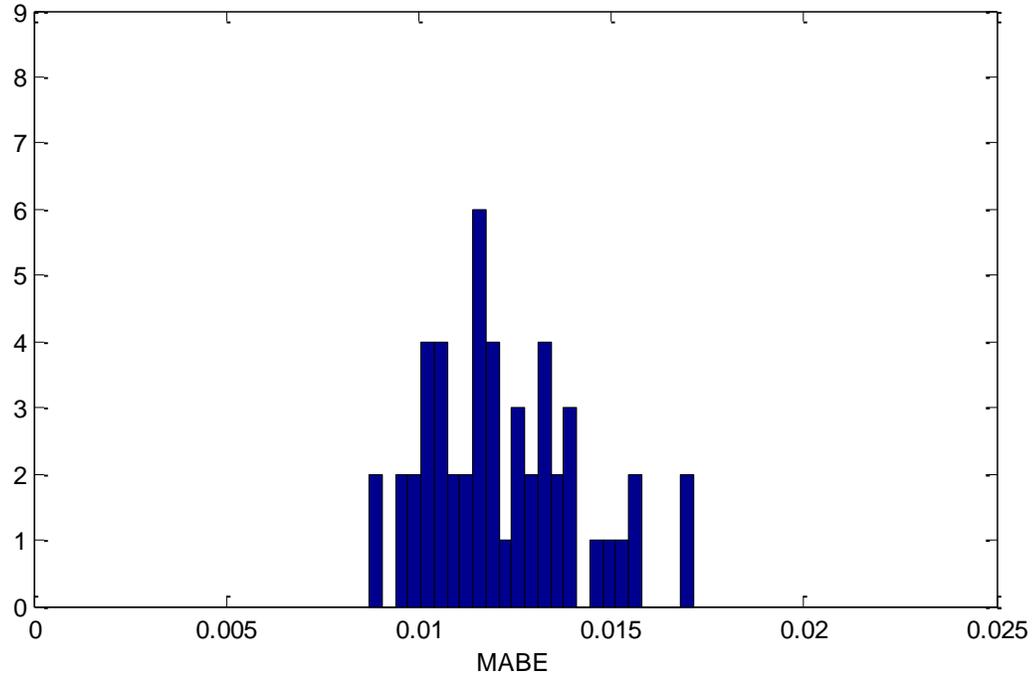


Figure 4-25. Histogram of RLMM-GD MABE values for CMM data set.

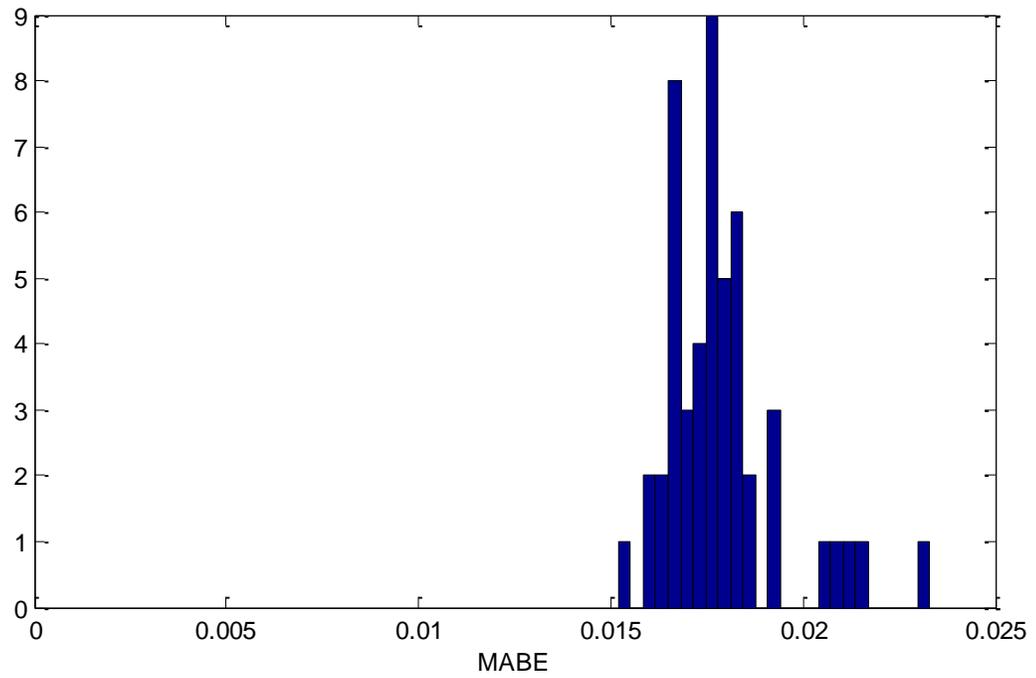


Figure 4-26. Histogram of AD-RLMM-GD MABE values for CMM data set.

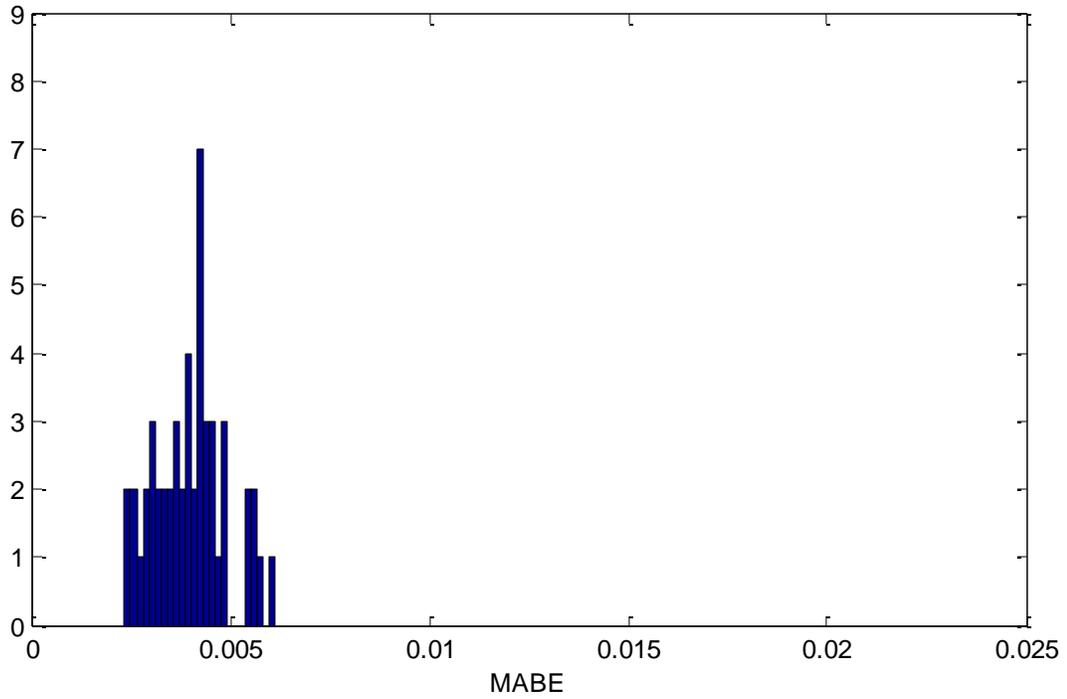


Figure 4-27. Histogram of DME MABE values for CMM data set.

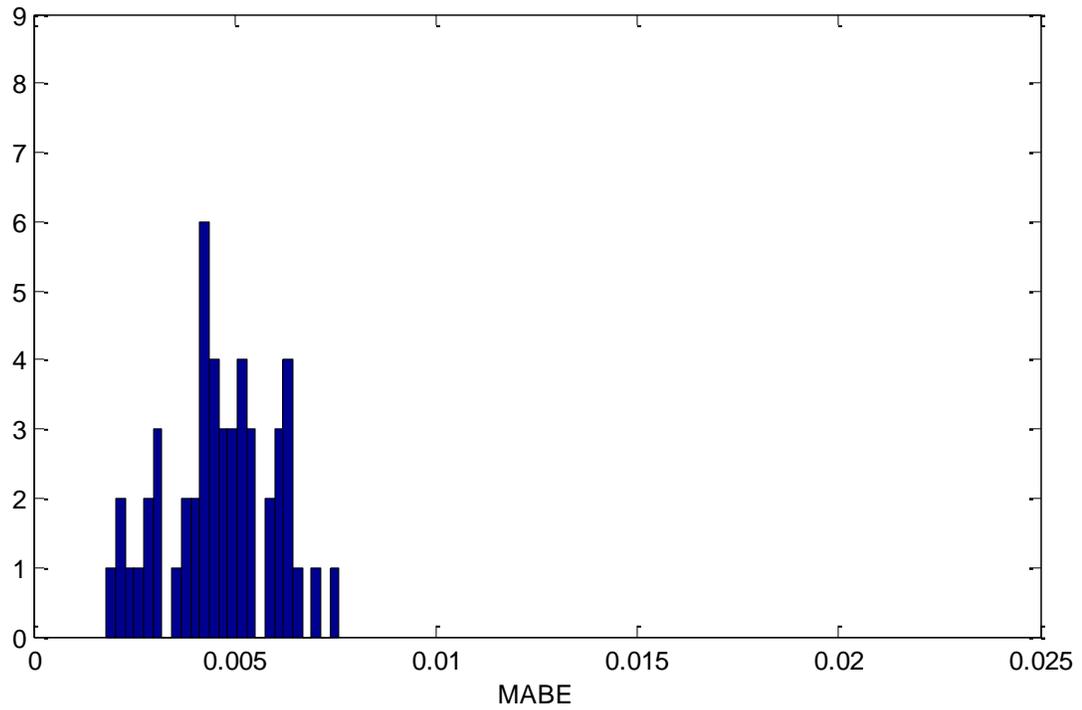


Figure 4-28. Histogram of MPE MABE values for CMM data set.

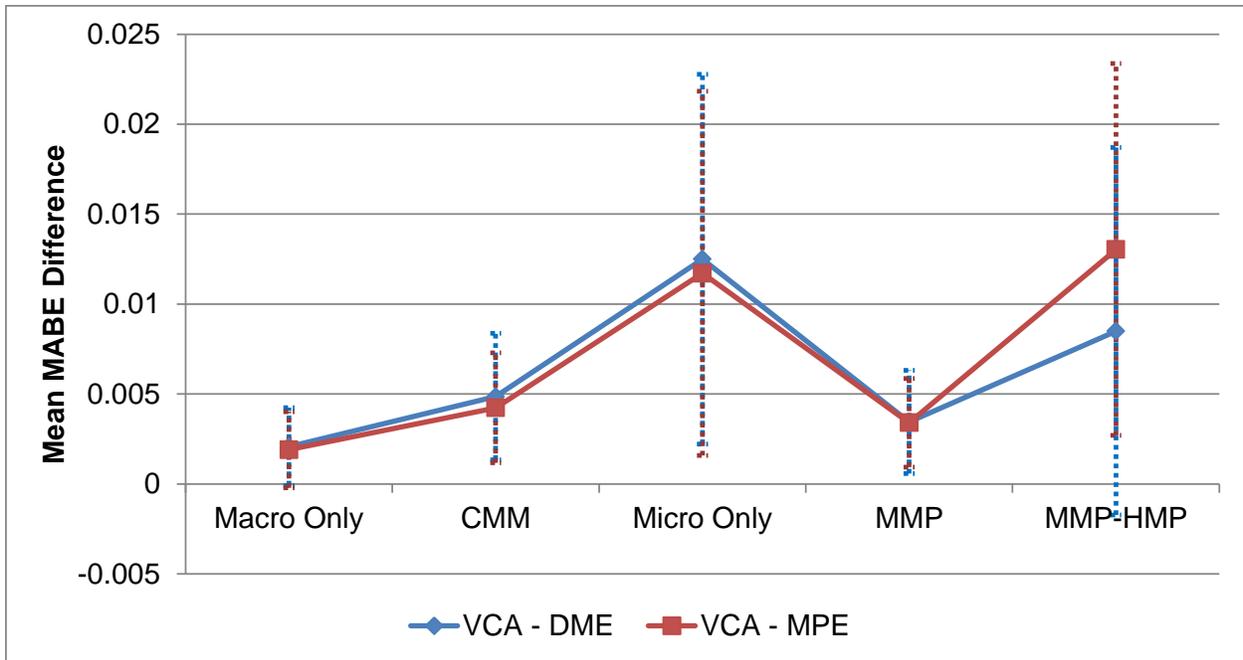


Figure 4-29. Mean MABE difference between VCA and DME and MPE.

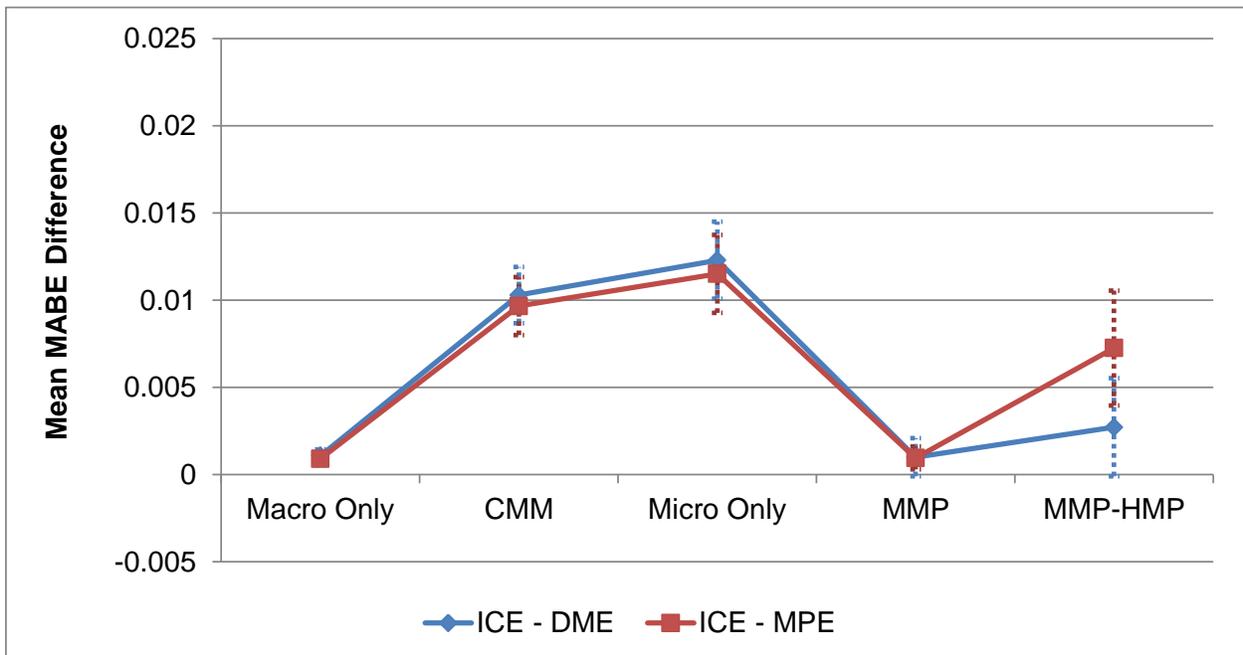


Figure 4-30. Mean MABE difference between ICE and DME and MPE.

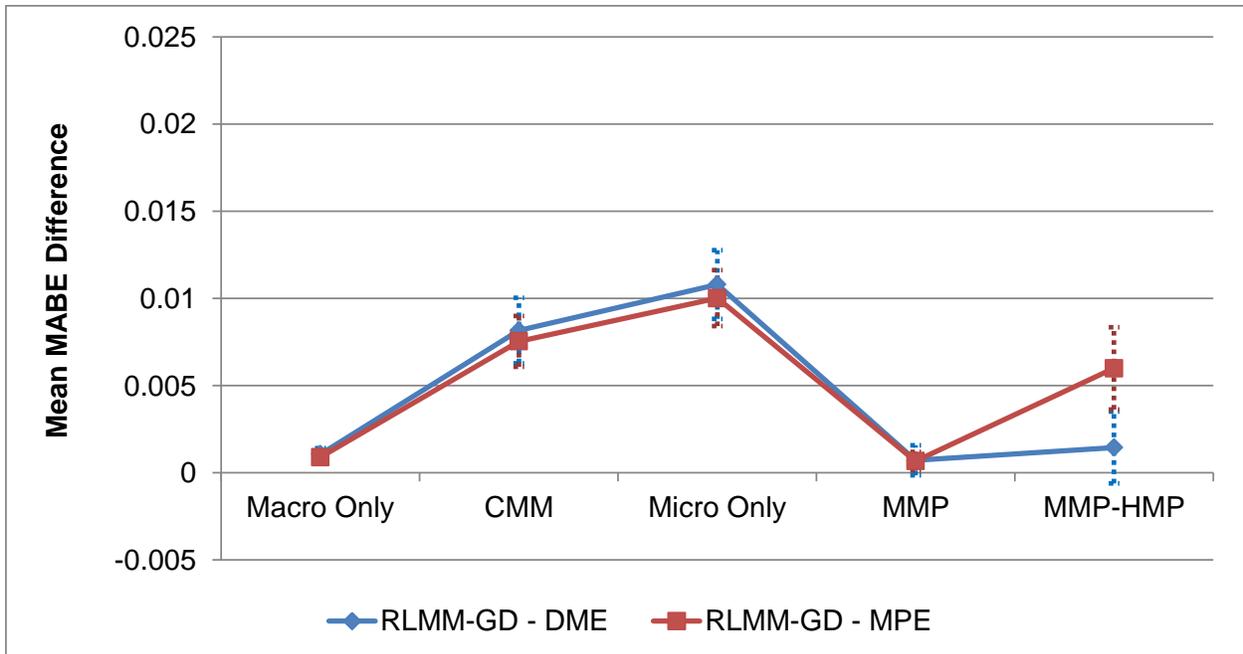


Figure 4-31. Mean MABE difference between RLMM-GD and DME and MPE.

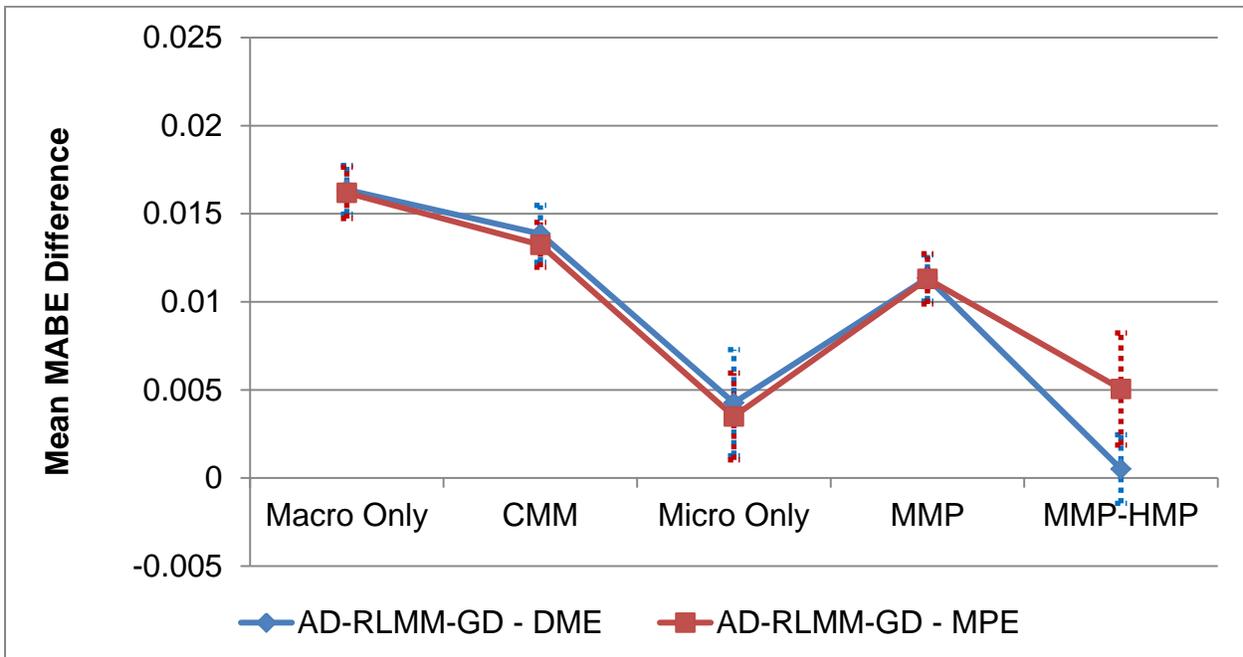


Figure 4-32. Mean MABE difference between AD-RLMM-GD and DME and MPE.

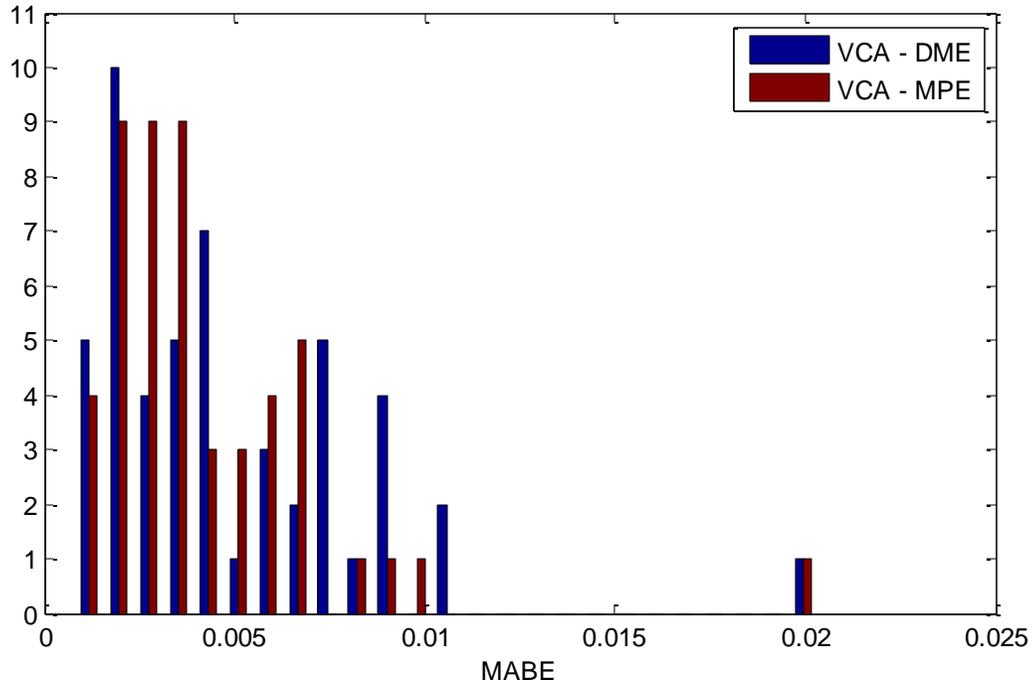


Figure 4-33. Histogram of MABE difference between VCA and DME and MPE for CMM data set.

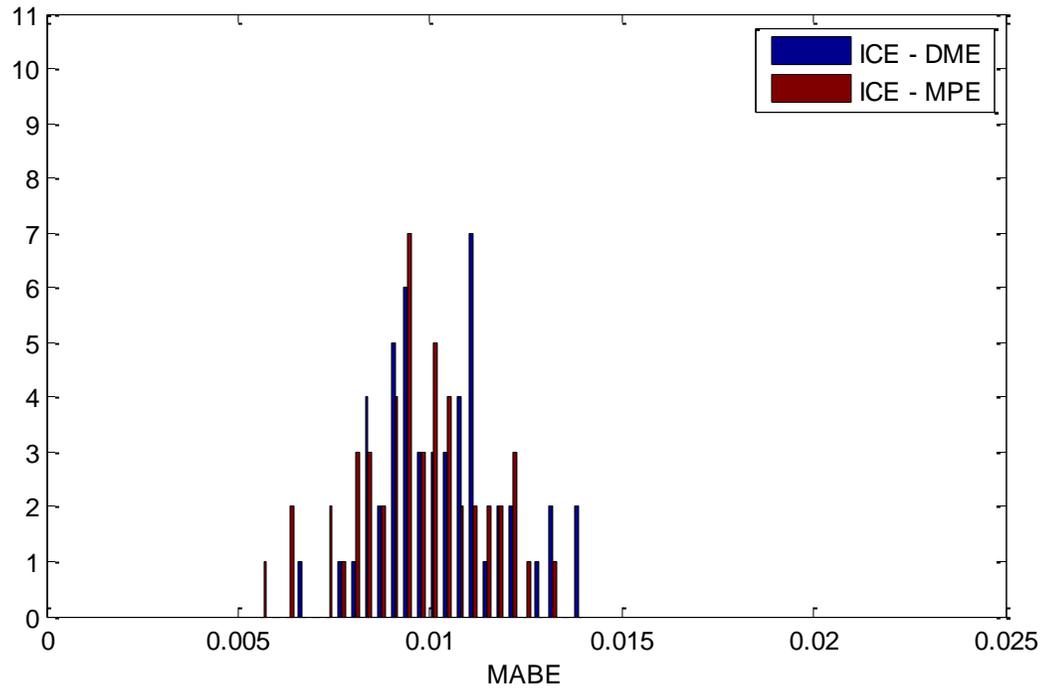


Figure 4-34. Histogram of MABE difference between ICE and DME and MPE for CMM data set.

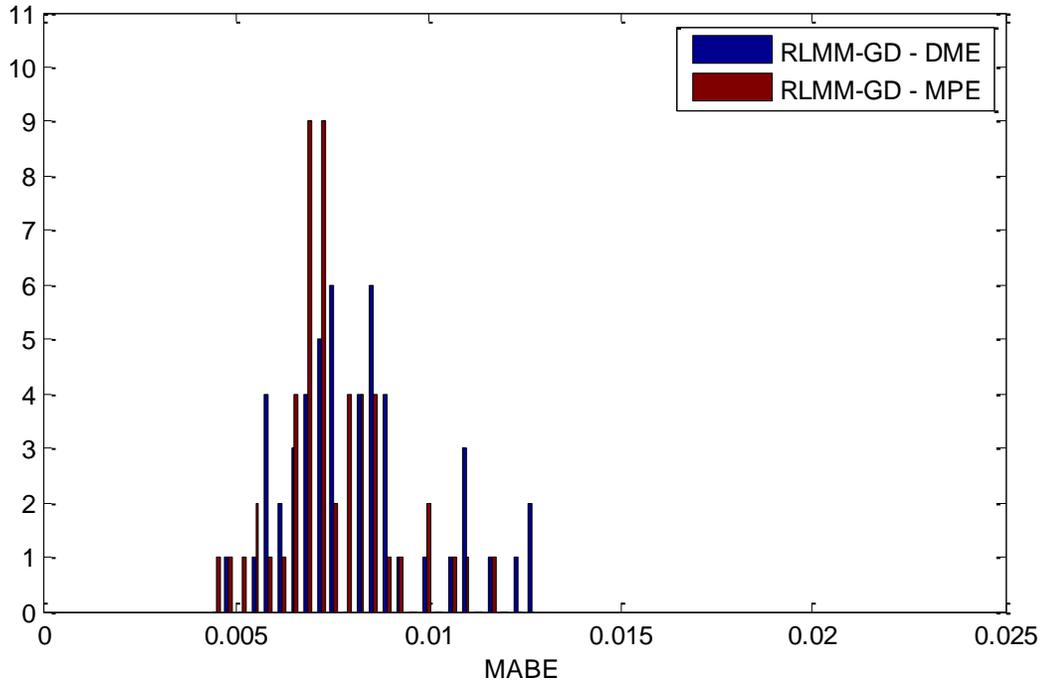


Figure 4-35. Histogram of MABE difference between RLMM-GD and DME and MPE for CMM data set.

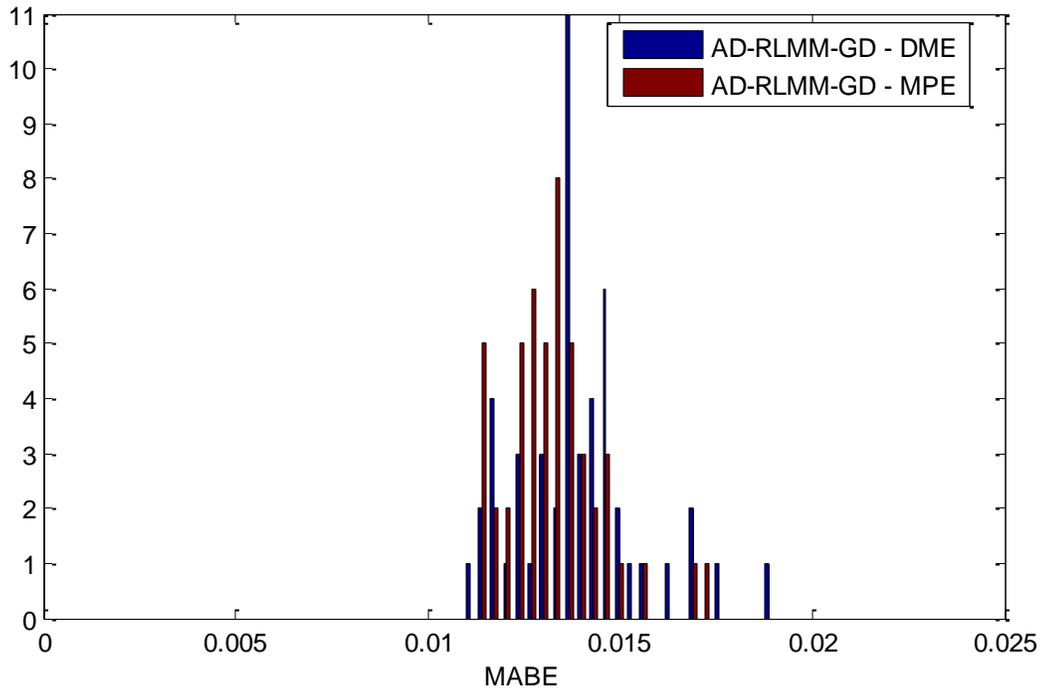


Figure 4-36. Histogram of MABE difference between AD-RLMM-GD and DME and MPE for CMM data set.

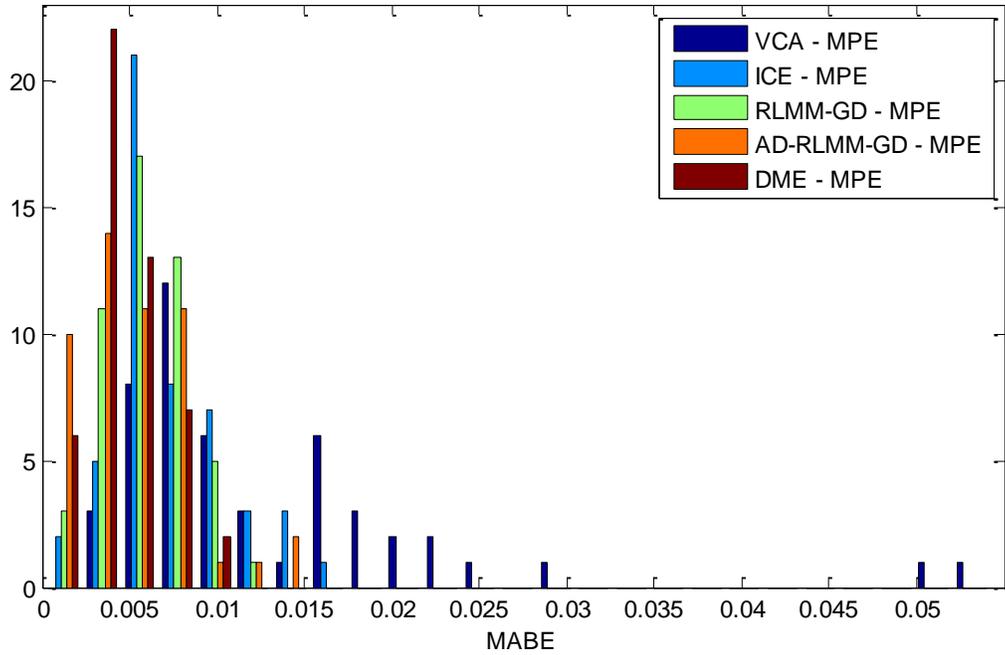


Figure 4-37. Histogram of MABE difference between VCA, ICE, RLMM-GD, AD-RLMM-GD, and DME and MPE for MMP-HMP data set.

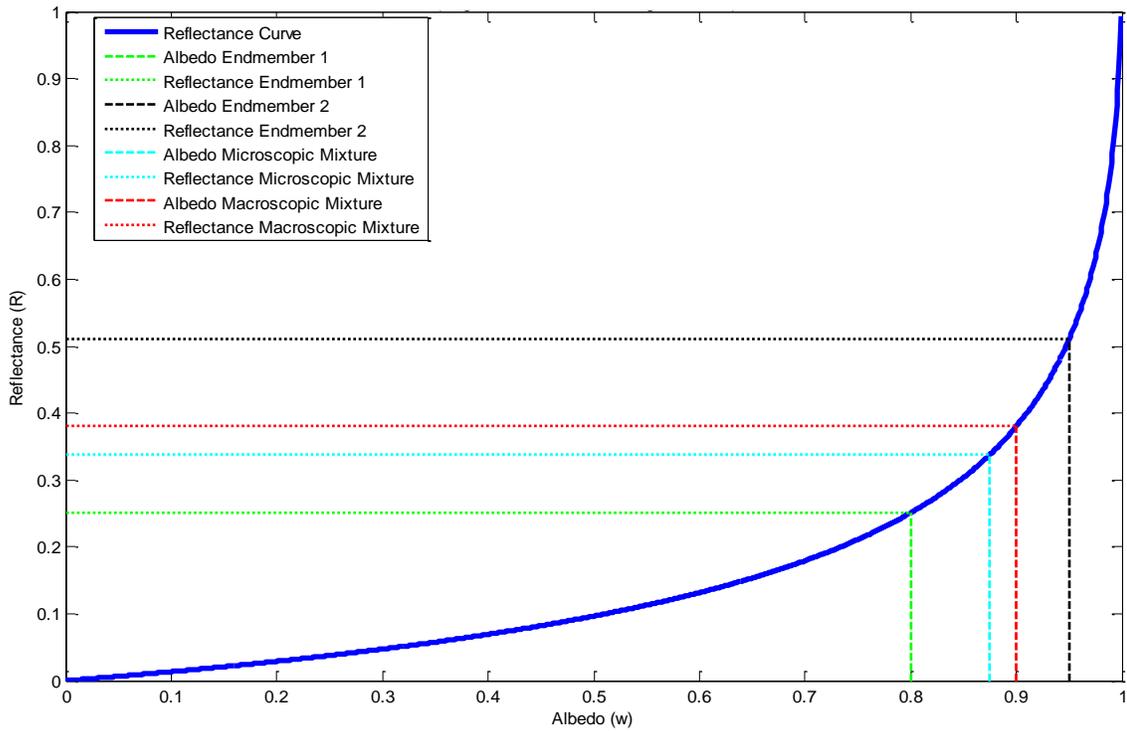


Figure 4-38. Comparison of nonlinearity in albedo-domain and reflectance-domain mixtures. Each mixture was created with a 50% proportion of each endmember. Angles of incidence and emergence were both 0° .

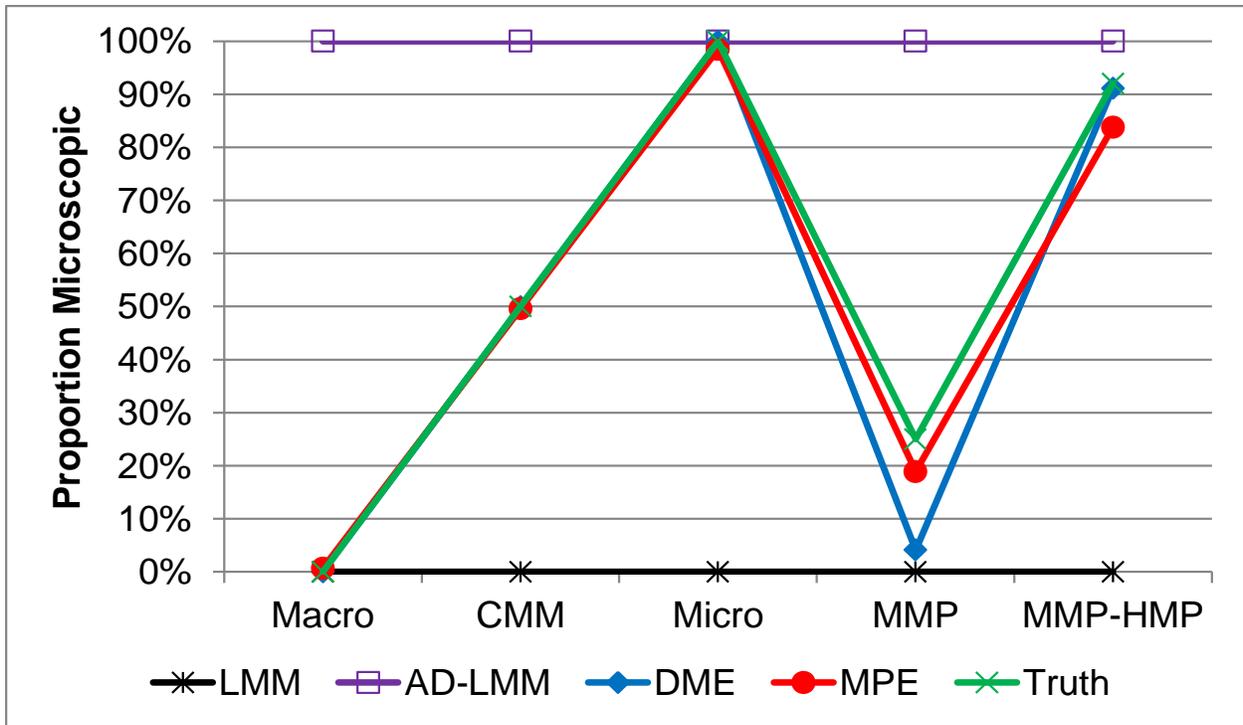


Figure 4-39. Microscopic proportions resulting from LMM, AD-LMM, DME, and MPE over all synthetic data sets.

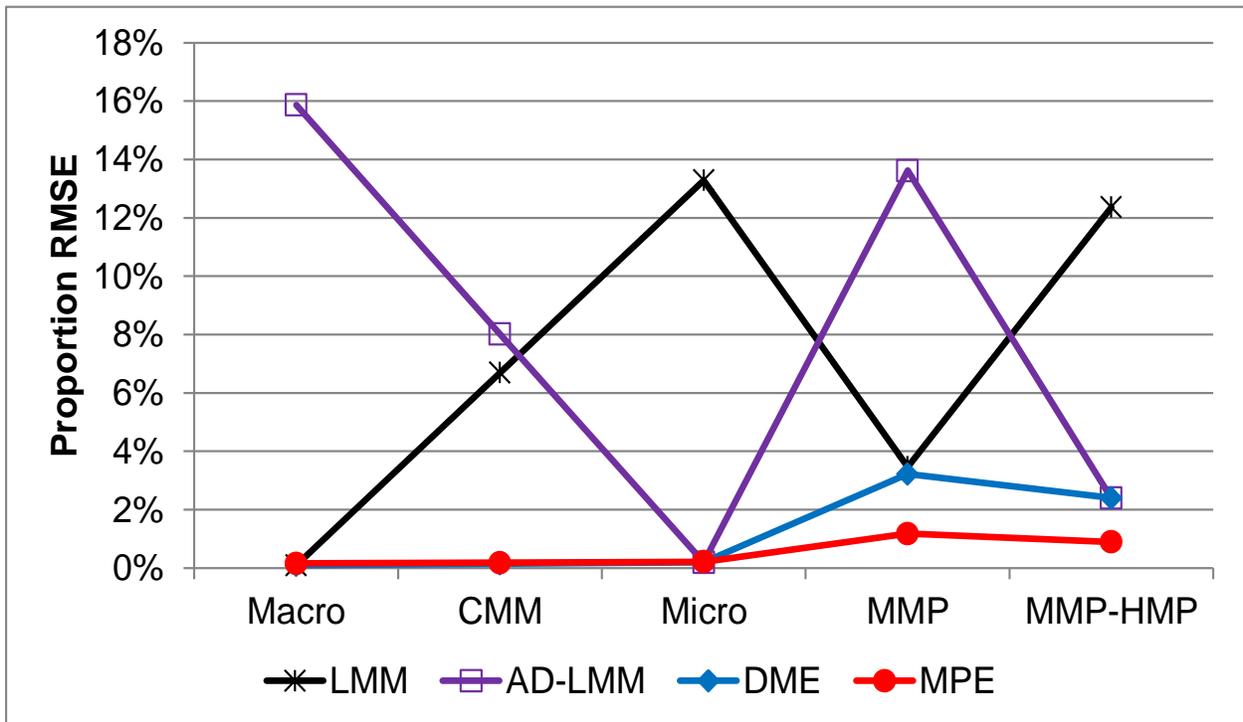


Figure 4-40. Proportion RMSE resulting from LMM, AD-LMM, DME, and MPE over all synthetic data sets.

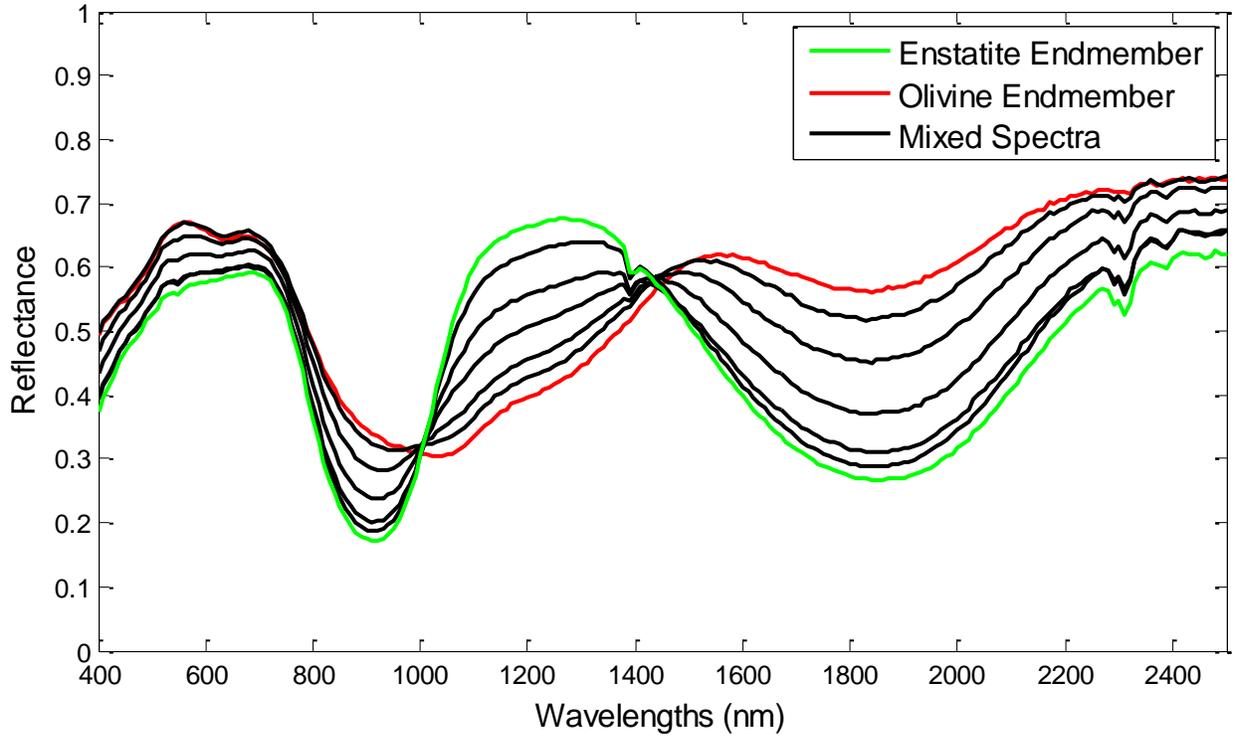


Figure 4-41. Spectra of Enstatite and Olivine mixture.

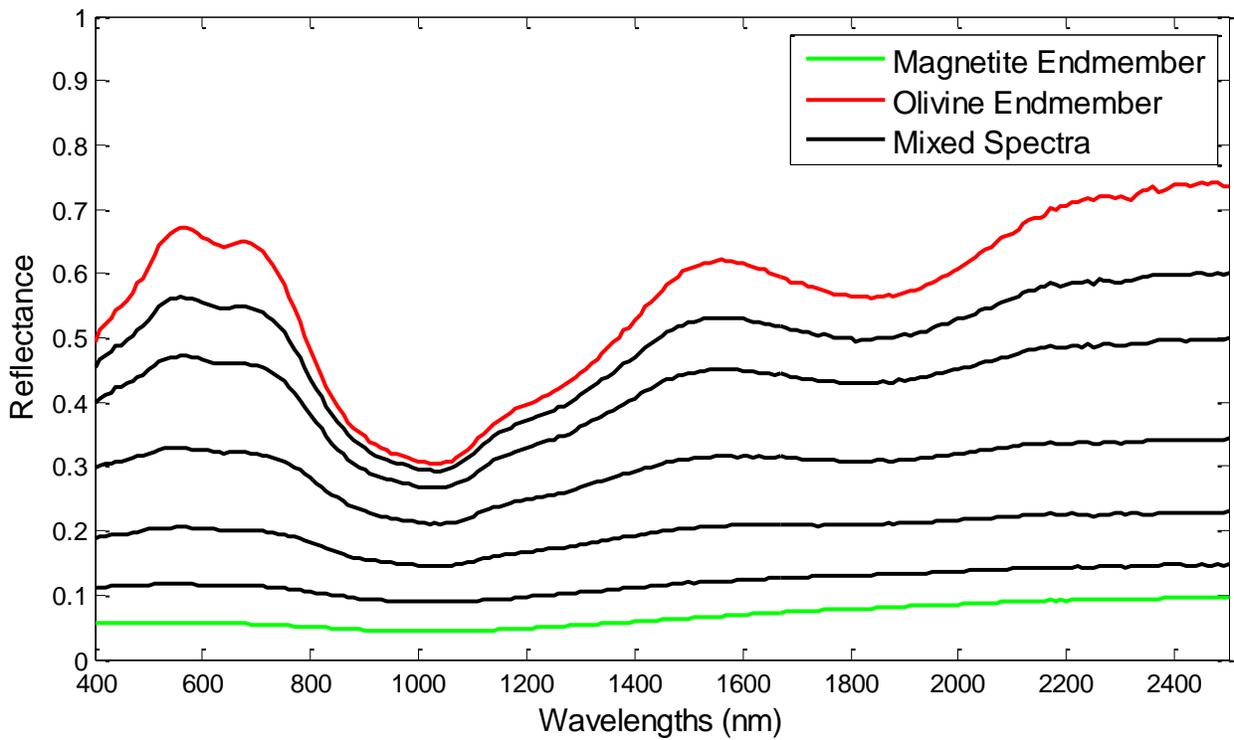


Figure 4-42. Spectra of Magnetite and Olivine mixture.

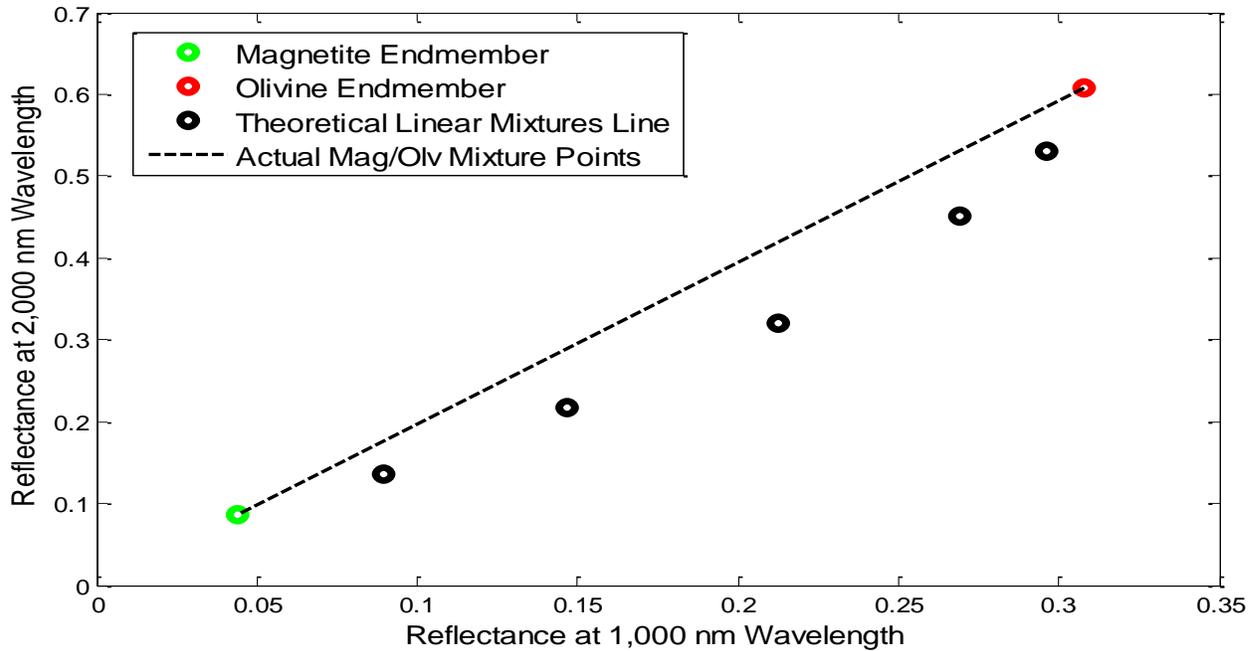


Figure 4-43. Wavelength scatter plot of Magnetite and Olivine mixture.

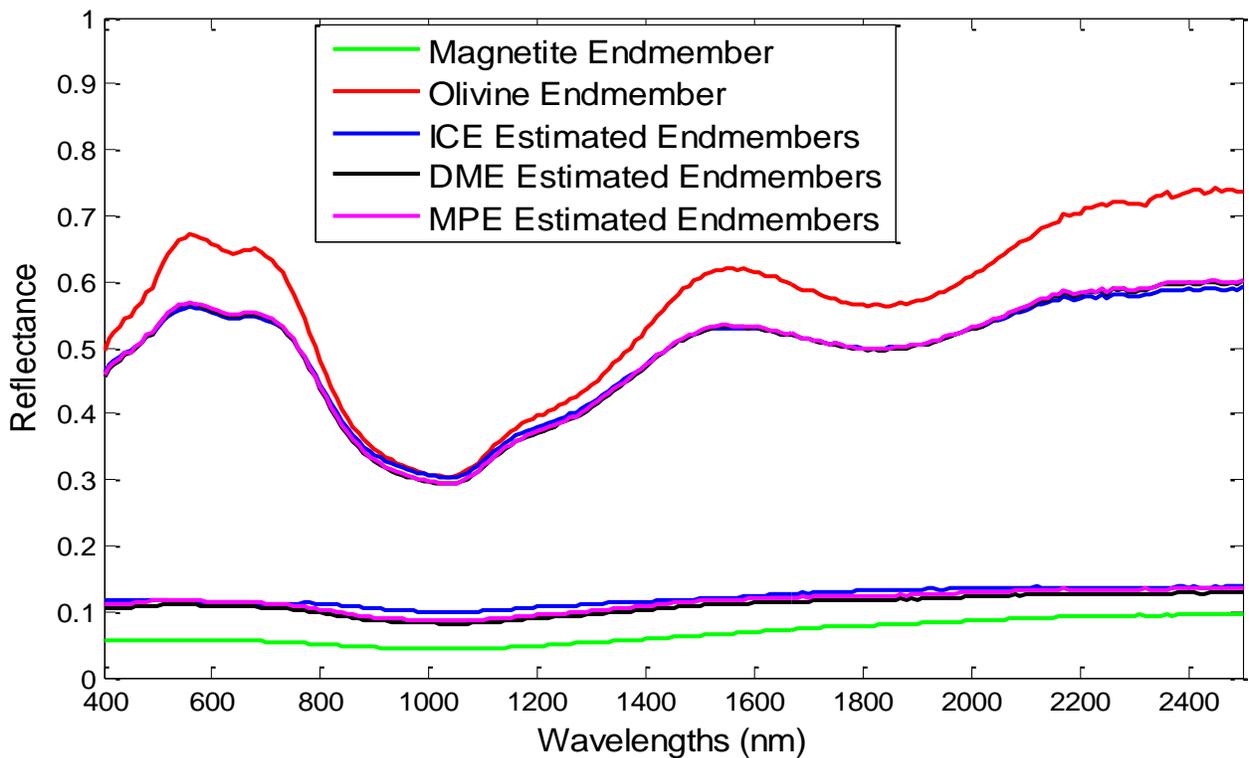


Figure 4-44. Endmember estimation of RELAB Magnetite and Olivine mixture.

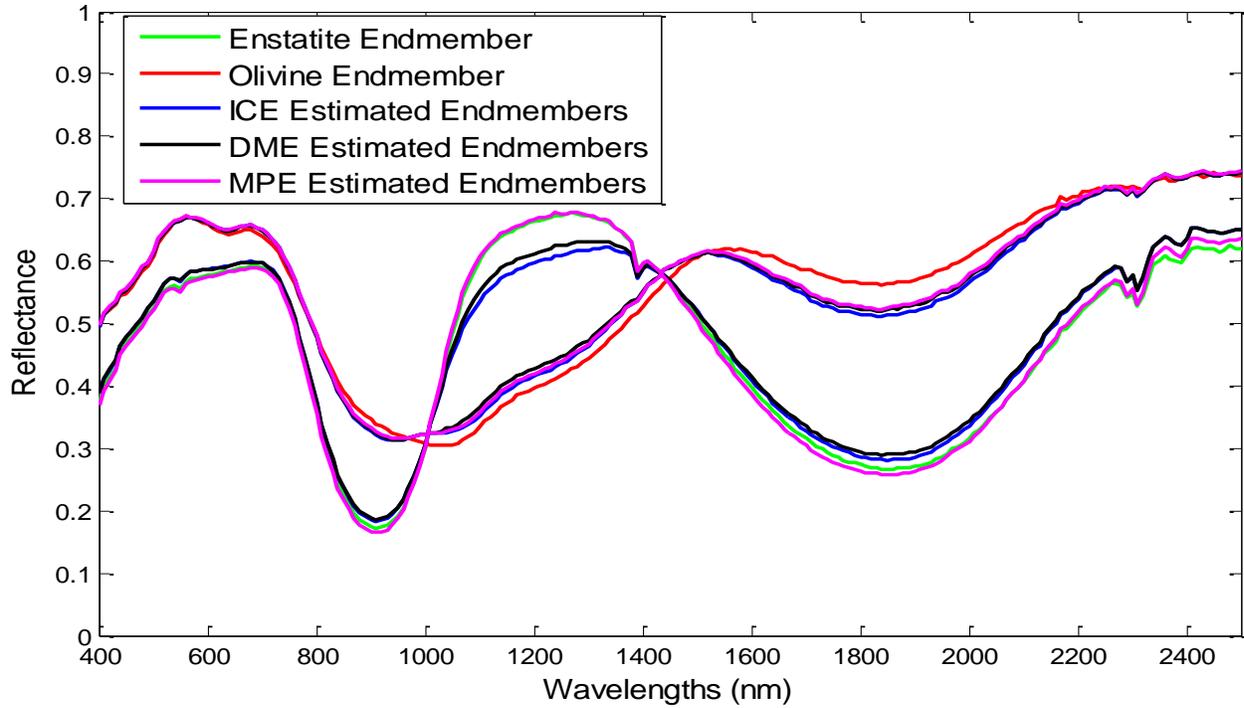


Figure 4-45. Endmember estimation of RELAB Enstatite and Olivine mixture.

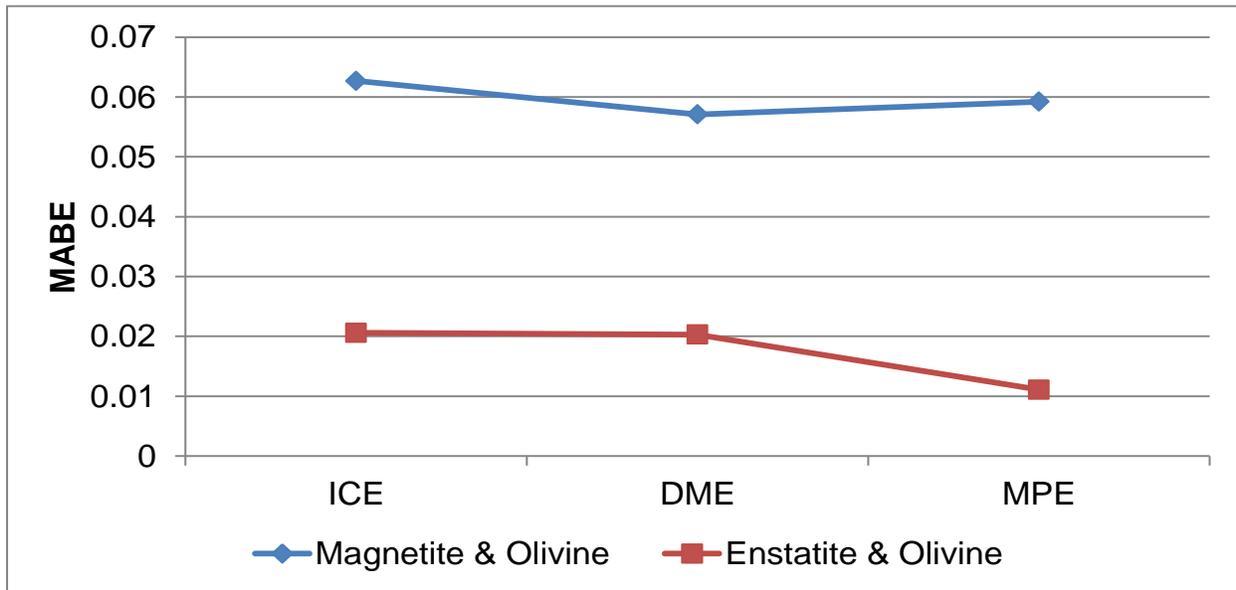


Figure 4-46. RELAB data sets endmember estimation error chart.



Figure 4-47. Baseball diamond scene.

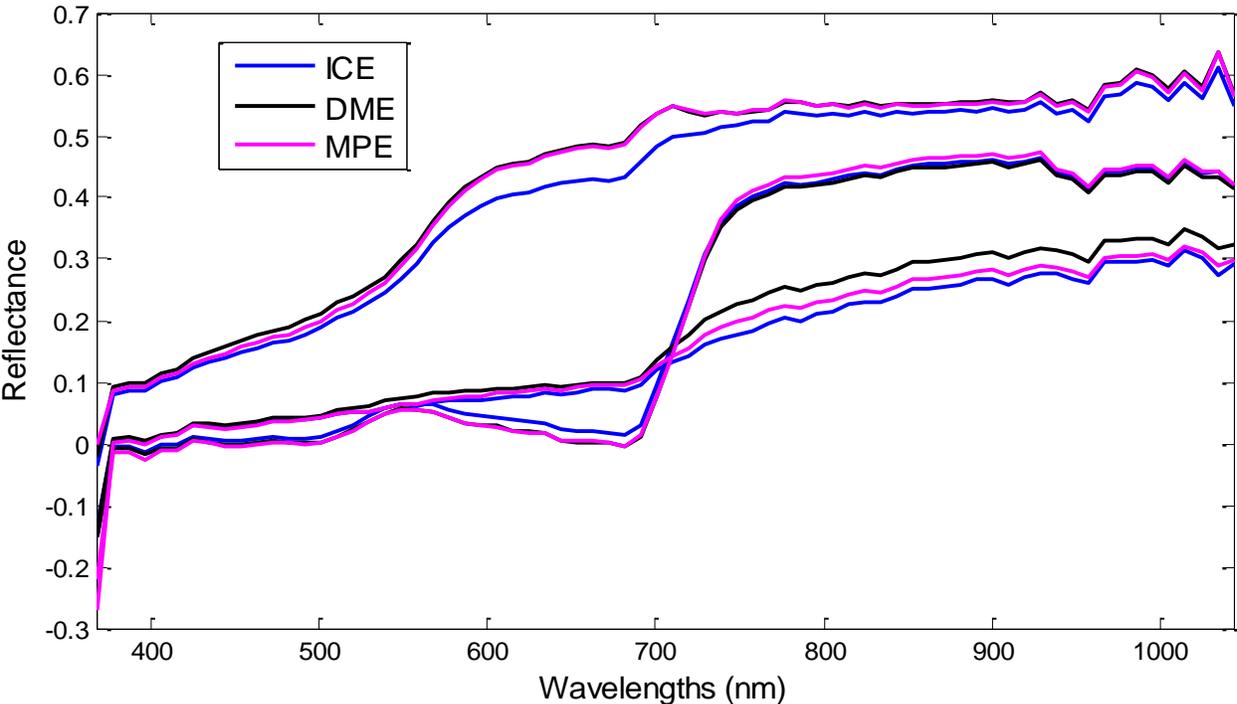


Figure 4-48. Endmembers estimated from baseball diamond scene.

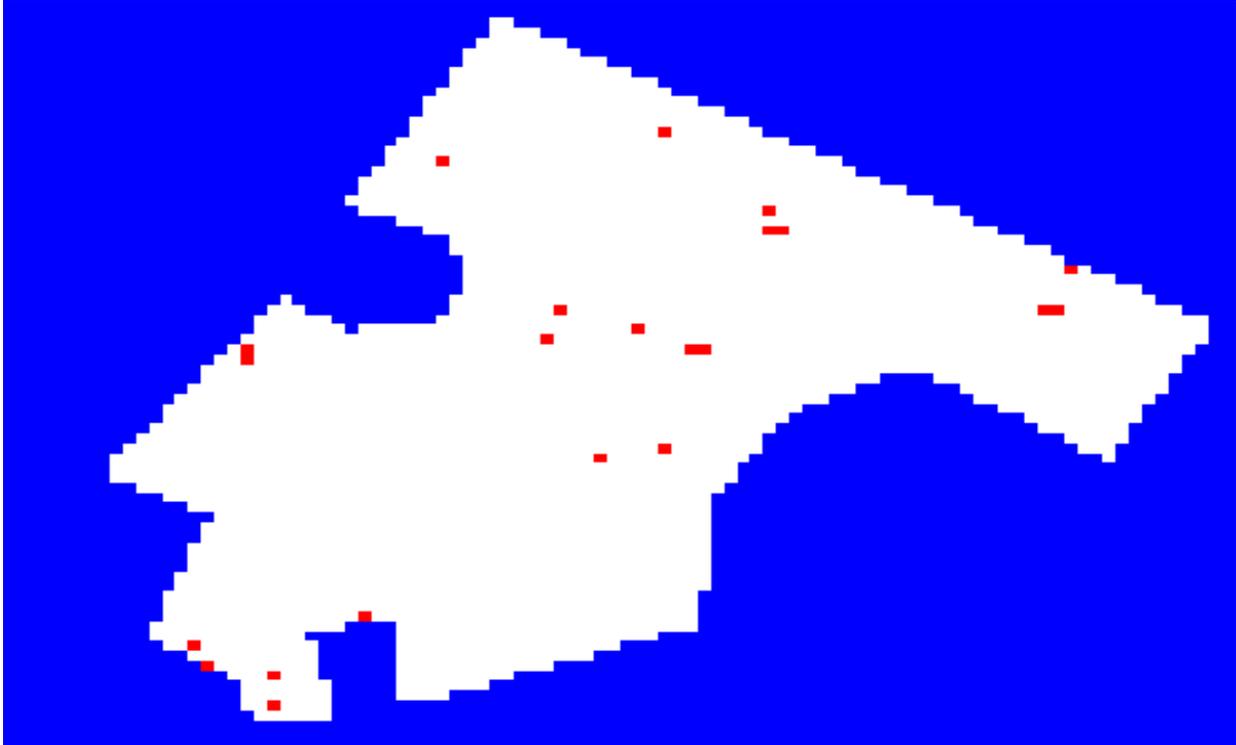


Figure 4-49. Points labeled by DME (red) as microscopically mixed.

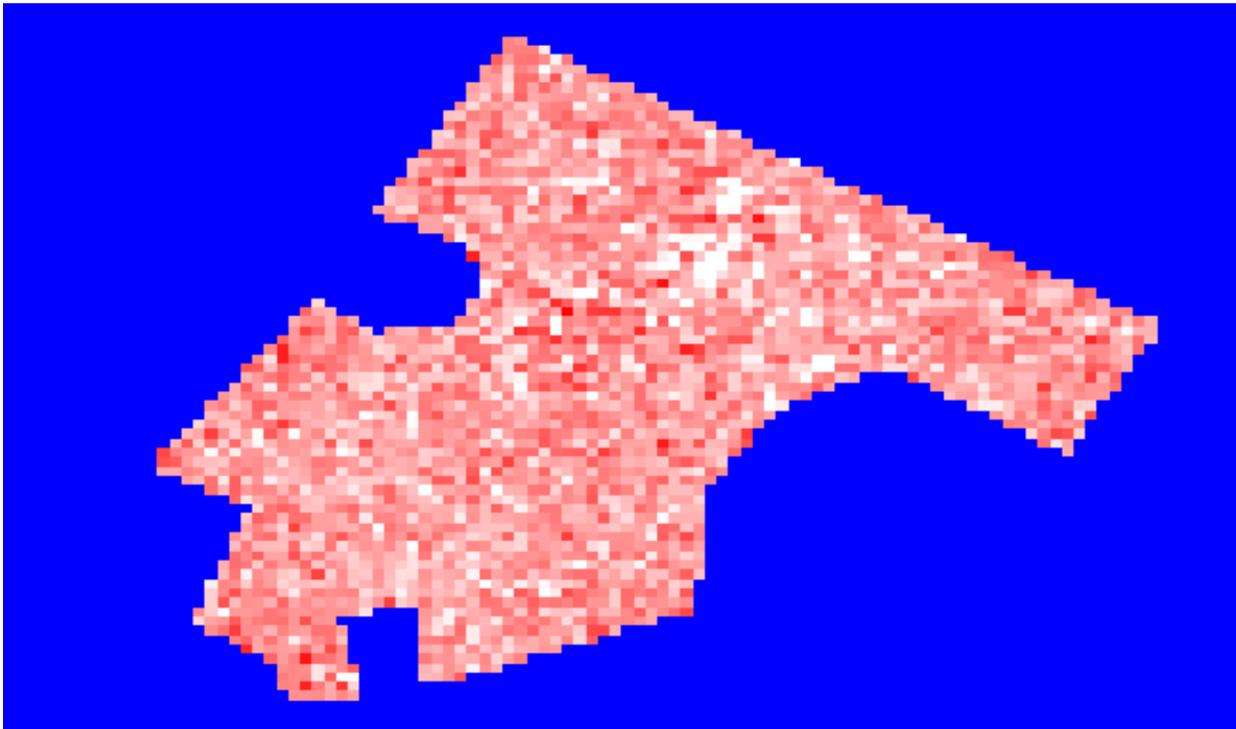


Figure 4-50. MPE microscopic mixture proportions. Darker red pixels indicate higher estimated proportions.

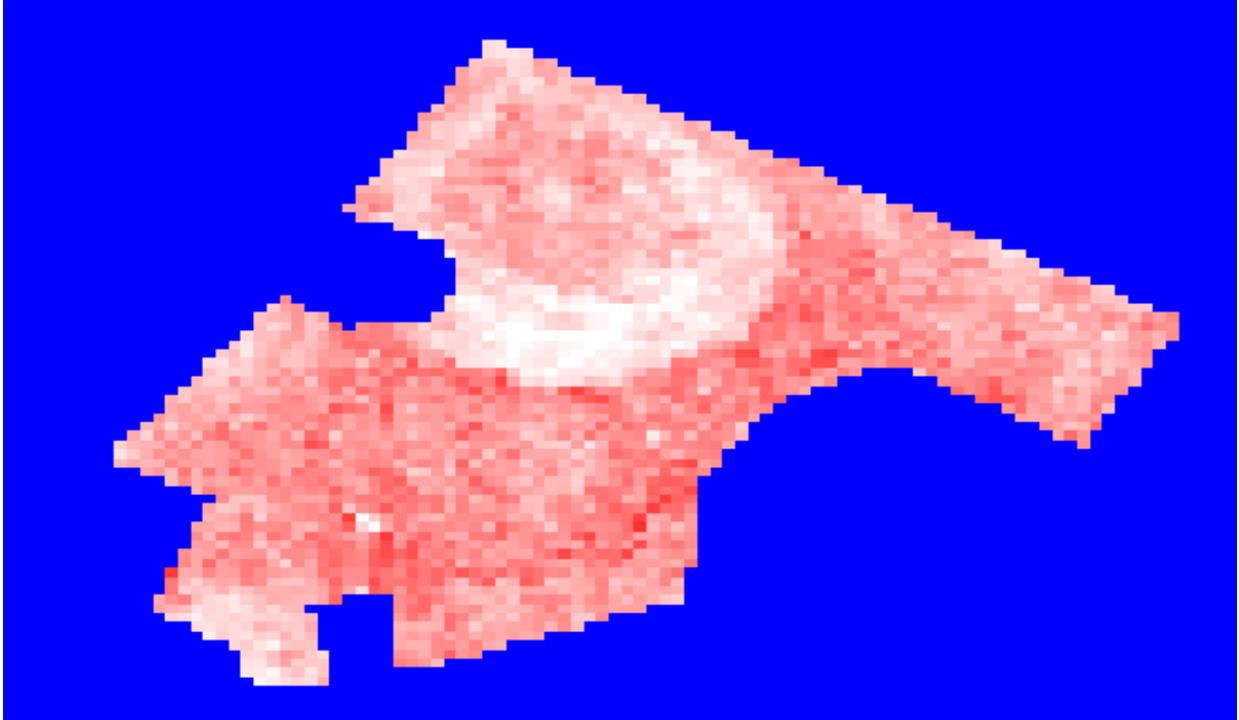


Figure 4-51. MPE grass macroscopic proportions. Darker red pixels indicate higher estimated proportions.

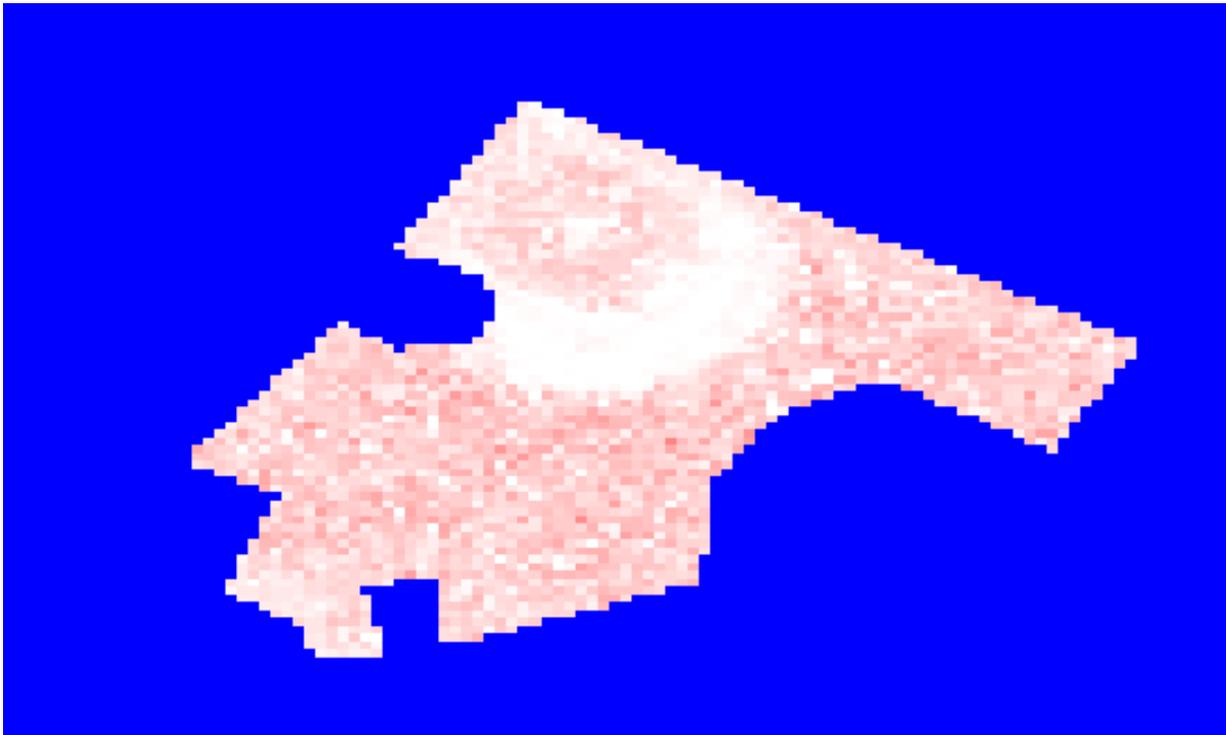


Figure 4-52. MPE grass microscopic proportions. Darker red pixels indicate higher estimated proportions.

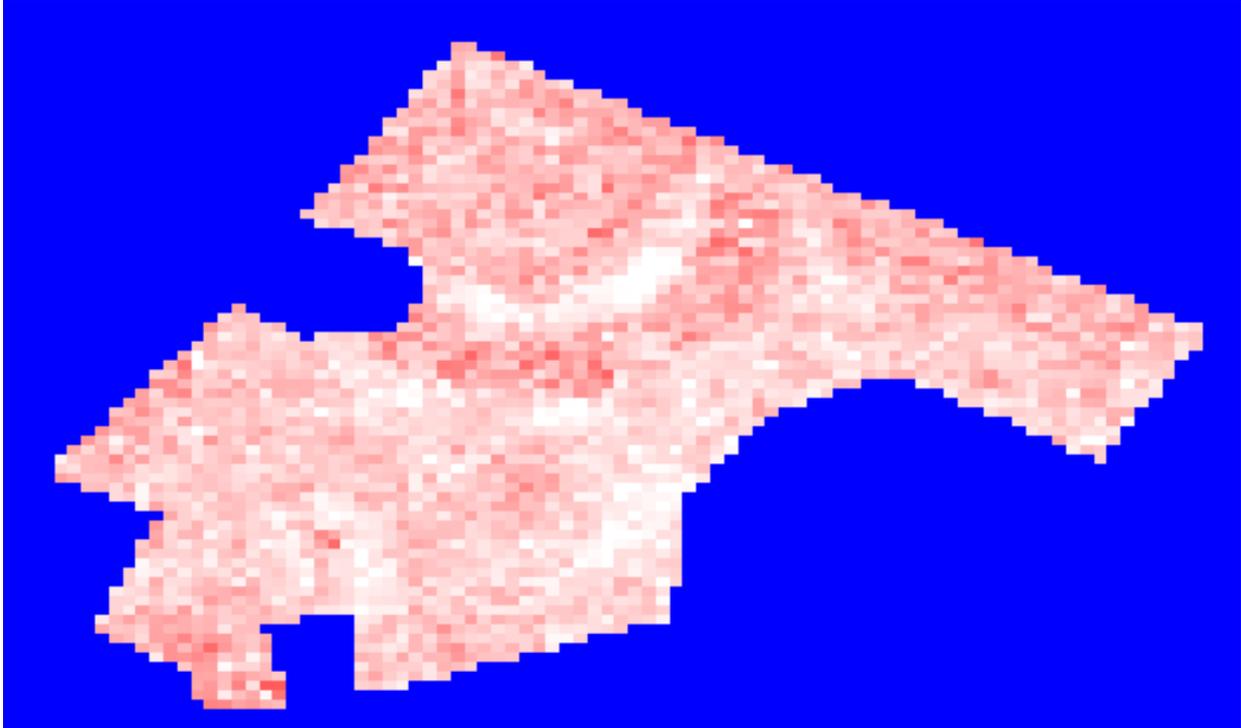


Figure 4-53. MPE dirt macroscopic proportions. Darker red pixels indicate higher estimated proportions.

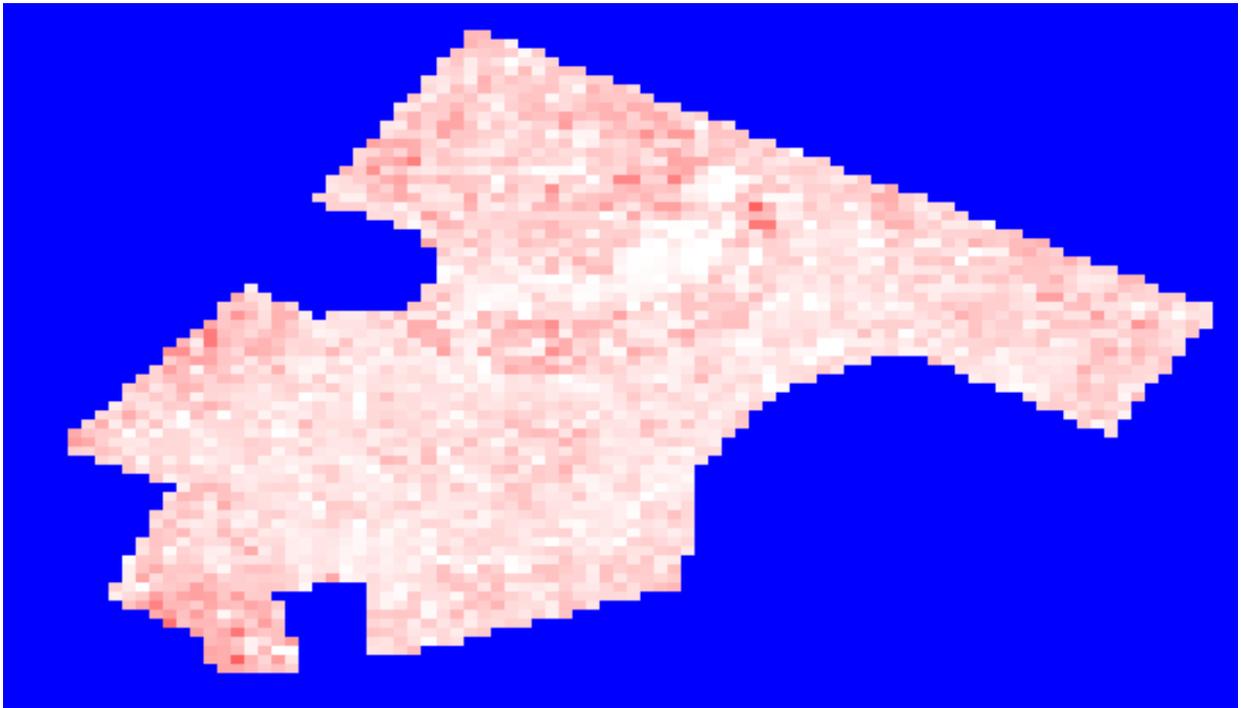


Figure 4-54. MPE dirt microscopic proportions. Darker red pixels indicate higher estimated proportions.

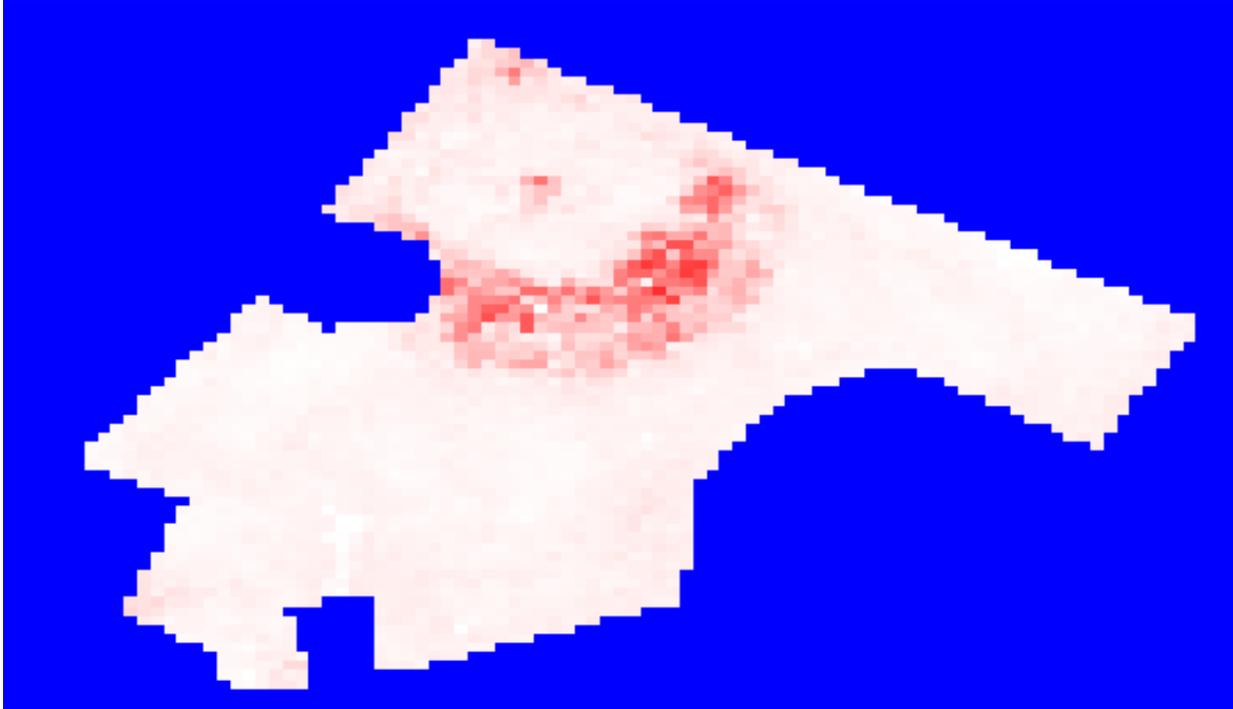


Figure 4-55. MPE clay macroscopic proportions. Darker red pixels indicate higher estimated proportions.

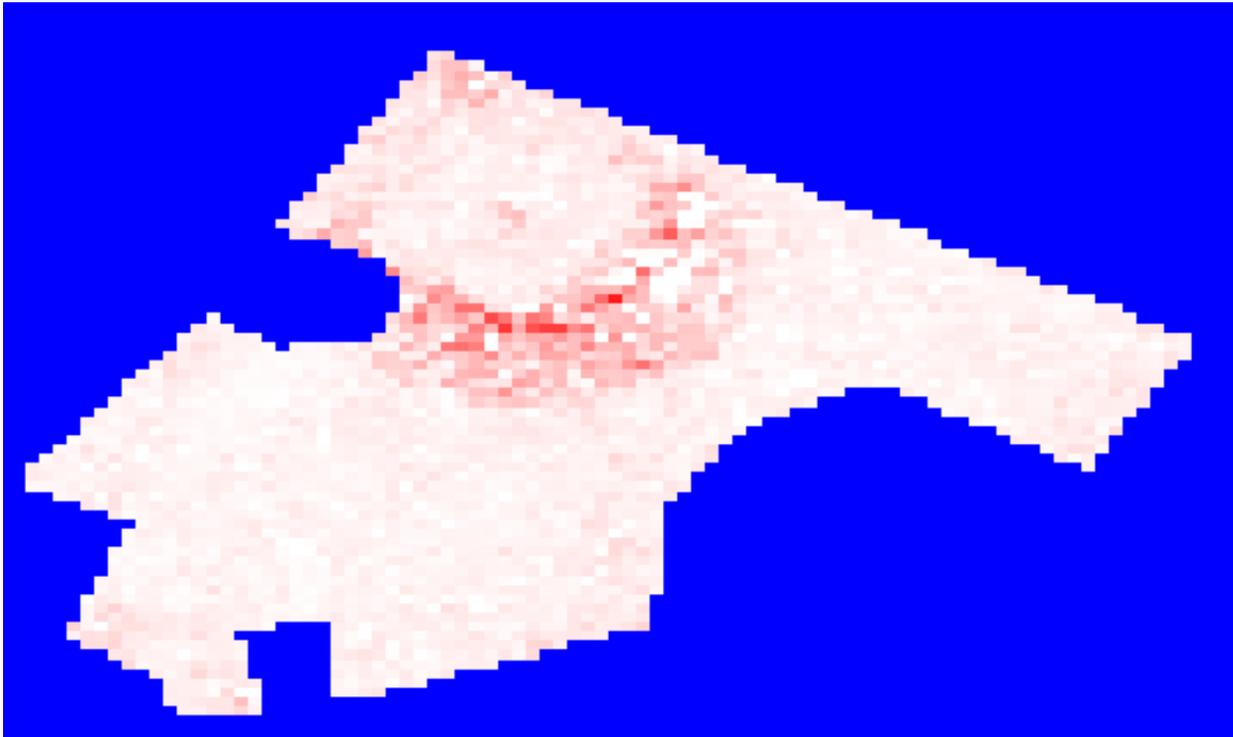


Figure 4-56. MPE clay microscopic proportions. Darker red pixels indicate higher estimated proportions.



Figure 4-57. Beach scene.

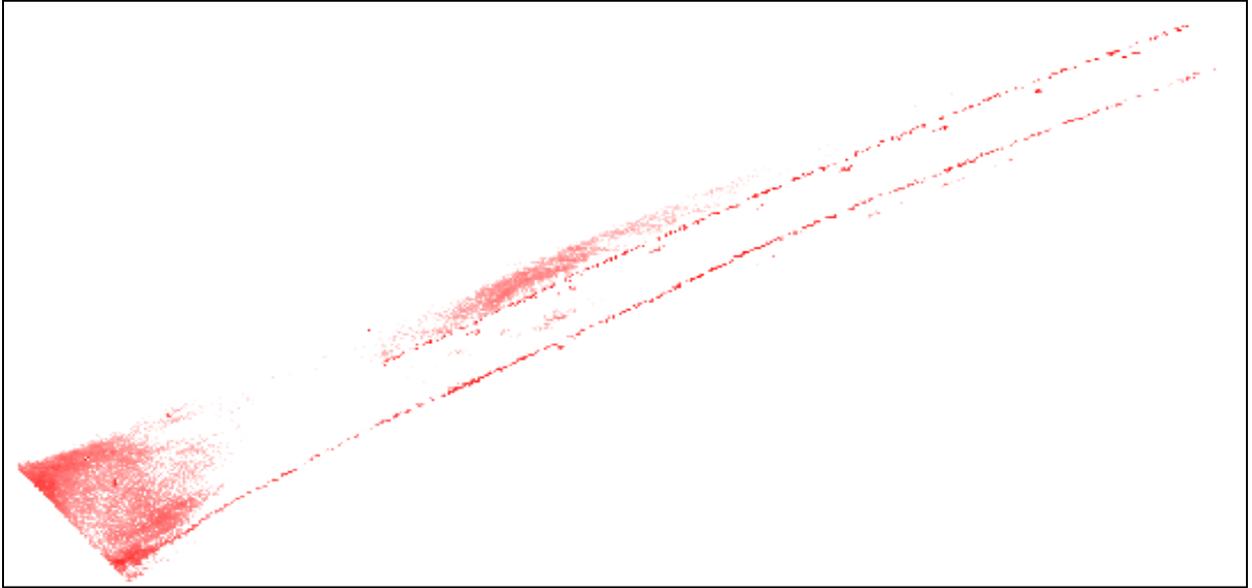


Figure 4-58. Microscopic proportions estimated using MPE. Darker red pixels indicate higher estimated proportions.

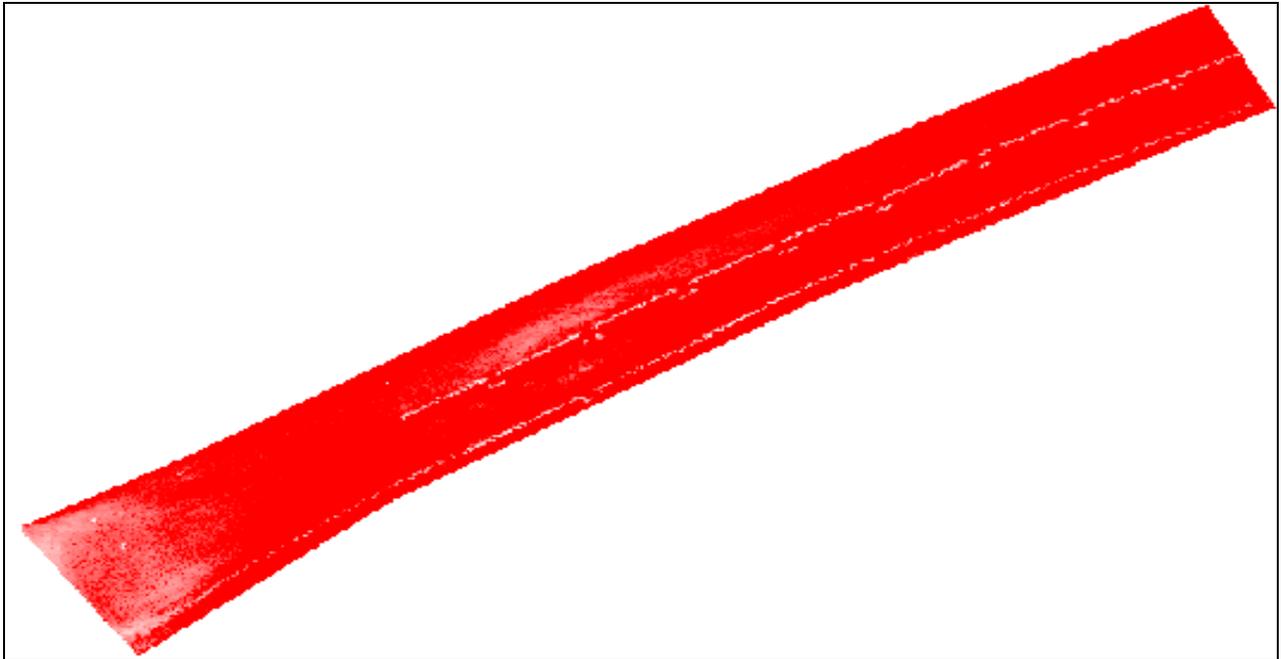


Figure 4-59. Macroscopic proportion map for sand endmember. Darker red pixels indicate higher estimated proportions.

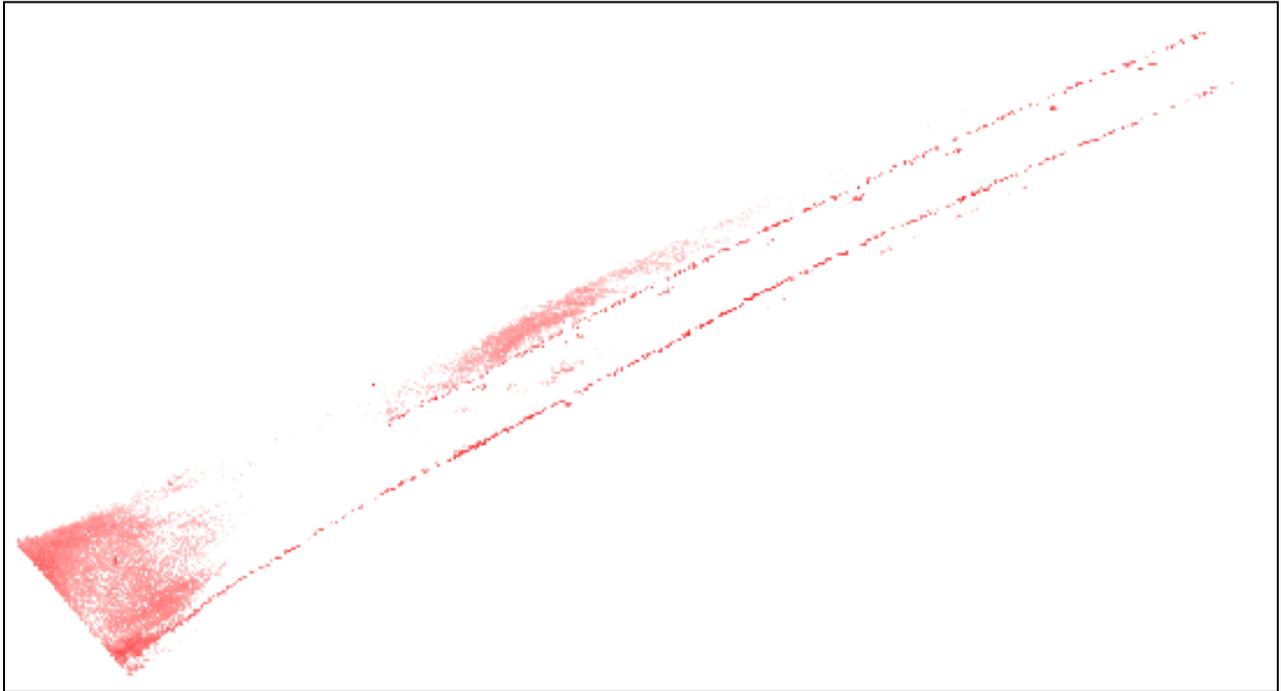


Figure 4-60. Microscopic proportion map for sand endmember. Darker red pixels indicate higher estimated proportions.

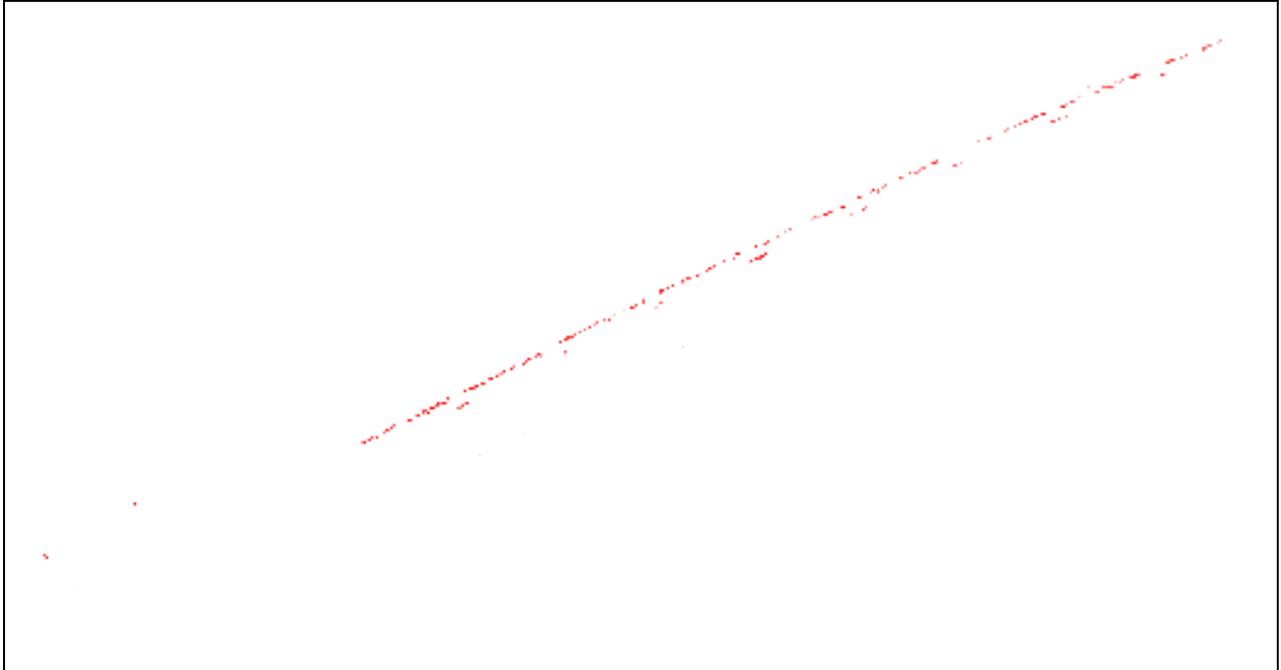


Figure 4-61. Macroscopic proportion map for sediment endmember. Darker red pixels indicate higher estimated proportions.

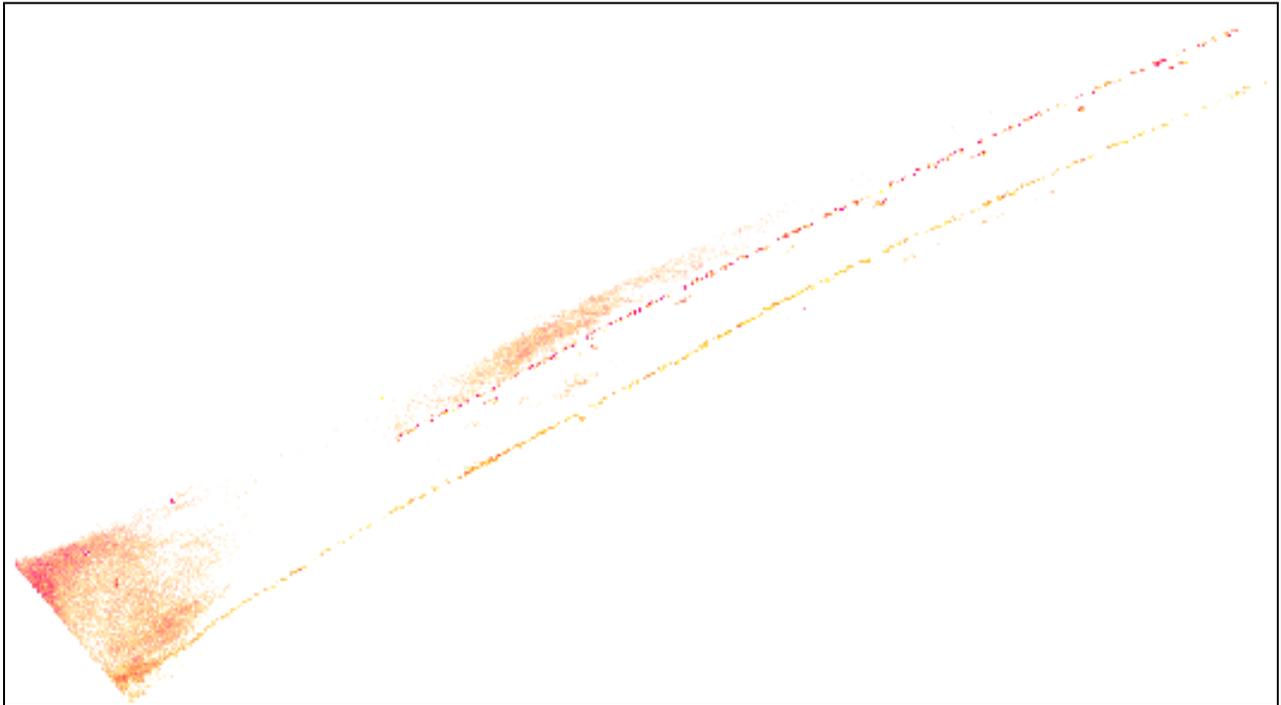


Figure 4-62. Microscopic proportion map for sediment endmember. Darker red pixels indicate higher estimated proportions.

CHAPTER 5 CONCLUSION

Two methods of incorporating macroscopic and microscopic mixture models into hyperspectral pixel unmixing is presented and discussed. A vast majority of hyperspectral unmixing methods rely on the linear mixture model to describe pixel spectra resulting from mixtures of endmembers. [1-4] Methods exist to unmix hyperspectral pixels using nonlinear models, but rely on severely limiting assumptions or estimations of the nonlinearity. [1, 23, 24, 32, 35, 37] The unmixing methods presented in this document utilize the bidirectional reflectance distribution function to model microscopic mixtures. Using this model, along with the linear mixture model to incorporate macroscopic mixtures, these methods are able to accurately unmix hyperspectral images composed of both macroscopic and microscopic mixtures. The mixtures are estimated directly from the hyperspectral data without the need for *a priori* knowledge of the mixture types. Quantitative results are presented using synthetic data sets, of macroscopic and microscopic mixtures, to demonstrate the increased accuracy in unmixing using these new physics-based methods over linear methods. In addition, results are presented using a well-known laboratory data set. Using these results, and other published results from this data set, increased accuracy in unmixing over other nonlinear methods is shown. Qualitative results are presented using two different hyperspectral image scenes collected from an airborne platform.

The first method introduced is the DME algorithm. This algorithm explicitly uses the macroscopic and microscopic mixture models for estimating endmembers and their proportions. Inclusion of these mixture models allows DME to unmix hyperspectral data in the presence of both macroscopic and microscopic mixtures. Quantitative

experiments conducted on both synthetic and laboratory data indicate that DME is able to estimate endmembers and proportions with increased accuracy over linear models, when both mixture types are present. Additionally, experiments on laboratory data indicate that DME estimates proportions of microscopically mixed data with more accuracy than existing methods for unmixing microscopic mixture data.

A new model for hyperspectral image pixels is introduced. This model, the MMP, models a pixel as a mixture of mixtures. Specifically the MMP describes a hyperspectral pixel as a macroscopic mixture of endmembers and a microscopic mixture. A new algorithm was designed around the MMP model, the MPE algorithm. Experiments utilizing the synthetic and laboratory data sets led to two conclusions. The first is that MPE is able to accurately estimate endmembers and proportions of MMP data sets as well as data sets formed of macroscopically and microscopically mixed only pixels. Secondly, in some cases MPE is able to estimate proportions of laboratory 100% microscopically mixed minerals more accurately than traditional microscopic unmixing methods.

During the course of this research, many areas of future work became apparent. The first area of possible future work is to more accurately estimate the angles of incidence and emergence in an aerial hyperspectral collection. An approach to be investigated is to use light detection and ranging (LIDAR) fused with the hyperspectral data to establish the geometry of the scattering surface to the light source and detector. The LIDAR provides 3-dimensional spatial data that can be used to determine the attitude of the scattering surface. This extracted information, combined with metadata produced by the sensor, would allow for estimation of the surface's orientation with

respect to the sensor platform. Increased accuracy in estimating the angles of incidence and emergence could result in increased accuracies in estimating endmembers and proportions of the collected data.

Another area of further research could be in endmember estimation. Endmember estimation using DME and MPE is effective but slow in comparison to other geometric methods, which only account for macroscopic mixtures. Further research could look into using a parametric manifold based on the bidirectional reflectance distribution function to estimate endmembers. This type of approach to endmember estimation could allow for the continued accuracy of endmember estimation shown with DME and MPE but with increased estimation speed. Also, the current models rely on the number of endmembers to be given as an input parameter. Adapting DME and MPE to use a Bayesian sparsity promoting prior, to mimic a SPICE framework, could allow the algorithms to estimate the number of endmembers autonomously. [4] Additionally, experiments could be run to further test the robustness of these methods to increased number of endmembers in the hyperspectral mixtures.

A third area of follow-on research could be to include multiple reflections and transmissions into the endmember and proportion estimation process. Thus, allowing the algorithms to account for another common mixture type. [14, 16, 19] The virtual endmember concept could be included into DME and MPE to allow microscopic mixtures between endmembers and virtual endmembers caused by multiple reflections and transmission between surfaces. [14, 16, 18, 19]

Experiments on MPE indicate increased accuracy over existing methods when estimating hyperspectral data composed of MMPs. However, this document discusses

the inherent introduction of error by the ill-posed inversion problem of estimating the microscopic proportions. Future research could look into methods of decreasing the error in estimating these proportions. One such method could be the use of sampling to allow for simultaneous estimation of the macroscopic and microscopic proportions. This simultaneous estimation could result in greater accuracy in estimating proportions. Another method could be to use spatial data inherent in hyperspectral images. By using spatial information and the assumption that mixtures proportions are similar in spatially close pixels, the microscopic proportions may be estimated with increased accuracy.

This research utilizes two laboratory data sets and two airborne hyperspectral data collections. However, the lack of real-world collection data necessitated the use of synthetic data sets. Future work should collect additional real-world data sets of a variety of endmembers and collecting conditions. These additional data sets will allow for more experiments on the existing models but also further understanding of how the bidirectional reflectance distribution function impacts data unbeknownst to researchers unfamiliar with reflectance spectroscopy. Also, collection of data under differing conditions will allow for the inclusion of different reflectance models, e.g., a direction-hemispherical reflectance distribution function.

Finally, additional research could incorporate non-Gaussian noise models for both reflectance-domain and albedo-domain models. Research presented in this document uses Gaussian noise assumptions for both the reflectance-domain and albedo-domain models, as is commonly accepted in hyperspectral research. [1, 3, 32] However, noise models that more accurately reflect the noise in the data could lead to increased accuracies in estimating endmembers and proportions.

LIST OF REFERENCES

- [1] N. Keshava and J. F. Mustard, "Spectral unmixing," *Signal Processing Magazine, IEEE*, vol. 19, pp. 44-57, 2002.
- [2] D. Manolakis, D. Marden, and G. A. Shaw, "Hyperspectral Image Processing for Automatic Target Detection Applications," *Lincoln Laboratory Journal*, vol. 14, pp. 79-116, 2003.
- [3] M. Berman, H. Kiiveri, R. Lagerstrom, A. Ernst, R. Dunne, and J. F. Huntington, "ICE: a statistical approach to identifying endmembers in hyperspectral images," *Geoscience and Remote Sensing, IEEE Transactions on*, vol. 42, pp. 2085-2095, 2004.
- [4] A. Zare and P. Gader, "Sparsity Promoting Iterated Constrained Endmember Detection in Hyperspectral Imagery," *Geoscience and Remote Sensing Letters, IEEE*, vol. 4, pp. 446-450, 2007.
- [5] A. Zare and P. Gader, "Sparsity promoting iterated constrained endmember detection with integrated band selection," in *Geoscience and Remote Sensing Symposium, 2007. IGARSS 2007. IEEE International*, 2007, pp. 4045-4048.
- [6] A. Zare and P. Gader, "PCE: Piecewise Convex Endmember Detection," *Geoscience and Remote Sensing, IEEE Transactions on*, vol. 48, pp. 2620-2632, 2010.
- [7] B. Hapke, *Theory of Reflectance and Emittance Spectroscopy*. Cambridge University Press, 1993.
- [8] C. Xuehong, C. Jin, J. Xiuping, and W. Jin, "Impact of collinearity on linear and nonlinear spectral mixture analysis," in *Hyperspectral Image and Signal Processing: Evolution in Remote Sensing (WHISPERS), 2010 2nd Workshop on*, 2010, pp. 1-4.
- [9] W. Fan, B. Hu, J. Miller, and M. Li, "Comparative Study Between a New Nonlinear Model and Common Linear Model for Analysing Laboratory Simulated-Forest Hyperspectral Data," *International Journal of Remote Sensing*, vol. 30, pp. 2951-2962, June 10, 2009.
- [10] N. Raksuntorn and D. Qian, "Nonlinear mixture analysis for hyperspectral imagery," in *Geoscience and Remote Sensing Symposium, 2009 IEEE International, IGARSS 2009*, 2009, pp. III-829-III-832.
- [11] X. Chen and L. Vierling, "Spectral mixture analyses of hyperspectral data acquired using a tethered balloon," *Remote Sensing of Environment*, vol. 103, pp. 338-350, 2006.

- [12] N. Raksuntorn and D. Qian, "Nonlinear Spectral Mixture Analysis for Hyperspectral Imagery in an Unknown Environment," *Geoscience and Remote Sensing Letters, IEEE*, vol. 7, pp. 836-840, 2010.
- [13] A. Halimi, Y. Altmann, N. Dobigeon, and J. Y. Tourneret, "Nonlinear Unmixing of Hyperspectral Images Using a Generalized Bilinear Model," *Geoscience and Remote Sensing, IEEE Transactions on*, vol. PP, pp. 1-10, 2011.
- [14] T. W. Ray and B. C. Murray, "Nonlinear spectral mixing in desert vegetation," *Remote Sensing of Environment*, vol. 55, pp. 59-64, 1996.
- [15] B. Somers, K. Cools, S. Delalieux, J. Stuckens, D. Van der Zande, W. W. Verstraeten, and P. Coppin, "Nonlinear Hyperspectral Mixture Analysis for tree cover estimates in orchards," *Remote Sensing of Environment*, vol. 113, pp. 1183-1193, 2009.
- [16] T. Han and D. G. Goodenough, "Investigation of Nonlinearity in Hyperspectral Imagery Using Surrogate Data Methods," *Geoscience and Remote Sensing, IEEE Transactions on*, vol. 46, pp. 2840-2847, 2008.
- [17] P. V. Villeneuve, S. A. Gerstl, and G. P. Asner, "Estimating nonlinear mixing effects for arid vegetation scenes with MISR channels and observation directions," in *Geoscience and Remote Sensing Symposium Proceedings, 1998. IGARSS '98. 1998 IEEE International*, 1998, pp. 1234-1236 vol.3.
- [18] H. Baoxin, J. R. Miller, W. Jinnian, and N. S. Goel, "Investigation of linear spectral mixtures of the reflectance spectra using laboratory simulated forest scenes," in *Geoscience and Remote Sensing Symposium, 2002. IGARSS '02. 2002 IEEE International*, 2002, pp. 1535-1537 vol.3.
- [19] C. C. Borel and S. A. W. Gerstl, "Nonlinear spectral mixing models for vegetative and soil surfaces," *Remote Sensing of Environment*, vol. 47, pp. 403-416, 1994.
- [20] R. B. Singer and T. B. McCord, "Mars: Large scale mixing of bright and dark surface materials and implications for analysis of spectral reflectance," *Proc. Lunar Planet. Sci. Conf. 10th*, pp. 1835-1848, 1979.
- [21] D. B. Nash and J. E. Conel, "Spectral Reflectance Systematics for Mixtures of Powdered Hypersthene, Labradorite, and Ilmenite," *Journal of Geophysical Research*, vol. 79, pp. 1615-1621, April 10, 1974.
- [22] J. F. Mustard and C. M. Pieters, "Photometric Phase Functions of Common Geologic Minerals and Applications to Quantitative Analysis of Mineral Mixture Reflectance Spectra," *Journal of Geophysical Research*, vol. 94, pp. 13619-13634, October 10, 1989.

- [23] J. Broadwater and A. Banerjee, "A comparison of kernel functions for intimate mixture models," in *Hyperspectral Image and Signal Processing: Evolution in Remote Sensing, 2009. WHISPERS '09. First Workshop on*, 2009, pp. 1-4.
- [24] J. Broadwater and A. Banerjee, "A generalized kernel for areal and intimate mixtures," in *Hyperspectral Image and Signal Processing: Evolution in Remote Sensing (WHISPERS), 2010 2nd Workshop on*, 2010, pp. 1-4.
- [25] J. Broadwater and A. Banerjee, "Mapping Intimate Mixtures Using An Adaptive Kernel-Based Technique," presented at the Workshop on Hyperspectral Image and Signal Processing: Evolution in Remote Sensing, Lisbon, Portugal, 2011.
- [26] P. E. Johnson, M. O. Smith, and J. B. Adams, "Quantitative Analysis of Planetary Reflectance Spectra with Principal Components Analysis," *Journal of Geophysical Research*, vol. 90, pp. C805-C810, February 15, 1985.
- [27] J. M. P. Nascimento and J. M. Bioucas-Dias, "Unmixing Hyperspectral Intimate Mixtures," in *SPIE Image and Signal Processing for Remote Sensing XVI*, 2010.
- [28] M. T. Rahman and M. S. Alam, "Nonlinear Unmixing of Hyperspectral Data Using BDRF and Maximum Likelihood Algorithm," in *SPIE Automatic Target Recognition XVII*, 2007.
- [29] M. O. Smith, P. E. Johnson, and J. B. Adams, "Quantitative Determination of Mineral Types and Abundances from Reflectance Spectra Using Principal Components Analysis," *Journal of Geophysical Research*, vol. 90, pp. C797-C804, February 15, 1985.
- [30] B. Hapke, "Bidirectional Reflectance Spectroscopy 1. Theory," *Journal of Geophysical Research*, vol. 86, pp. 3039-3054, April 10, 1981.
- [31] B. Hapke and E. Wells, "Bidirectional Reflectance Spectroscopy 2. Experiments and Observations," *Journal of Geophysical Research*, vol. 86, pp. 3055-3060, April 10, 1981.
- [32] J. F. Mustard and C. M. Pieters, "Quantitative Abundance Estimates From Bidirectional Reflectance Measurements," *Journal of Geophysical Research*, vol. 92, pp. E617-E626, March 30, 1987.
- [33] F. Poulet and S. Erard, "Nonlinear spectral mixing: Quantitative analysis of laboratory mineral mixtures," *J. Geophys. Res.*, vol. 109, p. E02009, 2004.
- [34] Y. Shkuratov, L. Starukhina, H. Hoffmann, and G. Arnold, "A Model of Spectral Albedo of Particulate Surfaces: Implications for Optical Properties of the Moon," *Icarus*, vol. 137, pp. 235-246, 1999.

- [35] K. J. Guilfoyle, M. L. Althouse, and I. C. Chein, "A quantitative and comparative analysis of linear and nonlinear spectral mixture models using radial basis function neural networks," *Geoscience and Remote Sensing, IEEE Transactions on*, vol. 39, pp. 2314-2318, 2001.
- [36] G. A. Licciardi, "Neural Network Algorithms for Nonlinear Spectral Unmixing Applied on Hyperspectral Data," presented at the Hyperspectral 2010 Workshop, Frascati, Italy, 2010.
- [37] J. Plaza, P. Martinez, R. Perez, and A. Plaza, "Nonlinear Neural Network Mixture Models for Fractional Abundance Estimation in AVIRIS Hyperspectral Images," presented at the NASA Jet Propulsion Laboratory AVIRIS Airborne Earth Science Workshop, Pasadena, California, 2004.
- [38] J. Plaza, A. Plaza, R. Perez, and P. Martinez, "Joint linear/nonlinear spectral unmixing of hyperspectral image data," in *Geoscience and Remote Sensing Symposium, 2007. IGARSS 2007. IEEE International*, 2007, pp. 4037-4040.
- [39] A. Banerjee, P. Burlina, and J. Broadwater, "A machine learning approach for finding hyperspectral endmembers," in *Geoscience and Remote Sensing Symposium, 2007. IGARSS 2007. IEEE International*, 2007, pp. 3817-3820.
- [40] J. Broadwater, R. Chellappa, A. Banerjee, and P. Burlina, "Kernel fully constrained least squares abundance estimates," in *Geoscience and Remote Sensing Symposium, 2007. IGARSS 2007. IEEE International*, 2007, pp. 4041-4044.
- [41] B. Wu, L. Zhang, P. Li, and J. Zhang, "Nonlinear Estimation of Hyperspectral Mixture Pixel Proportion Based on Kernel Orthogonal Subspace Projection," in *Advances in Neural Networks - ISNN 2006*. vol. 3971, J. Wang, Z. Yi, J. Zurada, B.-L. Lu, and H. Yin, Eds., ed: Springer Berlin / Heidelberg, 2006, pp. 1070-1075.
- [42] R. Heylen, D. Burazerovic, and P. Scheunders, "A graph-based method for non-linear unmixing of hyperspectral imagery," in *Geoscience and Remote Sensing Symposium (IGARSS), 2010 IEEE International*, 2010, pp. 197-200.
- [43] R. Heylen, D. Burazerovic, and P. Scheunders, "Non-linear Spectral Unmixing by Geodesic Simplex Volume Maximization," *Selected Topics in Signal Processing, IEEE Journal of*, vol. PP, pp. 1-1, 2010.
- [44] R. Heylen and P. Scheunders, "Nonlinear barycentric dimensionality reduction," in *Image Processing (ICIP), 2010 17th IEEE International Conference on*, 2010, pp. 1341-1344.
- [45] N. Dobigeon, S. Moussaoui, J.-Y. Tourneret, and C. Carteret, "Bayesian separation of spectral sources under non-negativity and full additivity constraints," *Signal Processing*, vol. 89, pp. 2657-2669, 2009.

- [46] O. Eches, N. Dobigeon, and J. Y. Tourneret, "An NCM-based Bayesian algorithm for hyperspectral unmixing," in *Hyperspectral Image and Signal Processing: Evolution in Remote Sensing, 2009. WHISPERS '09. First Workshop on*, 2009, pp. 1-4.
- [47] J. Nascimento and J. M. Bioucas-Dias, "Learning dependent sources using mixtures of Dirichlet: Applications on hyperspectral unmixing," in *Hyperspectral Image and Signal Processing: Evolution in Remote Sensing, 2009. WHISPERS '09. First Workshop on*, 2009, pp. 1-5.
- [48] A. Zare, "Hyperspectral Endmember Detection and Band Selection Using Bayesian Methods," Ph.D. Dissertation, Computer & Information Science & Engineering, University of Florida, Gainesville, 2008.
- [49] A. Zare and P. Gader, "L1-Endmembers: A Robust Endmember Detection and Spectral Unmixing Algorithm," presented at the Proceedings of the SPIE Defense, Security, and Sensing, Orlando, Florida, 2010.
- [50] A. Zare and P. D. Gader, "Endmember detection using the Dirichlet process," in *Pattern Recognition, 2008. ICPR 2008. 19th International Conference on*, 2008, pp. 1-4.
- [51] J. M. Bioucas-Dias, "A variable splitting augmented Lagrangian approach to linear spectral unmixing," in *Hyperspectral Image and Signal Processing: Evolution in Remote Sensing, 2009. WHISPERS '09. First Workshop on*, 2009, pp. 1-4.
- [52] J. W. Boardman, "Automating spectral unmixing of AVIRIS data using convex geometry concepts," *Summaries of the Fourth Annual JPL Airborne Geoscience Workshop, JPL Pub. 93-26, AVIRIS Workshop*, vol. 1, pp. 11-14, 1993.
- [53] J. W. Boardman, F. A. Kruse, and R. O. Green, "Mapping Target Signatures Via Partial Unmixing of AVIRIS Data," *Summaries, Fifth JPL Airborne Earth Science Workshop, JPL Publications*, vol. 1, pp. 23-26, 1995.
- [54] J. M. P. Nascimento and J. M. B. Dias, "Vertex component analysis: a fast algorithm to unmix hyperspectral data," *Geoscience and Remote Sensing, IEEE Transactions on*, vol. 43, pp. 898-910, 2005.
- [55] A. Santos-Garcia and M. Velez-Reyes, "Identifiability of geometric models for linear unmixing at different spatial resolutions in hyperspectral unmixing," in *Hyperspectral Image and Signal Processing: Evolution in Remote Sensing (WHISPERS), 2010 2nd Workshop on*, 2010, pp. 1-4.
- [56] C. Tsung-Han, M. Wing-Kin, C. Chong-Yung, and A. ArulMurugan, "Hyperspectral unmixing from a convex analysis and optimization perspective," in *Hyperspectral Image and Signal Processing: Evolution in Remote Sensing, 2009. WHISPERS '09. First Workshop on*, 2009, pp. 1-4.

- [57] M. E. Winter, "N-FINDR: An Algorithm for Fast Autonomous Spectral End-member Determination in Hyperspectral Data," in *SPIE Conference on Imaging Spectrometry V*, 1999, pp. 266-275.
- [58] J. Xiaoli, D. Yingzi, and I. C. Chein, "Component analysis-based unsupervised linear spectral mixture analysis for hyperspectral imagery," in *Hyperspectral Image and Signal Processing: Evolution in Remote Sensing, 2009. WHISPERS '09. First Workshop on*, 2009, pp. 1-5.
- [59] T. L. Ainsworth, C. M. Bachmann, and R. A. Fusina, "Local intrinsic dimensionality of hyperspectral imagery from non-linear manifold coordinates," in *Geoscience and Remote Sensing Symposium, 2007. IGARSS 2007. IEEE International*, 2007, pp. 1541-1542.
- [60] C. M. Bachmann, T. L. Ainsworth, and R. A. Fusina, "Automated Estimation of Spectral Neighborhood Size in Manifold Coordinate Representations of Hyperspectral Imagery: Implications for Anomaly Finding, Bathymetry Retrieval, and Land Applications," in *Geoscience and Remote Sensing Symposium, 2008. IGARSS 2008. IEEE International*, 2008, pp. I-56-I-57.
- [61] G. Dong, Y. Zhang, and S. Ji, "Dimensionality Reduction of Hyperspectral Data Based on ISOMAP Algorithm," in *Electronic Measurement and Instruments, 2007. ICEMI '07. 8th International Conference on*, 2007, pp. 3-935-3-938.
- [62] W. Jinhuan, T. Zheng, S. Hongwei, and Y. Weidong, "Feature extraction of hyperspectral images based on preserving neighborhood discriminant embedding," in *Image Analysis and Signal Processing (IASP), 2010 International Conference on*, 2010, pp. 257-262.
- [63] K. Karantzas, "Intrinsic dimensionality estimation and dimensionality reduction through scale space filtering," in *Digital Signal Processing, 2009 16th International Conference on*, 2009, pp. 1-6.
- [64] O. Kuybeda, D. Malah, and M. Barzohar, "Anomaly Preserving ℓ_2 -Optimal Dimensionality Reduction Over a Grassmann Manifold," *Signal Processing, IEEE Transactions on*, vol. 58, pp. 544-552, 2010.
- [65] M. Li, M. M. Crawford, and T. Jinwen, "Anomaly detection for hyperspectral images using local tangent space alignment," in *Geoscience and Remote Sensing Symposium (IGARSS), 2010 IEEE International*, 2010, pp. 824-827.
- [66] C. Ling, H. Rui, and H. Wei, "Graph-based semi-supervised weighted band selection for classification of hyperspectral data," in *Audio Language and Image Processing (ICALIP), 2010 International Conference on*, 2010, pp. 1123-1126.

- [67] E. Merenyi, B. Csatho, and K. Tasdemir, "Knowledge discovery in urban environments from fused multi-dimensional imagery," in *Urban Remote Sensing Joint Event, 2007*, 2007, pp. 1-13.
- [68] S. Velasco-Forero, J. Angulo, and J. Chanussot, "Morphological image distances for hyperspectral dimensionality exploration using Kernel-PCA and ISOMAP," in *Geoscience and Remote Sensing Symposium, 2009 IEEE International, IGARSS 2009*, 2009, pp. III-109-III-112.
- [69] S. Weiwei and L. Chun, "Manifold Coordinates Repairing of Boundary Points with PLS for Isomap Nonlinear Dimensionality Reduction of Hyperspectral Image," in *Multi-Platform/Multi-Sensor Remote Sensing and Mapping (M2RSM), 2011 International Workshop on*, 2011, pp. 1-6.
- [70] Z. Yuan, W. Bo, L. Deren, and L. Rongxing, "Edge detection on hyperspectral imagery via Manifold techniques," in *Hyperspectral Image and Signal Processing: Evolution in Remote Sensing, 2009. WHISPERS '09. First Workshop on*, 2009, pp. 1-4.
- [71] K. Cawse, M. Sears, A. Robin, S. B. Damelin, K. Wessels, F. van den Bergh, and R. Mathieu, "Using Random Matrix Theory to determine the number of endmembers in a hyperspectral image," in *Hyperspectral Image and Signal Processing: Evolution in Remote Sensing (WHISPERS), 2010 2nd Workshop on*, 2010, pp. 1-4.
- [72] J. Broadwater and A. Banerjee, "A Neyman-Pearson approach to estimating the number of endmembers," in *Geoscience and Remote Sensing Symposium, 2009 IEEE International, IGARSS 2009*, 2009, pp. IV-693-IV-696.
- [73] J. Broadwater, "Effects of Endmember Dimensionality on Subpixel Detection Performance," in *Geoscience and Remote Sensing Symposium, 2008. IGARSS 2008. IEEE International*, 2008, pp. II-613-II-616.
- [74] M. D. Iordache, A. Plaza, and J. Bioucas-Dias, "On the use of spectral libraries to perform sparse unmixing of hyperspectral data," in *Hyperspectral Image and Signal Processing: Evolution in Remote Sensing (WHISPERS), 2010 2nd Workshop on*, 2010, pp. 1-4.
- [75] A. Zare, J. Bolton, P. Gader, and M. Schatten, "Vegetation Mapping for Landmine Detection Using Long-Wave Hyperspectral Imagery," *Geoscience and Remote Sensing, IEEE Transactions on*, vol. 46, pp. 172-178, 2008.
- [76] I. Gerg, "An evaluation of three endmember extraction algorithms: ATGP, ICA-EEA & VCA," in *Hyperspectral Image and Signal Processing: Evolution in Remote Sensing (WHISPERS), 2010 2nd Workshop on*, 2010, pp. 1-4.
- [77] J. M. Bioucas-Dias and A. Plaza, "Hyperspectral unmixing: geometrical, statistical, and sparse regression-based approaches," 2010, p. 78300A.

- [78] M. Parente and A. Plaza, "Survey of geometric and statistical unmixing algorithms for hyperspectral images," in *Hyperspectral Image and Signal Processing: Evolution in Remote Sensing (WHISPERS), 2010 2nd Workshop on*, 2010, pp. 1-4.
- [79] A. Zare, O. Bchir, H. Frigui, and P. Gader, "Piece-wise Convex Multiple Model Endmember Detection," *Submitted to IEEE Transactions on Geoscience and Remote Sensing, Under Review*.
- [80] A. Zare, O. Bchir, H. Frigui, and P. Gader, "Spatially-smooth piece-wise convex endmember detection," in *Hyperspectral Image and Signal Processing: Evolution in Remote Sensing (WHISPERS), 2010 2nd Workshop on*, 2010, pp. 1-4.
- [81] A. Zare, O. Bchir, H. Frigui, and P. Gader, "A comparison of deterministic and probabilistic approaches to endmember representation," in *Hyperspectral Image and Signal Processing: Evolution in Remote Sensing (WHISPERS), 2010 2nd Workshop on*, 2010, pp. 1-4.
- [82] A. Zare and P. Gader, "Context-based endmember detection for hyperspectral imagery," in *Hyperspectral Image and Signal Processing: Evolution in Remote Sensing, 2009. WHISPERS '09. First Workshop on*, 2009, pp. 1-4.
- [83] O. Eches, N. Dobigeon, and J. Y. Tourneret, "Markov random fields for joint unmixing and segmentation of hyperspectral images," in *Hyperspectral Image and Signal Processing: Evolution in Remote Sensing (WHISPERS), 2010 2nd Workshop on*, 2010, pp. 1-4.
- [84] A. Huck and M. Guillaume, "Robust hyperspectral data unmixing with spatial and spectral regularized NMF," in *Hyperspectral Image and Signal Processing: Evolution in Remote Sensing (WHISPERS), 2010 2nd Workshop on*, 2010, pp. 1-4.
- [85] Marti, x, G. n, and A. Plaza, "Spatial-spectral preprocessing for volume-based endmember extraction algorithms using unsupervised clustering," in *Hyperspectral Image and Signal Processing: Evolution in Remote Sensing (WHISPERS), 2010 2nd Workshop on*, 2010, pp. 1-4.
- [86] A. Plaza, G. Martin, and M. Zortea, "On the incorporation of spatial information to endmember extraction: Survey and algorithm comparison," in *Hyperspectral Image and Signal Processing: Evolution in Remote Sensing, 2009. WHISPERS '09. First Workshop on*, 2009, pp. 1-4.
- [87] B. Rivard, D. M. Rogge, J. Feng, and J. Zhang, "Spatial constraints on endmember extraction and optimization of per-pixel endmember sets for spectral unmixing," in *Hyperspectral Image and Signal Processing: Evolution in Remote Sensing, 2009. WHISPERS '09. First Workshop on*, 2009, pp. 1-4.

- [88] M. Shaohui, H. Mingyi, W. Zhiyong, and F. Dagan, "Spatial Purity Based Endmember Extraction for Spectral Mixture Analysis," *Geoscience and Remote Sensing, IEEE Transactions on*, vol. 48, pp. 3434-3445, 2010.
- [89] M. Zortea and A. Plaza, "Improved Spectral Unmixing of Hyperspectral Images Using Spatially Homogeneous Endmembers," in *Signal Processing and Information Technology, 2008. ISSPIT 2008. IEEE International Symposium on*, 2008, pp. 258-263.
- [90] M. Zortea and A. Plaza, "Spatial Preprocessing for Endmember Extraction," *Geoscience and Remote Sensing, IEEE Transactions on*, vol. 47, pp. 2679-2693, 2009.
- [91] M. Zortea, D. Tuia, F. Pacifici, and A. Plaza, "Spectral-textural endmember extraction," in *Hyperspectral Image and Signal Processing: Evolution in Remote Sensing (WHISPERS), 2010 2nd Workshop on*, 2010, pp. 1-4.
- [92] C. M. Bishop, *Pattern Recognition and Machine Learning*: Springer, 2007.
- [93] S. Haykin, *Neural Networks and Learning Machines*, 3rd ed.: Pearson Education, Inc., 2009.
- [94] P. Honeine and C. Richard, "The angular kernel in machine learning for hyperspectral data classification," in *Hyperspectral Image and Signal Processing: Evolution in Remote Sensing (WHISPERS), 2010 2nd Workshop on*, 2010, pp. 1-4.
- [95] C. M. Bachmann, T. L. Ainsworth, R. A. Fusina, M. J. Montes, J. H. Bowles, D. R. Korwan, and D. B. Gillis, "Bathymetric Retrieval From Hyperspectral Imagery Using Manifold Coordinate Representations," *Geoscience and Remote Sensing, IEEE Transactions on*, vol. 47, pp. 884-897, 2009.
- [96] C. M. Bachmann, T. L. Ainsworth, R. A. Fusina, R. Topping, and T. Gates, "Manifold coordinate representations of hyperspectral imagery: Improvements in algorithm performance and computational efficiency," in *Geoscience and Remote Sensing Symposium (IGARSS), 2010 IEEE International*, 2010, pp. 4244-4247.
- [97] C. M. Bachmann, T. L. Ainsworth, D. B. Gillis, S. J. Maness, M. J. Montes, T. F. Donato, J. H. Bowles, D. R. Korwan, R. A. Fusina, G. M. Lamela, and W. J. Rhea, "A new data-driven approach to modeling coastal bathymetry from hyperspectral imagery using manifold coordinates," in *OCEANS, 2005. Proceedings of MTS/IEEE*, 2005, pp. 2242-2249 Vol. 3.
- [98] C. M. Bachmann, T. L. Ainsworth, D. B. Gillis, S. J. Maness, M. J. Montes, T. F. Donato, J. H. Bowles, D. R. Korwan, R. A. Fusina, G. M. Lamela, and W. J. Rhea, "Modeling Coastal Waters from Hyperspectral Imagery using Manifold Coordinates," in *Geoscience and Remote Sensing Symposium, 2006. IGARSS 2006. IEEE International Conference on*, 2006, pp. 356-359.

- [99] M. Li, M. M. Crawford, and T. Jinwen, "Local Manifold Learning-Based k -Nearest-Neighbor for Hyperspectral Image Classification," *Geoscience and Remote Sensing, IEEE Transactions on*, vol. 48, pp. 4099-4109, 2010.
- [100] S. T. Roweis and L. K. Saul, "Nonlinear Dimensionality Reduction by Locally Linear Embedding," *Science*, vol. 290, pp. 2323-2326, December 22, 2000.
- [101] X. R. Wang, S. Kumar, F. Ramos, and T. Kaupp, "Probabilistic Classification of Hyperspectral Images by Learning Nonlinear Dimensionality Reduction Mapping," in *Information Fusion, 2006 9th International Conference on*, 2006, pp. 1-8.
- [102] K. Wonkook and M. M. Crawford, "Adaptive Classification for Hyperspectral Image Data Using Manifold Regularization Kernel Machines," *Geoscience and Remote Sensing, IEEE Transactions on*, vol. 48, pp. 4110-4121, 2010.
- [103] K. Wonkook, M. M. Crawford, and J. Ghosh, "Spatially Adapted Manifold Learning for Classification of Hyperspectral Imagery with Insufficient Labeled Data," in *Geoscience and Remote Sensing Symposium, 2008. IGARSS 2008. IEEE International*, 2008, pp. I-213-I-216.
- [104] C. Yangchi, M. M. Crawford, and J. Ghosh, "Applying nonlinear manifold learning to hyperspectral data for land cover classification," in *Geoscience and Remote Sensing Symposium, 2005. IGARSS '05. Proceedings. 2005 IEEE International*, 2005, pp. 4311-4314.
- [105] C. Yangchi, M. M. Crawford, and J. Ghosh, "Improved Nonlinear Manifold Learning for Land Cover Classification via Intelligent Landmark Selection," in *Geoscience and Remote Sensing Symposium, 2006. IGARSS 2006. IEEE International Conference on*, 2006, pp. 545-548.
- [106] G. Camps-Valls, T. Bandos Marsheva, and D. Zhou, "Semi-Supervised Graph-Based Hyperspectral Image Classification," *Geoscience and Remote Sensing, IEEE Transactions on*, vol. 45, pp. 3044-3054, 2007.
- [107] G. Camps-Valls, M. Martinez-Ramon, J. L. Rojo-Alvarez, and J. Munoz-Mari, "Nonlinear System Identification With Composite Relevance Vector Machines," *Signal Processing Letters, IEEE*, vol. 14, pp. 279-282, 2007.
- [108] T. Damoulas, Y. Ying, M. A. Girolami, and C. Campbell, "Inferring Sparse Kernel Combinations and Relevance Vectors: An Application to Subcellular Localization of Proteins," in *Machine Learning and Applications, 2008. ICMLA '08. Seventh International Conference on*, 2008, pp. 577-582.
- [109] M. Gonen and E. Alpaydin, "Localized Multiple Kernel Learning," in *25th International Conference on Machine Learning*, Helsinki, Finland, 2008.

- [110] M. Gonen and E. Alpaydin, "Localized Multiple Kernel Regression," in *Pattern Recognition (ICPR), 2010 20th International Conference on*, 2010, pp. 1425-1428.
- [111] D. Tzikas, A. Likas, and N. Galatsanos, "Large Scale Multikernel RVM for Object Detection," presented at the Hellenic Conference on Artificial Intelligence, Heraclion, Crete, Greece, 2006.
- [112] D. Wei and M. M. Crawford, "Locally consistent graph regularization based active learning for hyperspectral image classification," in *Hyperspectral Image and Signal Processing: Evolution in Remote Sensing (WHISPERS), 2010 2nd Workshop on*, 2010, pp. 1-4.
- [113] K. Wonkook and M. Crawford, "A novel adaptive classification method for hyperspectral data using manifold regularization kernel machines," in *Hyperspectral Image and Signal Processing: Evolution in Remote Sensing, 2009. WHISPERS '09. First Workshop on*, 2009, pp. 1-4.
- [114] B. Wu, W.-q. Zhang, and J.-h. Liang, "A Genetic Multiple Kernel Relevance Vector Regression Approach," in *Education Technology and Computer Science (ETCS), 2010 Second International Workshop on*, 2010, pp. 52-55.
- [115] C. M. Bachmann and T. L. Ainsworth, "Bathymetric retrieval from manifold coordinate representations of hyperspectral imagery," in *Geoscience and Remote Sensing Symposium, 2007. IGARSS 2007. IEEE International, 2007*, pp. 1548-1551.
- [116] C. M. Bachmann, T. L. Ainsworth, and R. A. Fusina, "Improvements to land-cover and invasive species mapping from hyperspectral imagery in the Virginia Coast reserve," in *Geoscience and Remote Sensing Symposium, 2004. IGARSS '04. Proceedings. 2004 IEEE International, 2004*, pp. 4180-4183 vol.6.
- [117] C. M. Bachmann, T. L. Ainsworth, and R. A. Fusina, "Exploiting manifold geometry in hyperspectral imagery," *Geoscience and Remote Sensing, IEEE Transactions on*, vol. 43, pp. 441-454, 2005.
- [118] C. M. Bachmann, T. L. Ainsworth, and R. A. Fusina, "Improved manifold coordinate representations of hyperspectral imagery," in *Geoscience and Remote Sensing Symposium, 2005. IGARSS '05. Proceedings. 2005 IEEE International, 2005*, pp. 4307-4310.
- [119] C. M. Bachmann, T. L. Ainsworth, and R. A. Fusina, "Improved Manifold Coordinate Representations of Large-Scale Hyperspectral Scenes," *Geoscience and Remote Sensing, IEEE Transactions on*, vol. 44, pp. 2786-2803, 2006.
- [120] C. M. Bishop, *Gaussian Processes*: Springer, 2007.
- [121] C. E. Rasmussen and C. K. I. Williams, *Gaussian Processes for Machine Learning*. Cambridge: The MIT Press, 2006.

- [122] K. Wonkook, C. Yangchi, M. M. Crawford, J. C. Tilton, and J. Ghosh, "Multiresolution manifold learning for classification of hyperspectral data," in *Geoscience and Remote Sensing Symposium, 2007. IGARSS 2007. IEEE International*, 2007, pp. 3785-3788.
- [123] L. Yen-Yu, L. Tyng-Luh, and F. Chiou-Shann, "Local Ensemble Kernel Learning for Object Category Recognition," in *Computer Vision and Pattern Recognition, 2007. CVPR '07. IEEE Conference on*, 2007, pp. 1-8.
- [124] H. S. Seung and D. D. Lee, "The Manifold Ways of Perception," *Science*, vol. 290, pp. 2268-2269, December 22, 2000.
- [125] J. B. Tenenbaum, V. d. Silva, and J. C. Langford, "A Global Geometric Framework for Nonlinear Dimensionality Reduction," *Science*, vol. 290, pp. 2319-2323, December 22, 2000.
- [126] T. Bados, D. Zhou, and G. Camps-Valls, "Semi-supervised Hyperspectral Image Classification with Graphs," in *Geoscience and Remote Sensing Symposium, 2006. IGARSS 2006. IEEE International Conference on*, 2006, pp. 3883-3886.
- [127] J. P. L. NASA. *ASTER Spectral Library*. Available: speclib.jpl.nasa.gov/

BIOGRAPHICAL SKETCH

Ryan Close graduated from the University of Florida with a Bachelor of Science in computer science in December 2002 and a Master of Science degree in computer engineering in December 2005. From 2005 to 2008 he worked at ManTech Real-time Systems Laboratory as a staff software engineer. Ryan obtained the Doctor of Philosophy degree from the University of Florida in 2011. His research interests include: machine learning, automatic target recognition, remote sensing, and hyperspectral image analysis.